# DEVELOPMENT OF NOVEL HETERONANOSTRUCTURES ENGINEERED FOR ELECTROCHEMICAL ENERGY CONVERSION DEVICES

A Dissertation
Presented to
The Academic Faculty

by

Hoda Amani Hamedani

In Partial Fulfillment
of the Requirements for the Degree
Doctor of Philosophy in the
School of Materials Science and Engineering

Georgia Institute of Technology

August 2013

# DEVELOPMENT OF NOVEL HETERONANOSTRUCTURES ENGINEERED FOR ELECTROCHEMICAL ENERGY CONVERSION DEVICES

Approved by:

Dr. Hamid Garmestani, Advisor
School of Materials Science and
Engineering
*Georgia Institute of Technology*

Dr. Meilin Liu
School of Materials Science and
Engineering
*Georgia Institute of Technology*

Dr. Kenneth H. Sandhage
School of Materials Science and
Engineering
*Georgia Institute of Technology*

Dr. Faisal M. Alamgir
School of Materials Science and
Engineering
*Georgia Institute of Technology*

Dr. Said Ahzi
School of Materials Science and
Engineering
*Georgia Institute of Technology*

Dr. Karl I. Jacob
School of Materials Science and
Engineering
*Georgia Institute of Technology*

Dr. Mohammad A. Khaleel
Fundamental and Computational
Sciences Directorate, *Pacific Northwest
National Laboratory*

Date Approved:  May 17, 2013

*To my dear husband and my lovely parents*

# ACKNOWLEDGEMENTS

My appreciation extends to the academic and administrative members of the School of Materials Science and Engineering at Georgia Tech. I am indebted to my many colleagues who supported me throughout my PhD study at Georgia Tech. I must extend my great appreciation to the members in Prof. El-Sayed's group in the department of Chemistry and Biochemistry, especially Dr. Nageh Allam for all his kind helps during the initial stages of my work. I would like to thank my other colleagues at Georgia Tech for their technical advice and assistance in fabrication and measurements: Dr. Maysamreza Chamanzaar, Dr. Ji Il Choi, Dr. Mingfei Liu, Dr. Masood Ebrahimi, Dr. Mohamad Hadi Kassaee, Dr. Cole Petersburg, Dr. Xukai Xin, Dr. Xinchang Pang, Mr. Roozbeh Tabrizian, Mr. Simon Lee and Mr. Samson Lai.

My appreciation extends to technical staff at the National High Magnetic Field Laboratory, Dr. Yan Xin and Dr. Yi-Feng Su for their great assistance in performing an extensive TEM work.

I acknowledge the Pacific Northwest National Laboratory (PNNL) for providing me with the financial support through my Ph.D. study.

Finally, I would like to express my deepest gratitude above all to my husband, Hossein, for his love, unconditional support, and his long patience for the accomplishment of my Ph.D. work. I am deeply thankful to my wonderful parents Aliakbar and Maryam, my lovely sister Mahya and my kind brothers Mohsen and Mohammadhossein for their never-ending love, enthusiasm, patience and always being there during these years to help me and to inspire me toward success in my life.

# TABLE OF CONTENTS

# LIST OF TABLES

# LIST OF FIGURES

# LIST OF SYMBOLS

| | |
|---|---|
| $a$ | Unit cell parameter |
| $b$ | Unit cell parameter |
| $c$ | Unit cell parameter |
| $e_g$ | $d$-orbitals splitting |
| $Q$ | Charge |
| $R$ | Universal gas constant |
| $t_{2g}$ | $d$-orbitals splitting |
| $V$ | Potential |
| $\varepsilon$ | Dielectric permittivity |
| $\sigma$ | Charge density |

# LIST OF ABBREVATIONS

| | |
|---|---|
| 0D | Zero-dimensional |
| 1D | One-dimensional |
| 2D | Two-dimensional |
| 3D | Three-dimensional |
| AAO | Anodic aluminum oxide |
| AC | Alternating current |
| Ag | Silver |
| AgCl | Silver Chloride |
| $Al_2O_3$ | Aluminum oxide |
| B | Boron |
| $BaF_2$ | Barium fluoride |
| $Ba(OH)_2$ | Barium hydroxide |
| $BaTiO_3$ | Barium titanate |
| BE | Binding energy |
| BST | Barium strontium titanate |
| C | Carbon |
| $CaF_2$ | Calcium fluoride |
| CdS | Cadmium sulfate |
| Co | Cobalt |
| Cr | Chromium |
| Cu | Copper |
| CVD | Chemical vapor deposition |

| | |
|---|---|
| DI water | Deionized water |
| DSSC | Dye Sensitized solar cells |
| EDS | Energy dispersive X-ray spectroscopy |
| EELS | Electron energy loss spectroscopy |
| EG | Ethylene glycol |
| EXAFS | Extended X-ray absorption fine structure (spectroscopy) |
| $F^-$ | Fluoride |
| Fe | Iron |
| FESEM | Field-emission scanning electron microscopy |
| FFT | Fast Fourier transforms |
| FGM | Functionally graded material |
| FIB | Focused ion beam |
| FWHM | Full width at half the maximum height |
| GB | Grain boundary |
| GR | Growth rate |
| HAADF-STEM | High angle annular dark-field scanning electron microscopy |
| HF | Hydrofluoric acid |
| HNS | Hetero-nanostructure |
| $H_3PO_4$ | Phosphoric acid |
| $H_2SO_4$ | Sulfuric acid |
| HRTEM | High-resolution transmission electron microscopy |
| HT-GIXRD | High temperature-grazing incidence X-ray diffraction |
| IT | Intermediate temperature |
| ICP-MS | Inductively coupled plasma - mass spectrometer |
| KOH | Potassium hydroxide |

| | |
|---|---|
| LD-MOCVD | Liquid delivery metal organic chemical vapor deposition |
| LSM | Lanthanum strontium manganite |
| MEMS | Micro-electromechanical systems |
| Mg | Magnesium |
| μ-SOFC | Micro-solid oxide fuel cell |
| Mn | Manganese |
| Mo | Molybdenum |
| N | Nitrogen |
| NEMS | Nano-electromechanical systems |
| NEXAFS | Near-edge X-ray absorption fine structure (spectroscopy) |
| NHE | Normal hydrogen electrode |
| $NH_4F$ | Ammonium hydroxide |
| NIST | National institute of standards and technology |
| NT | Nanotube |
| PEY | Partial electron yield |
| pH | Power of hydrogen |
| PR | Photoresist |
| Pt | Platinum |
| PONTs | Perovskite oxide nanotubes |
| PZT | Lead zirconate titanate |
| RIE | Reactive ion etching |
| SAED | Selected area electron diffraction |
| FESEM | Field emission scanning electron microscopy |
| Si | Silicon |
| $SiO_2$ | Silicon dioxide |

| | |
|---|---|
| SOFC | Solid oxide fuel cell |
| Sr | Strontium |
| $Sr(OH)_2$ | Strontium hydroxide |
| ST | Strontium-doped titania |
| STO | Strontium titanate |
| TEM | Transmission electron microscopy |
| TF-TNA | Thin film titania nanotube array |
| $(thd)_3$ | 2,2,6,6-tetramethylheptane-$3$,5-dionate |
| Ti | Titanium |
| $TiO_2$ | Titanium dioxide |
| UV/VIS | Ultraviolet-visible (spectroscopy) |
| XANES | X-ray absorption near-edge structure (spectroscopy) |
| XPS | X-ray photon spectroscopy |
| XRD | X-ray diffraction |
| YSZ | Yttrium stabilized zirconia |
| Y | Yttrium |
| Zr | Zirconium |

# SUMMARY

Heterogeneous nanostructures such as coaxial nanotubes, nanowires and nanorods have been of growing interest due to their potential for high energy-conversion efficiencies and charge/discharge rates in solar cell, energy storage and fuel cell applications. Their superior properties at the nanoscale as well as the high surface areas, fast charge transport along large interfacial contact areas, and short charge diffusion lengths have made them be considered as attractive components of next generation high efficiency energy-conversion devices.

Vertically-oriented $TiO_2$ nanotube arrays are considered as a robust and cost-effective nanostructure for a wide range of applications particularly those related to energy conversion such as solar hydrogen generation. Despite its fascinating properties, one major challenge limiting the use of such material for solar-irradiation driven applications involves with its electronic structure, namely, the large bandgap and improper band-edge positions with respect to photocatalytic reactions. Therefore, intense effort has been invested on modifying the electronic properties of $TiO_2$ by band-gap engineering via two active approaches, doping the bulk structure, or by suitable surface modification of the $TiO_2$ via sensitization or heterojunction formation to create a visible-light response. Despite significant enhancement obtained in the efficiency of photoconversion in many doped $TiO_2$ systems, an important question is still remained which involves with identification of whether the nanocrystals have been successfully doped. The primary focus of this dissertation is to understand the doping mechanism of $TiO_2$ nanotube exclusively with strontium as an alkaline earth metal to shed light on the relation between the observed enhancement in photocatalytic properties of doped $TiO_2$

nanotubes and its structural and electronic characteristics. The exploration of insertion of Sr atom into the $TiO_2$ nanotube structure is investigated in low concentrations as a dopant and in very high concentrations by processing of $SrTiO_3$ nanotube arrays. From bulk analysis of the Sr-doped nanotubes, it was found that the Sr is mainly incorporated into the lattice structure of $TiO_2$. However, from surface analysis of the doped nanotubes, it was revealed that at high Sr doping levels, there is a great tendency for phase segregation of SrO in the $TiO_2$ matrix along with formation of heterojunction between the two phases; in addition, the Sr doping only alters the Ti and O ions interaction in the $TiO_2$ lattice on the surface and has no evident effect on their individual charge states. It was inferred from the optical absorption measurements, that Sr doping of $TiO_2$ nanotubes up to the concentration close to the salt solubility limit can red shift the absorption edge of the material to as long as 402 nm. In addition, the highest photo-conversion efficiency of 0.69% was recorded for the doped sample with the highest concentration of Sr dopant.

In regard to the use of vertically oriented metal oxide nanotube arrays in electrochemical cells, and to address the polarization associated with ionic/electronic charge transport in the electrolyte as well as the anode of SOFCs, a new platform is proposed that can contribute in less-expensive/practically productive construction of micro-SOFCs as well as other micro and nano-scale ionic devices for other energy-related applications. Based on the proposed design, a membrane multilayer composite system with coaxial nanotubular architecture named as heteronanostructures (HNSs) with functionality in both electrode and electrolyte of micro-SOFCs is developed. As a part of fabrication of HNSs for micro-SOFCs, first coating of Sr doped $TiO_2$ nanotubes with YSZ is investigated. The growth mechanism of the YSZ on Sr-doped $TiO_2$ nanotubes in

the CVD process showed that in the deposition temperature range of 550°C - 580 °C the film growth rate follows the kinetically controlled regime, thereby, the thickness of the coating can be effectively controlled through the deposition time and temperature. Post-annealing process of the YSZ/coated Sr-doped $TiO_2$ nanotubes was shown to result in crystallinity of the film above 750 °C. It was also observed that the YSZ coating improves the thermal stability of the Sr-doped $TiO_2$ nanotubes up to 700 °C. Results show that by modification of the composition of the YSZ film to the higher Y doping level, crystalline YSZ can be achieved at lower temperatures.

Second, based on the proposed model of nanotubular composite, the fabrication and characterization of YSZ/STO heteronanostructures on silicon are studied. It was found that YSZ tends to grow crystalline on STO nanotubes backbone which is a great achievement in mitigating the problems that arise from further thermal annealing in thin-film processing. The proposed design and the developed fabrication scheme for processing HNSs membranes on silicon substrate can be considered as a new platform for being used in low temperature fuel cells-on-chip such as micro-SOFCs application.

# CHAPTER 1

# INTRODUCTION

## 1.1 Background and Motivation

Due to the world's ever increasing consumption of fossil fuels and its inevitable environmental impacts, extensive research efforts has been recently focused on development of clean and more viable forms of renewable energy. Clean power generation has been driven through direct conversion of sunlight to electricity using photovoltaic cells or indirectly via conversion of pollution-free hydrogen fuel into electricity using electrochemical devices such as fuel cells. Hydrogen gas is one of the most promising alternative energy carriers though available in limited quantity in the nature, it has high energy content [1]. Relying on recent advances toward application of renewable energies, one approach is to utilize solar energy with water to make hydrogen as the primary fuel source of the future. In general, hydrogen can be produced by replicating the natural process of photosynthesis, i.e. splitting water by illumination with sunlight through the photoelectrochemical water splitting process [2, 3].

$TiO_2$ is one of the most intensely researched materials by the materials science community due to a set of virtually unique functional properties (see Figure 1.1) that make the material stand out from other transition-metal oxides and classical group IV, III–V, or II– VI semiconductors. Properties such as low-cost, non-toxicity and very high photocorrosion resistance compared to other metal oxides, make it an interesting candidate for photocatalysis, and in dyesensitized solar cells (DSSCs). However, its

electronic structure composed of a band gap of ~ 3 eV and improper band-edge positions with respect to oxygen and hydrogen potentials, limits the use for solar-irradiation driven applications (only 7% of solar energy is provided in the spectral range < 400 nm, that is, under super-band-gap energy conditions of $TiO_2$). Therefore, intense efforts focus on modifying the electronic properties of $TiO_2$ by band-gap engineering i.e. narrowing the optical band gap via doping the bulk structure, or by suitable surface modification of the $TiO_2$ via sensitization or hetero-junction formation to create a visible-light response [4, 5].
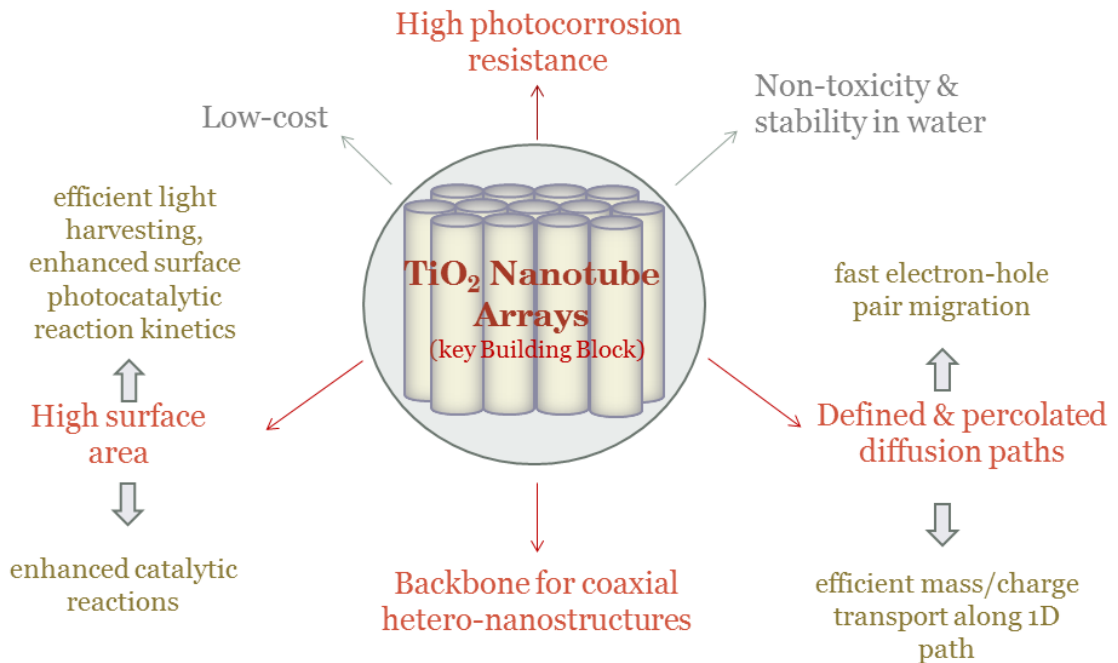


**Figure 1.1** Schematic showing the properties of $TiO_2$ nanotubes desired for energy conversion devices.

Despite the clear importance of $TiO_2$ nanostructures, most of the experimental and computational work has been focused on synthesis and demonstration of the enhanced

properties. Thus, a comprehensive investigation of the doping mechanism into $TiO_2$ bulk and lattice structure in relation to its effect on electronic and optical properties of the material have been still lacking. This has motivated the efforts in the present study to be profoundly invested on the mechanism of doping in $TiO_2$ nanotube arrays structure.

Solid oxide fuel cells (SOFCs) are the most efficient energy conversion devices that produce electricity directly from the electrochemical oxidation of a range of gas fuels from hydrogen to hydrocarbons without burning the fuel [6]. As such, these devices can be utilized as alternative power sources for next-generation energy systems. Currently, the main application of SOFCs involves the stationary power generation systems with power output in the 1 kW to 1 MW range. Recently the large energy densities of SOFCs and the versatility in fuel use such as hydrocarbon fuels, have generated interest in development of SOFCs for mobile applications and portable electronics namely, micro-SOFCs (μ-SOFCs) in the lower 1-500 W range. In fact, it is expected that SOFCs can produce energy densities per volume and specific energy per weight significantly larger than mainly polymer electrolyte fuel cells, or PEFCs and state-of-the-art rechargeable Li-ion and Ni metal hydride batteries for such applications [7].

Extensive research is underway in both areas of stationary and portable applications to meet the goals toward commercialization of these devices by improving the performance and reliability of the cells while minimizing costs that are essentially associated with high operating temperatures (~ 800 -1000°C) and processing of SOFCs. The major elements of an SOFC cell consist of two porous electrodes, an anode and a cathode, separated by a solid electrolyte [8]. Most known electrolyte show their best functionality in oxygen ion transfer from cathode to the anode electrode at elevated

3

temperatures. In recent years, studies have focused on design of functionalized materials/microstructures that operate efficiently at lower temperatures (< 800 °C) while maintaining the high performance [9-11].
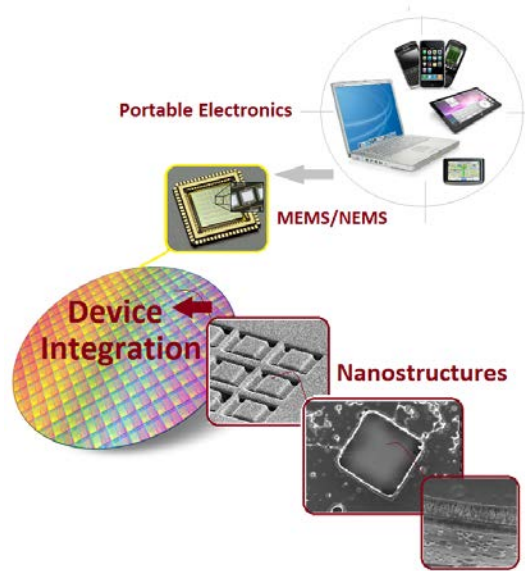


**Figure 1.2** Schematic showing the use of nanostructures for on-chip applications for down-scaling of micro-electronic devices.

As high performance portable electronic systems are becoming increasingly popular, development of portable power sources and devices that can operate efficiently at lower temperatures seem crucial (Figure 1.2). The use of thin-film technology in SOFCs area has gained a great portion of interest owing to the fact that it enables fabrication of high performance cells with thin electrolytes for lower temperature applications [12-14]. Moreover, development of novel nanostructures and nano-architectures not only has led to enhancement in properties of the individual components in the nano-scale, but also has made possible the down-scaling of the cells to smaller

dimensions for other applications. Despite significant advances in the field of integrated microelectronics, efficient power generation has not yet been fully explored for integrated circuits (IC) [15]. As such, development of miniaturized thin film SOFC structures such as μ-SOFCs with lateral dimensions in the sub-millimeter scale as sensors or power sources together with micro-electromechanical (MEM) components and other active electronics in the same silicon wafer seem to be very promising for use in portable electronic devices operating at low temperatures [14].

Such demanding applications have motived this research for development of novel hetero-nanostructures with improved low-temperature transport properties engineered for IT-SOFC and μ-SOFC applications. Owing to the large surface area and the defined path of the $TiO_2$ nanotube arrays, this work is motivated toward design and implementation of nanotubular heteronanostructures for enhancement of chemical reactions and fast transport of the chemical species as two requirements for enhancement of electrochemical performance of SOFCs.

# CHAPTER 2

# LITERATURE REVIEW AND RESEARCH OBJECTIVES

## 2.1 Metal Oxide Nanotubes

Since the discovery of carbon nanotubes by Ijima [16], considerable interest has been focused toward the fabrication of other types of one-dimensional (1D) nanomaterials. Inorganic nanotubes especially metal oxides are mostly fabricated to exploit other material-specific properties for many fields such as biomedical, photochemical, electrical, and environmental applications [17, 18]. The anodic aluminum oxide (AAO) was discovered in a pre-nanoscience era by anodic oxidation of aluminum in acidic electrolytes, resulting in the formation of a porous film consisting of nanotube arrays. Followed by the discovery of the hexagonal-packed porous aluminum oxide by anodization of aluminum, many attempts have been made to synthesize other metal oxides using the AAO template such as $TiO_2$ nanotubes [19]. Figure 2.1 shows the TEM and SEM images of some examples of metal oxide nanotubes such as isolated $BaTiO_3$ nanotube, $PbZrO_3$ nanotubes, $ZrO_2$, $BaSrTiO_3$ and $PbZrTiO_3$, $BiFeO_3$ [17, 18, 20]. Metal oxides nanotubes generally take the advantage of the large surface area and the defined geometry which results in a non-tortuous and narrow distribution of diffusion paths not only for entering the tubular depth (e.g., reactants to be transported to the tube bottom) but also for species to be transported through the tube wall, e.g., electrons, holes, ions. Therefore, the system response of ordered tube arrays in applications that involve transfer of charges species such as electrochemical sensing or photocatalysis is expected to be

more enhanced than using classical high surface area layers where nanoparticles are compacted or sintered to produce open porous network.
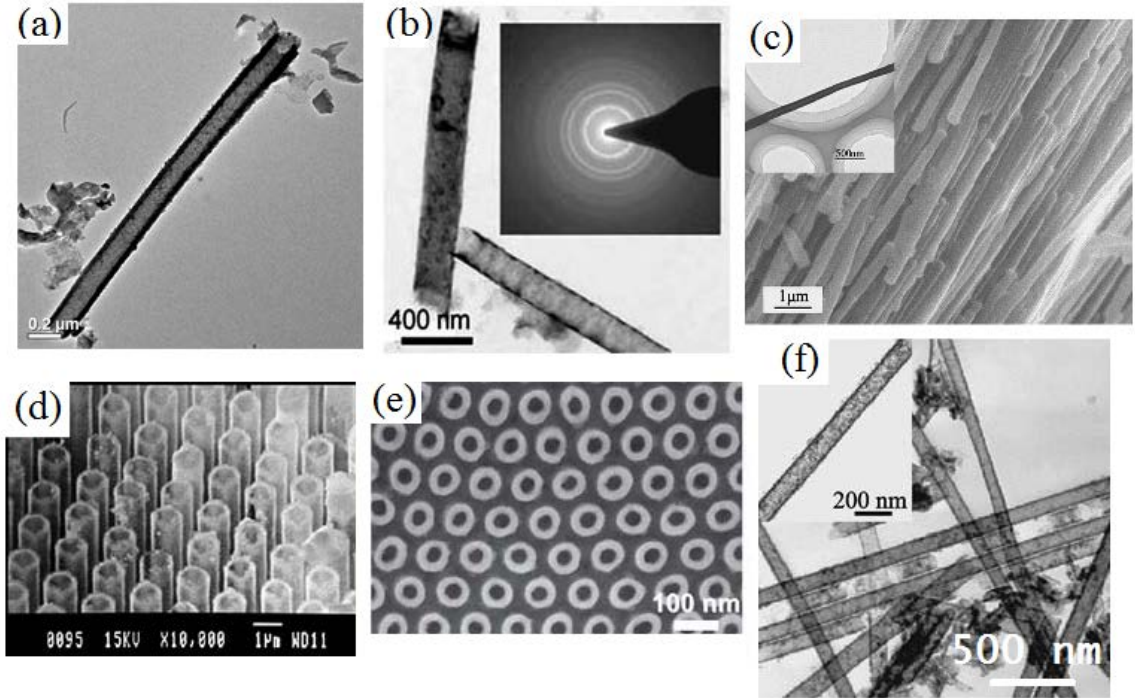


**Figure 2.1** TEM image of (a) an isolated $BaTiO_3$ nanotube. (b) $PbZrO_3$ nanotubes and the corresponding diffraction pattern. SEM image of $ZrO_2$ nanotubes in (c) and $BaSrTiO_3$ in (d) and $PbZrTiO_3$ in (e); (f) TEM image of isolated $BiFeO_3$ nanotubes. Reprinted with permission from ref.s [17, 18, 20].

### 2.1.1 Self-Organized Titania Nanotube Arrays

$TiO_2$ is naturally found in three crystalline forms namely (a) Anatase (I41/amd), (b) Rutile (P42/mnm) and (c) Brookite (Pbca), the first two being the most abundant. The crystal structures are shown in the Figure 2.2 where the $TiO_6$, with each $Ti^{+4}$ ion is

surrounded by six $O^{2-}$ ions forming an octahedron with eight triangular phases and six vertices [21].
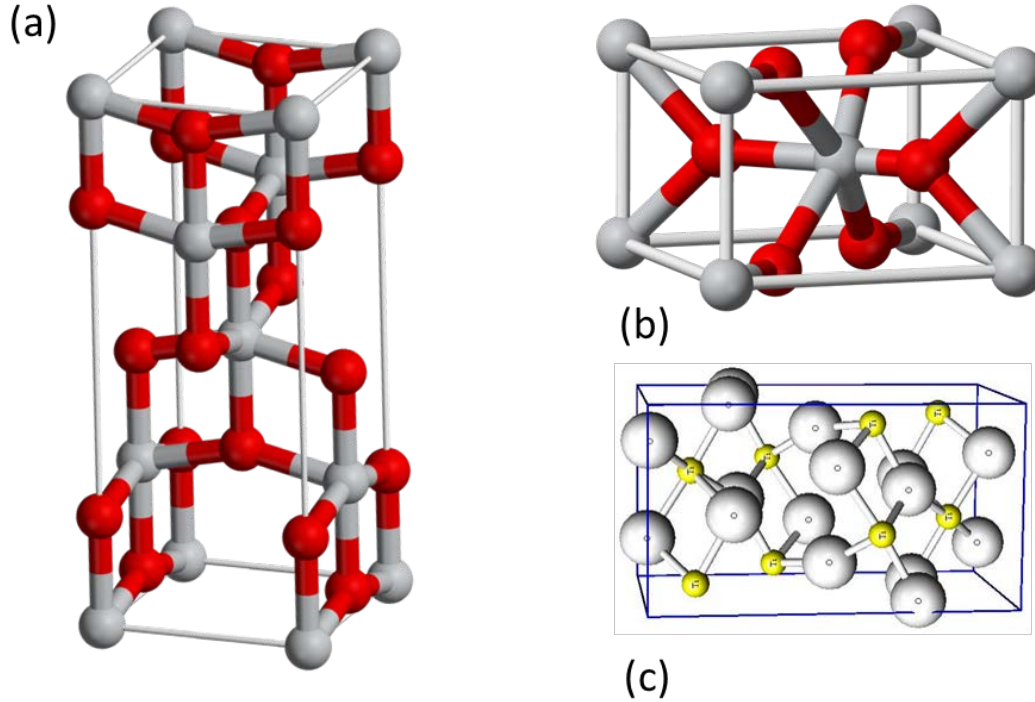


**Figure 2.2** Illustration of the crystal structure of (a) Anatase, (b) Rutile and (c) Brookite [21]

$TiO_2$ nanotubes in various lengths from a few tens of nanometers to a few tens of microns have been prepared using various physical and chemical synthesis routes [22]. Among them, the cheapest and most straightforward approaches that lead to ordered nanostructures are anodization techniques. During the anodization process, certain parameters such as applied potential, anodization time, and pH of the electrolyte can be used to control the resulting tube diameter, tube length, and overall morphology [59].

In photoelectrochemical water splitting, while the band gap of a photocatalyst must be large enough (> 1.23 eV) to dissociate water into hydrogen and oxygen, the relative energetic positions of the conduction and valence bands are also important. For example, the conduction band has to be more negative than the reduction potential of $H^+/H_2$ (0 V vs normal hydrogen electrode, NHE), whereas the valence band has to be more positive than the oxidation potential of $O_2/H_2O$ (1.23 V vs. NHE). In addition to these inherent materials properties, a large surface area is desirable for reaction kinetics, i.e. enhancement of surface photocatalytic reaction rates (Figure 2.3). Extremely high surface area of low dimensional $TiO_2$ structures such as 0D (particles) and 1D (tubes, wires, rods) as well as shorter distances the electron-hole pairs have to migrate to reach the surface in these nanostructures have shown to increase photo-conversion efficiency [2, 5].
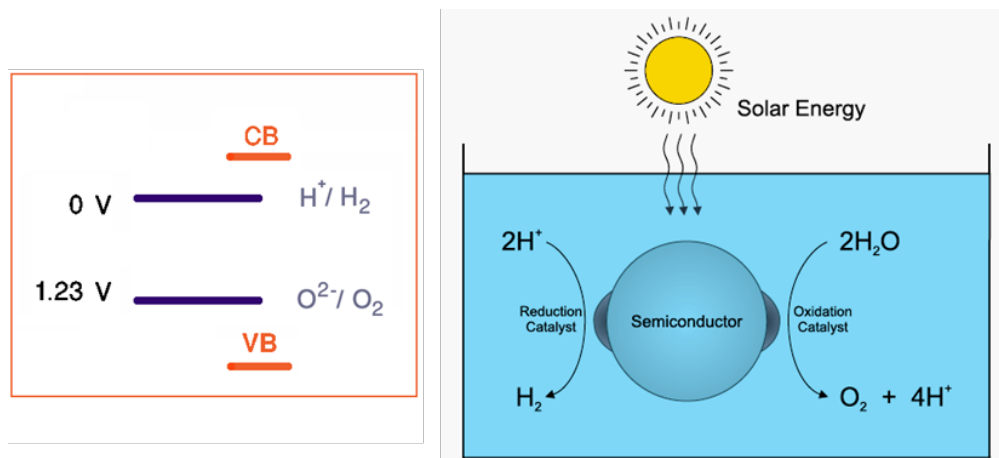


**Figure 2.3** Schematic of photoelectrochemical water splitting and the relative positions of conduction and valence bands required for dissociation of water. Reprinted with permission from ref. [23].

Besides taking the advantage of the nanotubular structure of these nanotubes, band gap engineering seems as a critical approach in improvement of electronic and optical properties of $TiO_2$ [24].

### 2.1.1.1 Effect of Doping and Coating on Physical Properties of Titania Nanotubes

Enhancement in the visible-light photoactivity of $TiO_2$ has been studied by introducing a wide range of transition metals including Fe, Mo, Mg, Ag, Pt, Co, Cr, Mn [5, 25, 26] and non-metal elements such as N, C, B [27-29] in the form of dopants or lower band-gap oxide composites with $TiO_2$ [28].

Doped $TiO_2$ nanostructures can typically be prepared by: 1) treating final or growing $TiO_2$ nanomaterials in a solution or melt of the doping species, 2) thermal treatments in gas atmospheres of the doping species, 3) co-sputtering, or sputtering in an atmosphere of the doping species and 4) high-energy ion implantation, 5) using alloys of the doped metal and Ti in electrochemical anodization. Among these approaches, method 1 and 4 seem more feasible and reliable, while ion implantation still suffers from inhomogeneous dopant distribution in the substrate depth [22].

Decoration and coating of $TiO_2$ nanotubes have been implemented widely in DSSCs as another efficient strategy for modification of the properties of such material. To suppress the recombination of charge carriers, typically a thin blocking layer that directs injected electrons toward charge-collecting substrate is introduced between sensitizer and oxide film. This approach typically involves fabricating composite electrodes in which two materials differ by their conduction band potential. This strategy

has been investigated in DSSCs with many different systems such as $CdS/TiO_2$ heterostructure nanotubes [30].

Of particular interest, strontium titanate ($SrTiO_3$) has been intensively investigated as a photoanode for water splitting due to its high corrosion resistance, excellent photocatalytic activity, high stability, and non-toxicity [31-33]. Although $SrTiO_3$ has band edges that straddle both oxygen and hydrogen redox potentials, it still suffers from its wide band gap (3.2 eV) nature. Recently, the specific phenomenon of combining the properties of both Titania and $SrTiO_3$ has attracted great attention [34-36]. Jitputti and co-workers reported production of $SrTiO_3$ from amorphous $TiO_2$ nanotubes arrays using hydrothermal process [37]. Particularly, using the same post-treatment hydrothermal method in a recent study, Kamat and co-workers applied a new approach into fabrication $TiO_2$ nanotubes decorated with $SrTiO_3$ particles/clusters. This study showed an improvement in the overall photoelectrochemical performance of the composite material ($SrTiO_3/TiO_2$) only in the case of well-dispersed $SrTiO_3$ nanocrystallites on $TiO_2$ nanotube arrays [34]. However, more controlled methodology is needed to get the full benefit of the material. Considering the advantages of doping and coating/decoration approaches on the improvement of bandgap structure, it would be more desirable to incorporate metal ions into the $TiO_2$ nanotube arrays during their fabrication. Therefore, *in-situ* bandgap engineering of the $TiO_2$ nanotubes seems to be a promising alternative strategy to avoid such structural imperfections and morphological defects imposed by multi-steps fabrication methods.

### 2.1.2 Perovskite Oxide Nanotubes

Complex metal oxides with perovskite structure $ABO_3$ (where A and B are cations) exhibit a wide range of functional properties, such as ferroelectricity, piezo/pyroelectricity, non-linear dielectric and semiconducting behavior [17]. The cubic strontium titanate ($SrTiO_3$) crystal ($Pm\bar{3}m$ space group, see Figure 2.4) is an excellent and well-known example of this family which deserves attention as an archetypical model $ABO_3$ perovskite for a wide range of applications. It has a simple structure, high thermal stability ($T_{melt} = 2100^{\circ}$ C) and an excellent chemical resistance to many solvents. It shows interesting properties such as high temperature stability, combination of electronic and ionic conductivity and a very large dielectric permittivity ($\varepsilon = 300$ at room temperature), photoelectric and catalytic properties which make this compound a great candidate for several different applications including high-voltage capacitors, sulfur tolerant anode of solid oxide fuel cells (SOFCs) [38-40], oxygen sensors [41-43] and integrated optoelectronic devices [44]. Furthermore, due to the ability to form high quality interfaces with other crystals, it has been used for epitaxial growth of high-$T_c$ superconductors and other oxide-based multilayered systems.

Recently much attention has been focused on synthesis, structural characterization, and physical properties of perovskite oxide nanotubes (PONTs). The $TiO_2$ nanotubes have been used as template for formation of several ternary metal oxide nanotubes such as barium titanate nanotubes ($BaTiO_3$) via a hydrothermal reaction and sol-gel process of $TiO_2$ nanotubes in $Ba(OH)_2$ aqueous solution [45]. Other examples of PONTs include $(Ba,Sr)TiO_3$ (BST), $Pb(Zr,Ti)O_3$ (PZT), have been fabricated by using different methods [17, 18]. $La_{0.8}Sr_{0.2}MnO_{3-\delta}/Zr_{0.92}Y_{0.08}O_2$ (LSM/YSZ) composite nano-

tubes are co-synthesized by a pore wetting technique as a cathode material for solid oxide fuel cells (SOFCs) [46]. Similar to other perovskite materials at the nanoscale, nanostructured $SrTiO_3$ exhibit novel physical properties that are different from its bulk and film counterparts. Recently, one-dimensional (1D) $SrTiO_3$ nanostructures have shown to be very promising for use in photoelectrochemical applications such as dye-sensitized solar cells and photocatalytic hydrogen production [47] and also in biomedical applications as Sr delivery platform for osseointegration on Ti-based bone implants [48]. The use of high surface area 1D $SrTiO_3$ nanotubes can also offer the possibility of increasing the sensitivity and stability for various types of MEMS/NEMS-based applications such as oxygen gas sensors. Besides, $SrTiO_3$ nanotube arrays (hereafter STO NTAs) can serve as an excellent model material for a wide class of $ABO_3$ perovskites oxide nanotubes [17]. Despite recent progress in design and development of state-of-the-art nanostructured materials and the efforts toward fundamental scientific understanding of their intrinsic size-dependent properties, integration of such functional nanostructures into silicon wafer is indispensable for utilization of these nanostructures as building blocks of miniaturized microelectronic devices. Recently, intense experimental efforts have been made in preparation of perovskite nanotubes via template approach followed by the through exchange of cations by wet-chemical synthesis low-temperature hydrothermal reaction route [37, 49, 50]. Thus, development of STO NTAs on silicon wafer and investigation of its electrical properties at elevated temperatures can serve as a key step toward utilization of such materials in variety of applications.
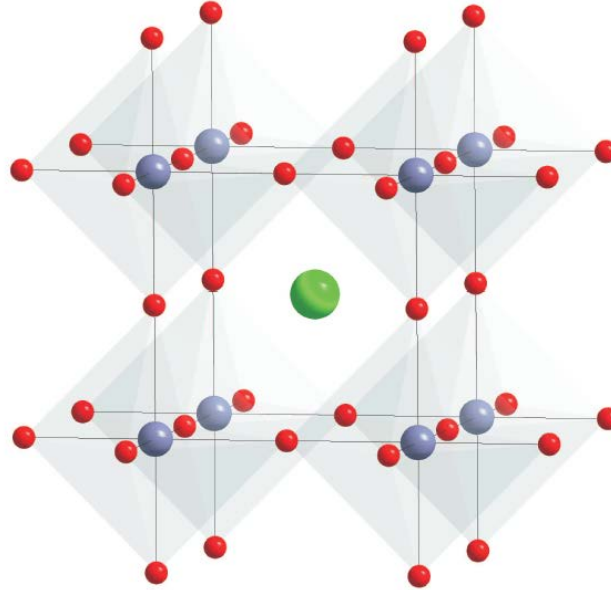
**Figure 2.4** $SrTiO_3$ cubic structure: $Pm\bar{1}3m$ space group with a = 3.90 °A. Reprinted with permission from ref. [51].

## 2.2 Integration of Oriented Metal Oxide Nanotubes with Microdevices

The development of high performance portable electronic systems requires the integration of power sources with other electronic components on the same silicon wafer. Titanium dioxide ($TiO_2$) is one of the most researched functional semiconductor materials which finds versatile applications in sensors, optoelectronics, dye-sensitized solar cells, photocatalysis, biomedicine, electrochemical and storage devices such as batteries [52-55]. More recently, self-assembled 1D vertically oriented $TiO_2$ nanotube arrays grown on different substrates has been shown to be an attractive component of such devices due to its enhanced structural properties at the nanoscale [56-58]. Of many routes that have been used to prepare 1D array of metal-oxide nanotubes, including template and hydrothermal synthesis, electrochemical lithography, the electrochemical

14

anodization process is the most promising technique with the potential for automation relative to many other methods [5, 59-61]. This, it is highly desirable to grow as many types of metal oxides nanotubes on the silicon wafer.

## 2.3 Solid Oxide Fuel Cells

Solid Oxide Fuel Cell (SOFC) is an electrochemical conversion device that produces electricity directly from oxidizing a fuel. A single cell includes three major components, the cathode, electrolyte and anode as shown in Figure 2.5 with the corresponding primary figures of merit: $E$ represents the potential induced across the cell under open circuit conditions for a given $P_{O_2}$ gradient, $\hat{t}_i$ is the ionic transference number, $E_N$ is the Nernst potential, $R_{INT}$, $R_C$, $R_{SE}$ and $R_A$ are the internal cell, cathode, solid electrolyte and anode resistances, respectively, $J_{O_2}$ is the oxygen permeation flux, and $L$ the thickness across which the $P_{O_2}$ gradient is imposed. All other terms have their normal meanings [62]. The standard SOFC electrolyte material is 8% yttria-stabilised zirconia (YSZ), strontium-doped lanthanum manganite such as $La_{0.8} Sr_{0.2} MnO_{3-\delta}$ (LSM) as the cathode and the Ni-YSZ cermet as the anode. The cell operates when the fuel gas (normally oxygen from air) is supplied to the porous cathode and is reduced to oxygen ions while the current is being drawn, based on the following reaction:

$$1/2O_2 + 2\bar{e} + V_{\ddot{O}} \Leftrightarrow O_O \tag{2.1}$$

In mixed ionic electronic conducting (MIEC) cathodes such as $La_{1-x}Sr_xCoO_3$ (LSCO), this reaction is accelerated as the cathode can provide both electrons as well as oxygen vacancies. The LSCO is known as an attractive choice for SOFC cathodes as it shows electronic conductivity of $> 100S$/cm and the oxygen ion conductivity of $> 1S$/cm at temperatures above 800 ºC. This ceramic compound has the best compatibility with doped ceria electrolytes, such as $Ce_{1-x}M_xO_2$:M=Gd or Sm, for operation at reduced temperatures of 550–750 ºC [62].



$$E = \hat{t}_i E_N = \hat{t}_i \frac{kT}{4q} \ln\left(\frac{P_{O_2}'}{P_{O_2}''}\right)$$

$$R_{INT} = R_C + R_{SE} + R_A$$

$$J_{O_2} = -\frac{RT}{4^2F^2L}\int_{\ln P_{O_2}'}^{\ln P_{O_2}''} \frac{\sigma_{el}\sigma_{ion}}{\sigma_{el}+\sigma_{ion}}\, d\ln P_{O_2}$$
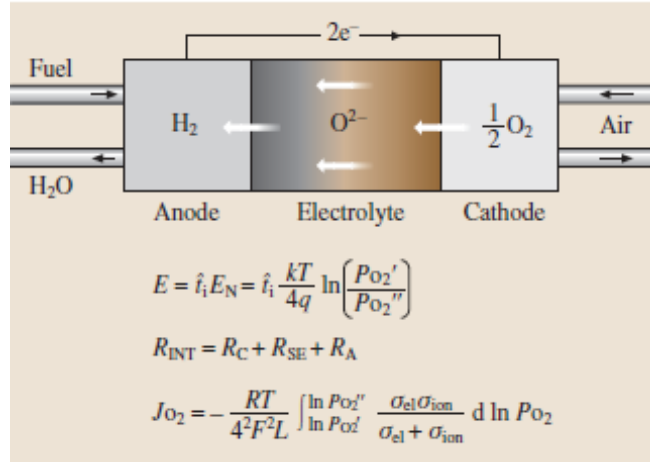
**Figure 2.5** Schematic of a solid oxide fuel cell and the primary figures of merit. Reprinted with permission from ref. [62].

### 2.3.1 Microstructure Design Based on the Use of Hetero-Nanostructures for Micro- and Intermediate Temperature (IT-) SOFCs

2.3.1.1 Hetero-Nanostructures for SOFCs Electrodes

The goal of microstructure design is to improve the microstructure to render enhanced properties in such a way that compensates the performance losses associated

with lower operating temperatures. Up to now, several strategies have been used to develop novel structures that demonstrate variety of advantages over other conventional microstructures. For instance, development of functionally graded materials (FGMs) as well as composite electrodes have been shown to be effective in enhancement of functionality of individual layers at low temperatures as well as improvement of electrodes performance in IT-SOFCs [11, 63].

Development of nanostructured electrode and electrolytes has been of great interest in advancing the science and technology of SOFCs. It is also well known that the physical and chemical properties of condensed matter differ at surfaces or interfaces significantly from the volume phase. Recently, the use of heterogeneous nanostructures (hereafter HNSs) in both electrolyte and electrode design has been of particular importance in understanding the role of nanostructures in mediating bulk and surface/interface ionic transport, gaseous molecular transport, and kinetics of $O_2$ reduction in the vicinity of the three-phase boundary [64, 65].

Using a nano-particulate approach, infiltration process has been used to create hetero-nanostructured cathodes [12, 66-68]. For instance, infiltration of yttria-doped ceria (YDC) into the LSM–YSZ composite cathode is reported to decrease the polarization resistance over 50% and thus increases the electrochemical performance of the cathode [66]. A single cell with LSM cathodes infiltrated in multiple cycles with YSZ produces a maximum power density of $1.13 \text{Wcm}^{-2}$ at 750°C [69] while the maximum power density of a cell with conventional LSM–YSZ composite cathode is only $0.14 \text{Wcm}^{-2}$ [70].
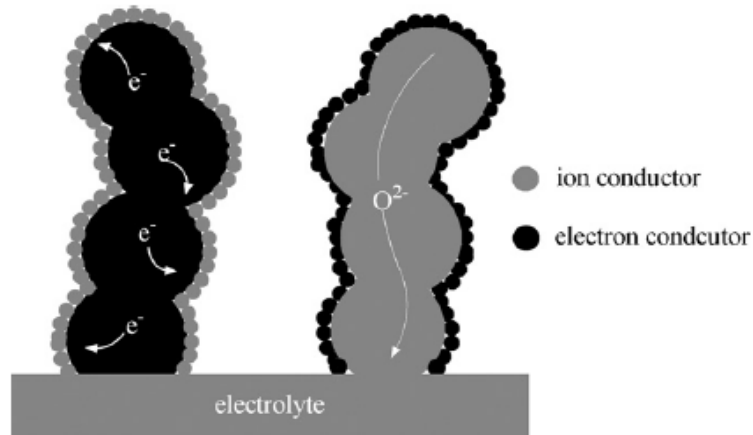
**Figure 2.6** Schematic of the microstructure derived by two types of infiltration strategies. Left: ionically conducting nanoparticles with electronically conducting backbone; right: electronically conducting nanoparticles with ionically conducting backbone. Reprinted with permission from ref. [64].

Figure 2.6 shows the morphology of the HNSs that can be derived by two types of infiltration strategy. On the left, ionically conducting nanoparticles with electronically conducting backbone and on the right the electronically conducting nanoparticles with ionically conducting backbone are shown as if cathodes and electrolytes such as perovskites (LSM, LSCF, etc.) can be used in composite with the electrolyte materials such as YSZ, GDC, etc., with one or the other as the backbone of the electrode.

Despite the advances in design of novel hetero-nanostructures for SOFCs cathodes, the use of such structures in the electrolyte has yet to be investigated. This strategy is expected to be more promising when combined with the idea of reducing the electrolyte thickness especially in miniaturized (micro) SOFCs, concerning the extensive electrolyte contribution to the total resistance of the device.

2.3.1.2 Hetero-Nanostructures for Improved Ion Transport

The most impressive improvements in ionic conductivity in SOFC electrolytes have been demonstrated in heterogeneous structures. In the case of ionic materials, faster ionic transport is often found at the interface between two similar (homophase) and dissimilar phases (heterophase). In a heterophase system, increase in conductivity at the interfacial regions can be related to the existence of a region with a more defective lattice structure caused by the structural mismatch between two different phases. Moreover, the formation of a space charge region with an increased concentration of mobile point defects may be responsible for such enhancement.

Recent studies on the contribution of interfacial transport to the overall transport in heterostructures have been focused on the thin film multilayer oxide ion conductors. Janek et al. have shown a strain dependence of the interfacial conductivity in multilayer thin film systems of $YSZ/Y_2O_3$, $YSZ/Lu_2O_3$ and $YSZ/Sc_2O_3$. Sata et al. [71] have developed heterolayered films of $CaF_2$ and $BaF_2$ that exhibit ionic conductivity (parallel to the interfaces) increasing proportionally with interface density- for interfacial spacing greater than 50 nanometres. The results are in excellent agreement with semi-infinite space-charge calculations, assuming redistribution of fluoride ions at the interfaces (Figure 2.7). Azad et al. [72] have also synthesized layer-by-layer structures of gadolinia-doped ceria and zirconia on $Al_2O_3$ (0001) using oxygen plasma-assisted molecular beam epitaxy. They have shown that the oxygen ion conductivity greatly increased with an increasing number of layers compared to bulk polycrystalline yttria-stabilized zirconia and gadolinia-doped ceria electrolytes.
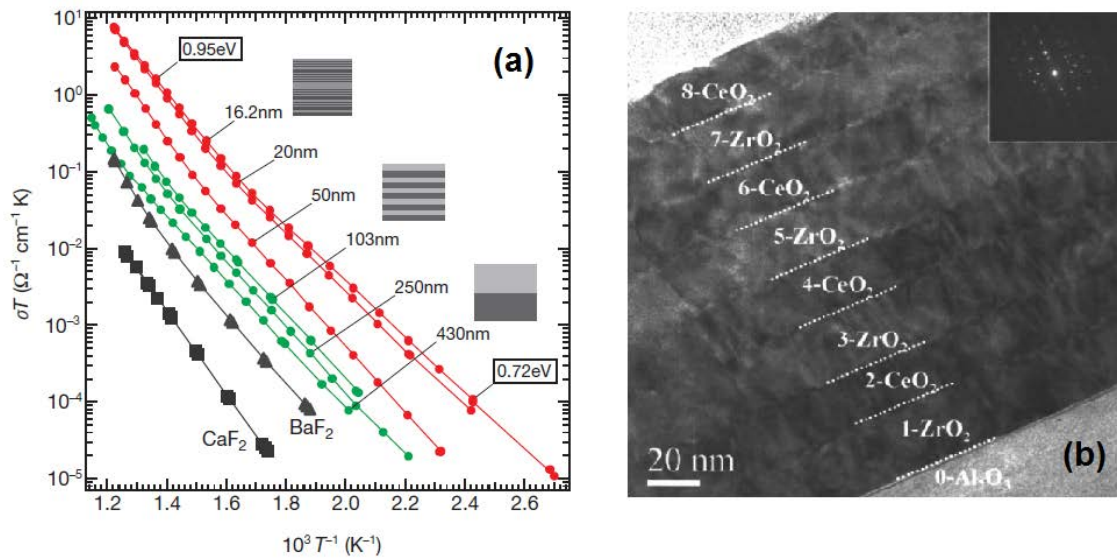
**Figure 2.7** (a) Parallel ionic conductivity of the films with various periods and interfacial densities in the 430±16 nm range. The overall thickness is approximately the same in all cases (~500 nm). σ, conductivity; T, temperature. The different colors refer to different site regimes (green: semi-infinite space charge zones; red: finite space charge zones) [71]. (b) TEM micrograph showing a cross sectional view of an eight-layer $Gd_2O_3$-doped $CeO_2$ and $ZrO_2$ film grown on $Al_2O_3$ (0001). Reprinted with permission from ref. [72].

Barriocanal et al. have reported a colossal enhancement in the ionic conductivity of up to 8 orders of magnitude near room temperature for yttria-stabilized zirconia (YSZ)/strontium titanate ($SrTiO_3$ or STO) epitaxial heterostructures on STO substrates, in which YSZ layers with thickness $t$ ranging from 1 to 62 nm were sandwiched between two 10-nm-thick STO layers. Such hetero-structures of STO/YSZ/STO achieved a very large conductivity in YSZ layers that are strained to 7% to match the STO lattice. The main reason is attributed to the near-interface region where mismatch between the YSZ

and STO oxygen sublattices is likely to result in either O vacancies or disorder in the interfacial plane while being independent on the layer thickness [73].

A density functional theory study by Pantelides et. al that relates the origin of such colossal ionic conductivity to a combination of lattice-mismatch strain and O-sublattice incompatibility. In fact, strain alone in bulk YSZ enhances O mobility at high temperatures due to extreme O disorder. However, the key note in multilayer hetero-structures is the O-sublattice incompatibility which causes the same extreme disorder at room temperature. Moreover, it is proposed that the coherent growth of strained interfaces in hetero-structures of materials with different degrees of lattice mismatch may promote ion diffusivity [65, 74]. Zhang et al. have also fabricated heterogeneous free-standing films of ordered $CeO_2$/Ni concentric nanostructures containing arrays of ceria nanotubes (200 nm OD, 100 nm ID) coated with Ni/$CeO_2$ using template-assisted electrodeposition method. They reported the use of such heteronanostructures as an anode electrocatalyst/current collector of SOFCs with the interfacial contact area within the 3-dimensional oxide nanotube/nickel matrix ~ 100 times greater than 2-dimensional thin films of nickel and ceria of the same area (Figure 2.8) [75].
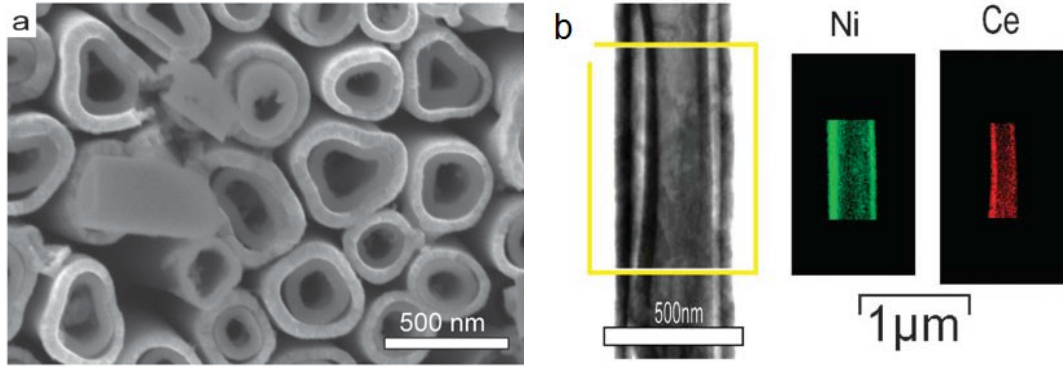
**Figure 2.8** (a) SEM image of Ni–CeO$_2$ coaxial nanotube arrays after removal of the AAO template; (b) phase maps of a Ni–CeO$_2$ coaxial nanotube. Reprinted with permission from ref. [75].

2.3.1.3 Impact of Ordered Metal Oxide Nanotubes on Micro-SOFC Applications

As mentioned in previous sections, the large surface area and the defined geometry of vertically oriented metal oxide nanotubes can offer particular advantages toward the use of such arranged nanostructures for various applications. For many types these applications, diffusion and transport of chemical and charged species are critical factors influencing the final device performance. The specific geometry of vertically oriented metal oxide nanotubes can provide a non-tortuous and narrow distribution of diffusion paths not only for entering the tubular depth (e.g., reactants and gas species to be transported to the tube bottom) but also for charged species to be transported through the tube walls, e.g., electrons, holes, ions. Therefore, the fast response of ordered nanotube arrays due to their large interfacial contact areas, high electrical conductivities, and short charge diffusion lengths dominates that of the conventional sintered porous networks [22].

Non-oriented metal Oxide nanotubes have been recently incorporated in SOFCs electrode microstructures based on random distributions of the nanotubes in the microstructure [76-79]. The vertical (columnar) orientation of the nanotubes on the electrolyte allows rapid gas diffusion through the inner diameters of the nanotubes to the TPBs and also provides a straight diffusion length (through the walls of the nanotubes) for fast transport of the ions to the electrolyte. This will result in a significant reduction in both gas concentration and activation polarizations. For instance, a lowest value of ASR of 0.21 $\Omega cm^2$ at 700 °C is reported for LSCO nanotubes for IT-SOFC cathodes compared to that of 0.4 $\Omega cm^2$ in conventional cobaltite-based cathodes [80, 81] Additionally, the issues of percolation in the ion-conductor phase is inherently resolved with nanotubes, as there are no "disconnected" regions as in conventional porous electrode-electrolyte composite structures [67]. In addition to the improved performance, nano-tubular structures have a lower tendency of sintering compared to nanoparticles in composites which will improve the stability of the porous microstructure [78].

## 2.4 Thesis Outline

The experimental part of this thesis is divided into five chapters as summarized in the following:

In chapter 3, a brief description of the experimental methods and materials that are used in this work are summarized. The experimental work includes fabrication, doping and coating processes of $TiO_2$ nanotube arrays on two types of substrates: titanium foil and silicon. This part is followed by description of the photolithography-based techniques that are used in this work for the development of the self-organized

nanotubes membrane on silicon wafer as a platform for being used in µ-SOFC applications. Further, details of the surface and bulk sensitive characterization techniques that were used for materials analysis are given. Finally, the optical and electrical test measurements that were used for property analysis of fabricated materials are also provided.

In an effort to extend the applicability of $TiO_2$ nanotube arrays for energy-conversion micro-devices such as micro-fuel solid oxide fuel cells, the growth of self-organized thin-film $TiO_2$ arrays on silicon substrate was studied using highly scalable and controllable electrochemical anodization technique. Chapter 4 is focused on the electrochemical growth of self-organized thin-film nanotube arrays (TF-TNAs) on silicon substrate via anodization of sputtered Ti on silicon via two different routes. In addition, the electrochemical growth mechanism of TF-TNAs on 3D FIB micropatterned isolated islands is reported.

In chapter 5, fabrication and growth mechanism of $Sr^{2+}$-doped $TiO_2$ nanotubes via one step electrochemical anodization technique is investigated. This chapter is mainly focused on understanding the mechanism of lower valence doping in self-organized $TiO_2$ nanotube arrays with a focus on the effect of strontium doping at various doping levels and processing conditions on the bulk and lattice structure as well as the electronic structure of the $TiO_2$ nanotubes. In addition, the effect of dopant and its level on properties of the $TiO_2$ nanotubes are further studied through measurements of the optical properties of the $Sr^{2+}$-doped $TiO_2$ nanotubes. Furthermore, the photocatalytic activity of the doped nanotubes is investigated in regard with the application of this material for water-splitting applications. The results from this part are provided in Appendix A.

24

For the purpose of development of coaxial composite HNSs and along with the observed effect from the doping of strontium on properties of $TiO_2$ nanotubes, and also in light of excellent properties of $SrTiO_3$ in many other fields of applications such as photoanode for hydrogen production through water splitting, the fabrication, growth mechanism and electrical conductivity of $SrTiO_3$ nanotubes on silicon is reported in chapter 6. The effect of growth kinetics parameters on effective control of the nanotubular morphology is also discussed.

In chapter 7, the coating process of the doped $TiO_2$ nanotubes and $SrTiO_3$ nanotubes is investigated. The growth mechanism of the YSZ on Sr-doped $TiO_2$ nanotubes in the CVD process is identified. Also, the structural properties and thermal stability of the composite YSZ/Sr-doped $TiO_2$ nanotubes are analyzed using different characterization techniques. A novel design approach for development of nanotubular multilayer system architecture is proposed for the electrolyte of μSOFCs. Based on the proposed model, YSZ/STO heteronanostructures are fabricated and characterized. The conductivity of STO and YSZ/STO NTAs composite system is measured by AC impedance spectroscopy.

# CHAPTER 3

# EXPERIMENTAL METHODS AND MATERIALS

## 3.1 Nanostructures and Their Fabrication Methods

### 3.1.1 Fabrication Techniques

3.1.1.1 Electrochemical Anodization and Thermal Annealing

The nanotube arrays were grown using the potentiostatic anodization process on 2cm x 2cm strips of polished pure titanium foil (0.25 mm thick, Alfa Aesar, 99.9+%) or that of sputtered titanium on silicon in a two-electrode cell configuration as depicted in Figure 3.1. Prior to anodization, the strips were rinsed in an ultrasonic bath of ethanol and cold DI water for 1 h and 15 min respectively. Pt mesh was used as the counter electrode and located in 2cm distance from the Ti electrode immersed in the electrolyte (Figure 3.1).
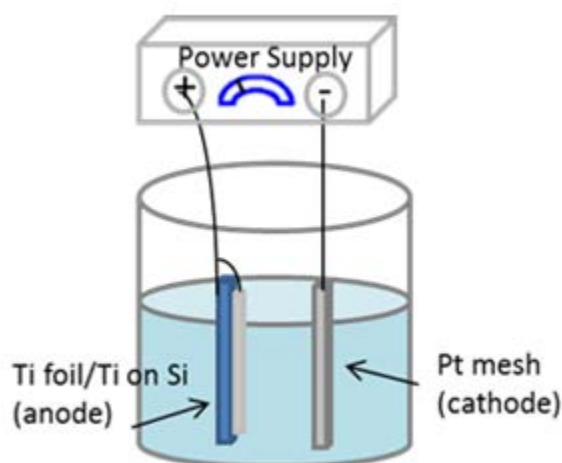


**Figure 3.1** Schematic of the electrochemical anodization setup.

<u>3.1.1.2 Hydrothermal Process</u>

Hydrothermal process is used for processing $SrTiO_3$ nanotube arrays via phase transformation of $TiO_2$ nanotube arrays in a bath of $Sr(OH)_2$ solution at various temperatures and reaction times. The $TiO_2$ nanotube samples on different substrates were cut into pieces and submerged into the solution which filled up to 2/3 of an alumina vessel. The vessel with closed cap was then moved into a stainless still autoclave and transferred to the furnace which was previously heated up to the desired temperature. After the hydrothermal treatment is terminated, the autoclave was moved out and kept at room temperature for 4 hours for cooling. The samples were taken out and were washed using ultrasonication in DI water for a few minutes to remove the white precipitates from the surface. The samples were finally dried with nitrogen gun.

**3.1.2 Thin-Film Deposition Techniques**

<u>3.1.2.1 Chemical Vapor Deposition (CVD)</u>

A lab-made (liquid-delivery) metal-organic chemical vapor deposition (LD-MOCVD) system in vertical configuration (Figure 3.2 (left)) was used for conformal coating of the nanotubes. This technique takes the advantage of using versatile liquid solvents for dissolving different precursors which enables having more control over the deposition. First, β-diketonate precursors ($M(thd)_3$, M=Zr, Y, for deposition of Yttrium-stabilized zirconia (YSZ)) dissolved in an organic solvent, and then the solution was pumped into the vaporization reactor. The volatized precursor produced was transported

27

with $N_2$ as the carrier gas to the reactor tube where the oxygen was mixed with the vapors. Due to the pressure gradient the deposition occurs on the heated substrate. The substrate temperature is kept constant at 580 °C. A combination of set of parameters such as deposition temperature, carrier gas flow-rate, solution delivery pump speed (flow-rate) and the vacuum pressure was varied to control the quality of the final coating and the growth mechanism in the regime where it is more kinetically controlled and is ideal for the film formation (Figure 3.2 (right)).
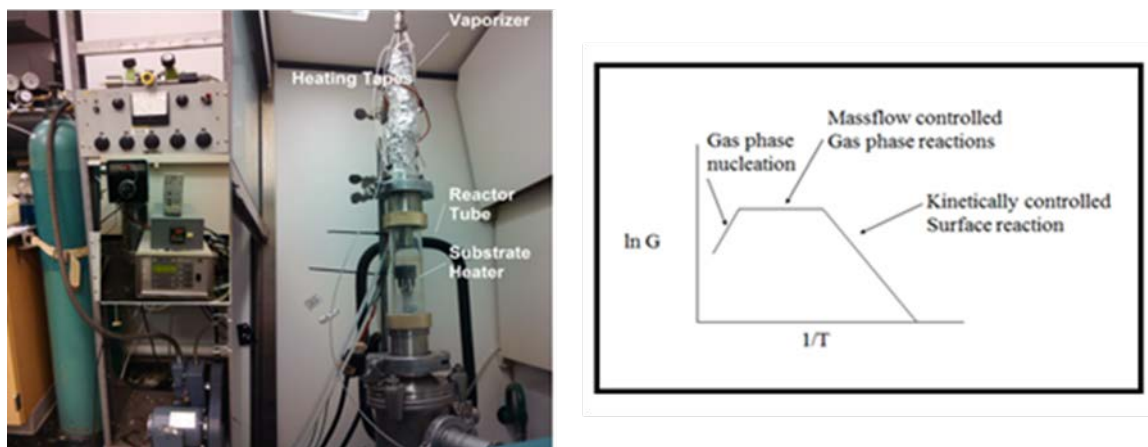


**Figure 3.2** Left: Photo of the liquid-delivery chemical vapor deposition (LD-MOCVD) system setup. Right: Schematic of CVD growth regimes.

### 3.1.2.2 Sputtering

The deposition of Ti films onto Si substrates was carried out using a dc magnetron sputtering (Denton Discovery) tool. The chamber was first evacuated to 2.0 x 10-7 torr backpressure and the argon gas pressure was then maintained at 6.0 x 10-4 torr during the deposition. The sputtering power and the deposition temperature were held constant at 125 W and 500 °C, respectively.

3.1.2.3 E-Beam Evaporation

The deposition of Yttrium-Stabilized Zirconia (YSZ) was performed using an E-Beam Evaporator (Denton Explorer) tool. The target was pressed YSZ pellets that were annealed at 700 °C for 4 hours.

## 3.1.3 Etching Technique

3.1.3.1 Focused Ion Beam (FIB)

The FEI Nova Nanolab 200 FIB/SEM was used for micro-patterning of sputtered Ti thin film into 3D isolated cylindrical and cubic regions of Ti on the silicon substrate. The ion beam voltage and current were set to 30 kV and 5 nA, respectively. The sputter material was set to aluminum with a sputter rate value (0.3 $\mu m^3/nC$) closest to that of titanium (0.37 $\mu m^3/nC$). In order to obtain the desired mill depth which is here the entire thickness of the Ti thin-film, the Z value was calculated based on the relation between the sputter rate, beam current and the volume of the material to be milled as in the following Eq.:

$$sputter\ rate = \frac{volume}{charge} \tag{4.5}$$

where, the charge is the beam current multiplied by the sputter time.

The FIB micro-patterning of sputtered thin-film Ti was performed to realize high resolution 3D (cylindrical and cubic) islands and investigation of the growth mechanism of thin-film nanotube arrays on these isolated regions on Si substrate using electrochemical anodization.

## 3.2 Morphological, Compositional and Crystal Structure Characterization

The morphology and composition of the samples were examined using a field emission scanning electron microscope (FESEM-Zeiss SEM Ultra60) equipped with EDS (energy-dispersive X-ray spectroscopy) detector. The analysis of the atomic structure and the chemical composition of the samples were carried out using a 200 KV atomic resolution transmission electron microscope (JEOL, JEM-ARM200F). For TEM observations, $TiO_2$ nanotube films were scratched off from the (titanium or silicon) substrate and were dissolved in ethanol followed by grinding. The dried powder-like samples were supported on Cu mesh with a carbon micro-grid. The TEM, high resolution TEM (HRTEM) and the high angle annular dark-field scanning transmission electron microscopy (HAADF-STEM) observations were performed using an aberration-corrected cold field emission scanning transmission electron microscope. The electron energy loss spectroscopy (EELS) and EELS spectrum imaging (EELS-SI) measurements were also performed using a Gatan GIF Quantum spectrometer. Additionally, the doped nanotubes were imaged using aberration-corrected atomic number contrast STEM (Z-STEM). All the TEM image processing has been performed using Gatan's Digital Micrograph software.

For the bulk and lattice crystal structure analysis and the phase evolution during annealing of the samples, X-ray diffraction (XRD) and in-situ high temperature glancing incidence X-ray diffraction (HT-GIXRD) using X'Pert PRO MRD diffractometer with Cu Kα radiation source were used. As a part of GIXRD optics, parallel-plate collimator was used to eliminate all sources of error associated with the focusing circle etc. The XRD data were analyzed and refined using Rietveld analysis with pseudo-Voigt peak profile fitting using MDI Jade, X'Pert HighScore Plus and MAUD software. NIST 640A

silicon was used as an external standard calibration sample to obtain instrumental peak broadening and FWHM calibration. The peak-fitting process is performed using pseudo-Voigt peak profile fitting algorithm in MDI Jade and MAUD softwares and is repeated to obtain the patterns that best fit the experimental data based on the calibration curve as a least-square fit of original patterns and the fitted ones. After the peak-fitting procedure is completed for all samples, the two-theta peak position assignment is performed using a peak-finding algorithm in MDI Jade software for all samples. Then, the Ti reference peak position in the pure $TiO_2$ sample is used to align all doped patterns with respect to the undoped one, and then the standard Ti peak position at $2\theta = 40.3$ is used to obtain the correct peak positions for all samples. The two-theta values obtained from this process are used in calculation of d-spacings and the lattice parameters.

The surface properties, composition and electronic structure of the samples were analyzed by X-ray photoelectron spectroscopy (XPS) using a Thermo Scientific K-Alpha system with an Al anode and Synchrotron near-edge X-ray absorption fine structure (NEXAFS). Analysis of photoemission lines was carried out after subtracting a Shirley-type background using a combined Gaussian-Lorentzian line shape, using symmetric line shapes for oxygen peaks for fitting. Additional constraint were applied for for fitting Sr 3d spectra with Sr $3d_{5/2}$ and Sr $3d_{3/2}$ doublet with energy separation of 1.8 eV and the peak area ratio of 1.5. The details of oxygen and strontium peak fitting spectra are provided in the Appendix B.

The NEXAFS was performed by acquiring peak intensities as a function of the incident X-ray photon energy in the vicinity of the titanium L-edge (445−490 eV) and the oxygen K-edge (520−590 eV) regions. The data were taken using a partial electron yield (PEY) detector and a 270 V rejection bias at the NIST beam line U7A located at the

31

National Synchrotron Light Source in Brookhaven National Laboratory. Simultaneous reference signals were collected from a TiN mesh and used to energy-calibrate the partial electron yield (PEY) signals. A 1200 l/mm grating was used together with 30 um x 30 um slits to energy select the incident beam. A 0.1 eV/ step energy resolution was used within at least +/- 20 eV of the absorption edge. In order to probe the Ti-O bond directionality, the NEXAFS data were collected varying the angle between the electric field vector of the x-rays and the surface of the nanotubes arrays with the photon beam fixed at parallel, in 55° and perpendicular to the surface normal of the sample. The final spectra were generated by post-processing this intensity versus energy dataset within various regions of the sample using the Athena program.

The dopant concentrations were measured in standard mode ICP MS (inductively coupled plasma - mass spectrometer) PerkinElmer, model ELAN 9000.

### 3.3 Property Measurements

### 3.3.1 Optical Property Measurements

3.3.1.1 Light Absorption Properties

Light absorption properties were performed on $Sr^{2+}$-doped titania nanotubes samples using a Shimadzu UV-3101PC UV-vis-NIR spectrophotometer with a wavelength range of 300-800 nm.

3.3.1.2 Photoelectrochemical Measurements

Photoelectrochemical properties were investigated in 1.0 M KOH solution using a three-electrode configuration with $Sr^{2+}$-doped nanotube arrays photoanodes, saturated

Ag/AgCl as a reference electrode, and platinum foil as a counter electrode. A scanning potentiostat (CH Instruments, model CH 660D) was used to measure dark and illuminated currents at a scan rate of 10 mV/s. Sunlight was simulated with a 300 W xenon ozone-free lamp (Spectra Physics) and AM 1.5G filter at 100 mW/cm$^2$ (Figure 3.3).
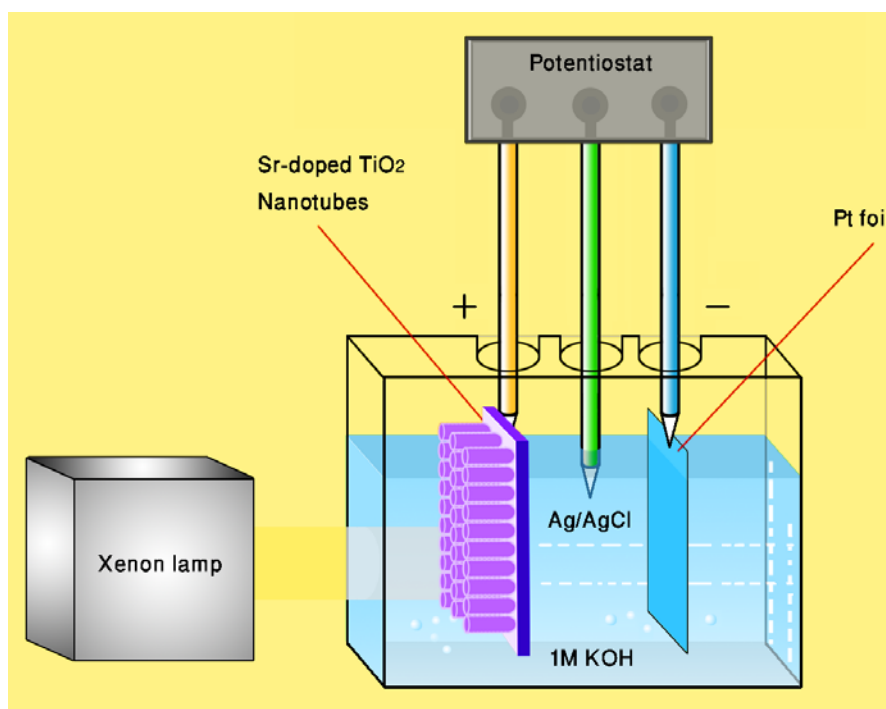


**Figure 3.3** Schematic of photoelectrochemical water splitting apparatus.

# CHAPTER 4

# SYNTHESIS AND CHARACTERIZATION OF THIN-FILM

# TITANIA NANOTUBE ARRAYS ON SILICON

## 4.1 Overview

A key to the incorporation of high surface area, high crystallinity $TiO_2$ to microelectronics applications, including micro-SOFCs, is the directed growth of $TiO_2$ nanotube arrays on silicon. Such architecture will allow for the development of novel micro/nano-electromechanical and electrochemical applications. Moreover, the high degree of biocompatibility of $TiO_2$-based nanostructures, combined with selective growth of such organized nanoporous structures on silicon, make this material an attractive model system to develop nano-sensors to study the response of cells. Photolithography, selective wet etching and reactive ion etching have been widely used for making patterned structures over large areas for various applications. Micropatterning and site-selective growth of $TiO_2$ thin film, $TiO_2$ nanotubes on Ti foil and TF-TNAs on silicon wafer have been reported using versatile approaches such as on superhydrophilic–superhydrophobic template, applying a seed-layer based on the use of photolithography techniques [82-84].

Recently, Schmuki and coworkers have reported the fabrication of photolithography micropatterned $TiO_2$ nanotubes which enable highly selective bone-like hydroxyapatite formation on defined lateral microstructures of the nanotubes [85]. Despite their potential capacity for generating large area of highly uniform periodic

microarrays, photolithography-based techniques suffer from multiple complex steps. The use of polymer photoresists and the difficulty of finding suitable etching conditions particularly suited for realizing high resolution 3D patterns add drawbacks to the implementation of such methods in several practical applications [86, 87].

Among all micro-nanopatterning techniques, focused ion beam (FIB) offers the larger variety of patterning schemes over nanolithography methods by site specific sputtering/milling as a resistless process with the capability of direct surface modification [88]. Such superior resolution of an FIB compared with photolithography makes it a suitable technique for specialty direct-write high resolution patterning with ever-higher aspect ratios [89]. Recently, Chen, et al. have used the FIB method for the fabrication and investigation of the growth mechanism of $TiO_2$ nanotubes on curved surfaces and in different arrangements in a FIB-guided anodization process [90, 91]. However, to the authors' knowledge, there is no report on the growth mechanism of TF-TNAs on 3D islands where the Ti film is only connected to the substrate from underneath and is isolated from its surroundings.

In this chapter, the fabrication and growth mechanism of self-organized $TiO_2$ nanotube arrays (TNAs) on silicon wafers and the growth mechanism of thin-film $TiO_2$ nanotube arrays on net-shape 3D micro-patterned arrays on silicon substrates are investigated. The 3D isolated growth of TF-TNAs on silicon using a one-step FIB process shows great promise toward the use of the proposed approach for the development of metal-oxide nanostructured devices and their integration with micro and nano-electromechanical systems (MEMS/NEMS) and integrated-circuit (IC) devices. In this paper, the synthesis of thin-film $TiO_2$ nanotube arrays (TF-TNAs) on silicon

substrate using two different electrolyte systems is reported. The fabrication and growth mechanism of TF-TNAs on three-dimensional (3D) isolated islands is demonstrated for the first time using the focused ion beam (FIB) technique. FIB milling (with $Ga^{+3}$ ion beam) is used for micropatterning of thin-film sputtered Ti to create isolated regions of different shapes for demonstration of the growth mechanism of $TiO_2$ nanotube arrays on these isolated areas with different geometries as a suggestive platform for biological cell growth studies and other types of micro-electrochemical/mechanical sensors and devices.

## 4.2 Synthesis and Characterization of Thin-Film TiO$_2$ Nanotube Arrays on Silicon

### 4.2.1 Titanium Thin-Film Deposition on Silicon

The n-type (100) Si wafers were first degreased using a standard technique followed by oxygen plasma cleaning prior to deposition. The Ti films of $800 \pm 10$ nm and $1.6 \pm 0.01$ µm thickness were deposited onto Si substrates using dc magnetron sputtering. The chamber was first evacuated to $2.0 \times 10^{-7}$ torr backpressure and the argon gas pressure was then maintained at $6.0 \times 10^{-4}$ torr during the deposition. The sputtering power and the deposition temperature were held constant at 125 W and 500 °C, respectively. The sputtering rate of titanium was found to be ~ 1 Å/sec which results in deposition of $800 \pm 10$ nm thick layer of titanium in ~ 135 min. Figure 4.1 sows the surface morphology of the sputtered titanium film on the silicon substrate.
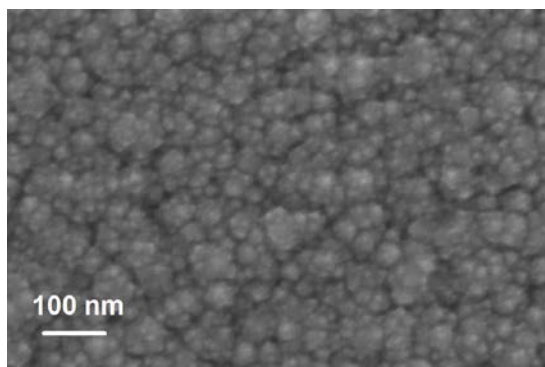
**Figure 4.1** FESEM image of the sputtered titanium on silicon.

**4.2.2 Growth of Thin-Film Titania Nanotube Arrays on Silicon**

Self-organized $TiO_2$ nanotube arrays were grown by electrochemical anodization of Ti thin-films on Si substrates in two different electrolytes. In the first route, the $TiO_2$ nanotube arrays were grown in a conventional two electrode cell in an aqueous solution of 0.5 wt% HF and 1 M $H_2SO_4$ and at a constant temperature of 4 °C. The anodization voltage was held at constant voltage of 10 V during 30 min and 1 h. The second route consisted of room temperature anodization of the Ti thin-film in an organic electrolyte consisting of 96 wt. % ethylene glycol (EG) and 0.4 g $NH_4F$ dissolved in 3 wt. % DI water, at the constant voltage of 40V and for the same durations. Both TF-TNAs samples were annealed at 420 °C for 4 hours with a heating rate of 1 °C/s to form the crystalline anatase phase.

**4.2.3 Effect of Electrolyte on Morphology of TF-TNAs**

The growth of the thin-film oxide nanotube layer was first monitored by studying the current-time characteristics as reported elsewhere [92]. Figure 4.2 (a) and (b) show the top-view FESEM images of the as-anodized and the annealed TF-TNAs (and the

37

cress-section view of the backside of the nanotubes in inset), respectively. These nanotubes are formed by anodization of 800 ± 10 nm thin-film Ti in HF-containing aqueous electrolyte at 4 °C for 30 min and after annealing at 420 °C in air. As shown in this image, the average inner diameter and the length of as-anodized and annealed nanotubes was ~ 50 nm and ~ 300 nm, respectively; this diameter corresponds to that of the $TiO_2$ nanotubes grown on titanium foil and anodized at 10 V for the same duration as reported in the literature [57].
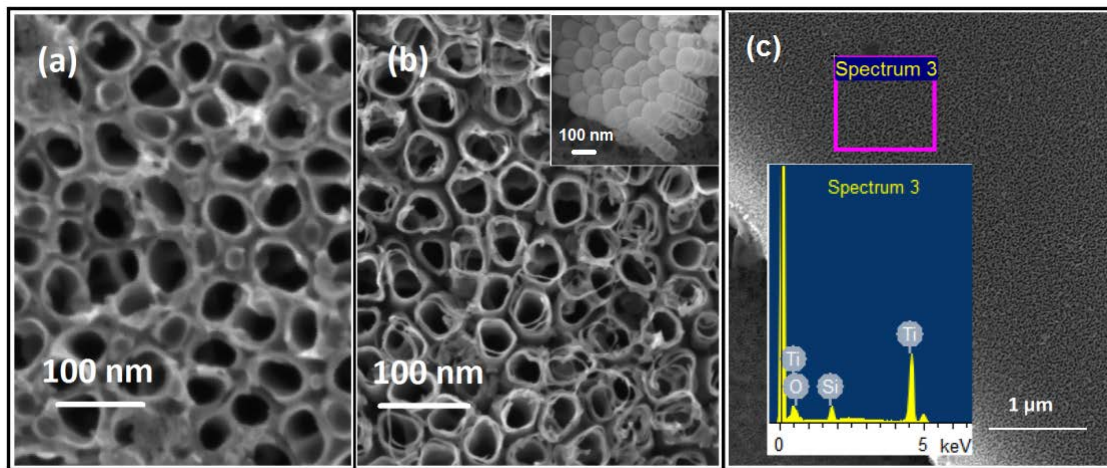


**Figure 4.2** (a) and (b) FESEM top-view FESEM images of the as-anodized and annealed TF-TNAs (inset: cross-section view of the nanotubes looking from backside) on silicon, respectively. (c) EDS spectra showing the chemical composition of the thin-film and the substrate.

Figure 4.2 (c) shows the FESEM image and the corresponding energy dispersive X-ray spectroscopy (EDS) analysis of the as-anodized TF-TNAs layer on the silicon

substrate which confirms the chemical composition of the film as well as the substrate. The formation of high quality nanotubes in this work was shown to be only achievable below 5 °C in the HF-based aqueous electrolyte solution. This is in accordance with the findings of Macak' et al., where the formation of nanotubes in similar HF-based electrolyte has been observed at temperature of 2°C [58].

Figure 4.3 shows the schematic representation of the thin-film $TiO_2$ nanotubular array under anodic conditions. The formation of nanotubes in electrochemical anodization is a self-ordering process in which the degree of ordering is dependent on the electrolyte (pH), voltage, temperature, and the presence of impurities in the material [93]. The mechanism of tube formation is shown in Figure 4.3 which is explained in detail in the following. The first step of the growth is controlled by the applied field and begins with $TiO_2$ formation (by oxidation of Ti layer as shown in Figure 4.3 (a) and based on Eq. 4.1) and continues with solvatization of $Ti^{4+}$ (Eq. 4.2); The applied field acts as the driving force for ionic transport through the barrier layer at the bottom of the pore [1]. Under the applied field, the $Ti^{4+}$ ions migrate outwards while $O^{2-}$ ions migrate towards the metal–oxide interface (Figure 4.3 (b)). Yasuda, et al. have found that nanopore/nanotube diameters correlate linearly with the growth factor of the transition metal oxide (the growth factor $f_{growth} = t_{film}/\Delta U$ in which $t_{film}$ is the (compact) oxide thickness that grows at a specific voltage in a metal and $\Delta U$ is the potential difference through the film) [94]. In fact, due to local changes in the thickness of the oxide layer over the surface, the distribution of electric filed is varied which results in anisotropy in the field assisted oxidation/etching process. As the process proceeds, the pores start to form locally through dissolution of the oxide at specific sites on the surface due to $F^-$ ions

attack directed by the local field distribution correlated to the surface morphological fluctuations as shown in Figure 4.3 (c). From these point sources, the oxide growth would take place immediately in all directions resulting to a hemispherical oxide structure with a certain radius R $= f_{\text{growth}}U$. Repeated breakdown at the bottom of the pores would then lead to an oxide tube diameter proportional to the oxidation factor of the metal [22]. As the chemical dissolution proceeds in the barrier layer, the electric field in these thinned regions increases, enhancing the field assisted oxide growth and oxide dissolution. Thus, well-defined inter-pore cavities start forming as if the entire growth process has started over in these regions as shown in Figure 4.3 (d). At this point, depending on the amount of water in the electrolyte, the ripples start to appear as a result of such repeating field assisted oxidation/thinning/dissolution process. Thereafter, both cavities and tubes grow in parallel and form the tube walls. The nanotube length increases until the electrochemical etch rate equals the chemical dissolution rate of the top surface of the nanotubes. Such chemical dissolution is the key step for formation of the nanotube arrays. At this step, the thinning process of the barrier layer is continued to keep the electrochemical etching (field assisted oxidation and dissolution) process active. No nanotubes can be formed if the chemical dissolution is too high or too low [1].
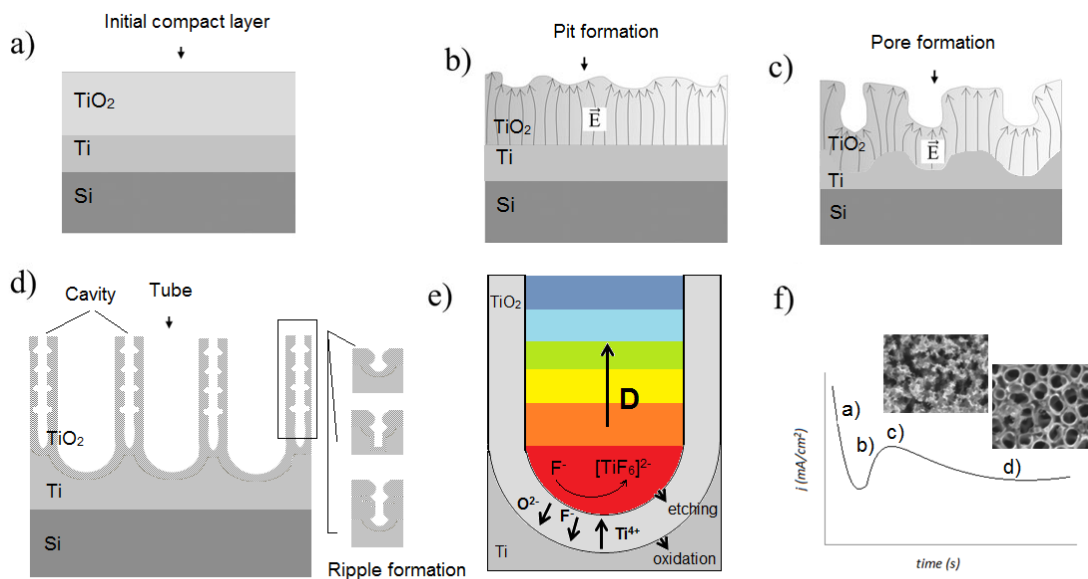
**Figure 4.3** Schematic representation of growth mechanism of TF-TNAs on silicon in electrochemical anodization: (a) formation of the compact anodic oxide; (b) local field distribution correlated to the surface morphological fluctuations; (c) initiation of the pore growth due to the field-enhanced dissolution; (d) pore growth to form tubes in steady-state conditions; (e) overall growth mechanism including oxidation and etching steps (f) Current-time curve monitored during the electrochemical growth in aqueous solution and the corresponding effect on morphology of the film shown in FESEM images. Images (a) to (d) were reprinted with permission from Ghicov et al. [93]. Copyright 2009 RCS Publishing group.

In later growth stages, reactions continue in a steady-state condition under a competition between the tube growth at the bottom and chemical/electrochemical dissolution (Eq. 4.3 and 4.4) at the top [93]. In the case of aqueous electrolyte, it was

found that these two competing processes are dependent on the anodization temperature. At this point the process becomes diffusion controlled and thereby the growth can become affected by the viscosity of the electrolyte. At temperatures higher than 5 °C, the surface of the nanotubes was found to be covered with some irregular features indicating a higher dissolution rate of the oxide. At low temperature range of 2 to 5 °C, precipitate-free nanotubes were found to be formed at sufficiently low rate of the chemical dissolution of $TiO_2$. A constant field gradient is established in the bottom of the tube that determines ions transport resulting in development of the diffusion profile (D) within the tube as shown in Figure 4.3 (e)). By monitoring the current changes during the anodization process, one can control the growth process to the optimized condition. The growth mechanism can be summarized in four steps as the following:

Field-assisted oxidation:

$$Ti + 2H_2O \rightarrow TiO_2 + 4H^+ + 4e^- \qquad (4.1)$$

Field-assisted migration:

$$Ti^{4+} + 6F^- \rightarrow [TiF_6]^{2-} \qquad (4.2)$$

Field-assisted dissolution:

$$TiO_2 + 6F^- + 4H^+ \rightarrow [TiF_6]^{2-} + 2H_2O \qquad (4.3)$$

Chemical dissolution:

$$TiO_2 + 6HF \rightarrow [TiF_6]^{2-} + 2H_2O + 2H^+ \qquad (4.4)$$
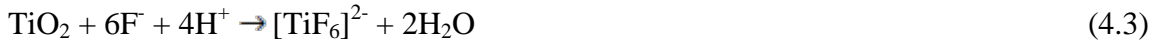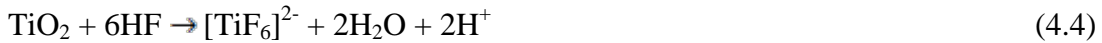
Figure 4.4 shows the FESEM images of smooth as-anodized and the annealed TF-TNAs formed by anodization of thin-film Ti in $NH_4F$-containing organic electrolyte at

room temperature for 1 h at 40 V and after annealing at 420 °C in air. As shown in Figure 4.4 (a), the TF-TNAs are grown to ~ 1.3 ± 0.01 µm (out of 1.6 ± 0.01 µm) during 1 h anodization time. The morphology of the annealed organic TF-TNAs is shown in Figure 4.4 (c-e). By looking from top to cross-sections near the bottom, slight changes in the diameter to ~ 80 nm and the wall thickness to ~ 15 nm can be observed. This can be related to lower concentration of fluoride ions in the electrolyte inside the tubes close to the tube ends and the corresponding effect on the etching rates and thus the thinning process at the tube walls. The inset in Figure 4.4 (e) shows a photograph of the annealed TF-TNAs on a silicon piece.

Using organic electrolytes, well-shaped circular and longer nanotubes can be obtained at room temperature as compared to aqueous electrolytes. In fact, lower dissolution rates of the nanotubes in the presence of low water content organic electrolyte results in the formation of smooth walls and allows for long growth times for the growth of long nanotubes. This is particularly important in growth of thin-film nanotubes on a substrate, as thin-film nanotubes are more prone to be dissolved in HF-based aqueous solutions, thus, leaving less chance for the nanotubes to grow longer. This has been also reported in the case of the growth of nanotubes on Ti foil due to very high rate of chemical dissolution of $TiO_2$ which results in the growth of the nanotubes only up to a maximum length of 1 µm [95].
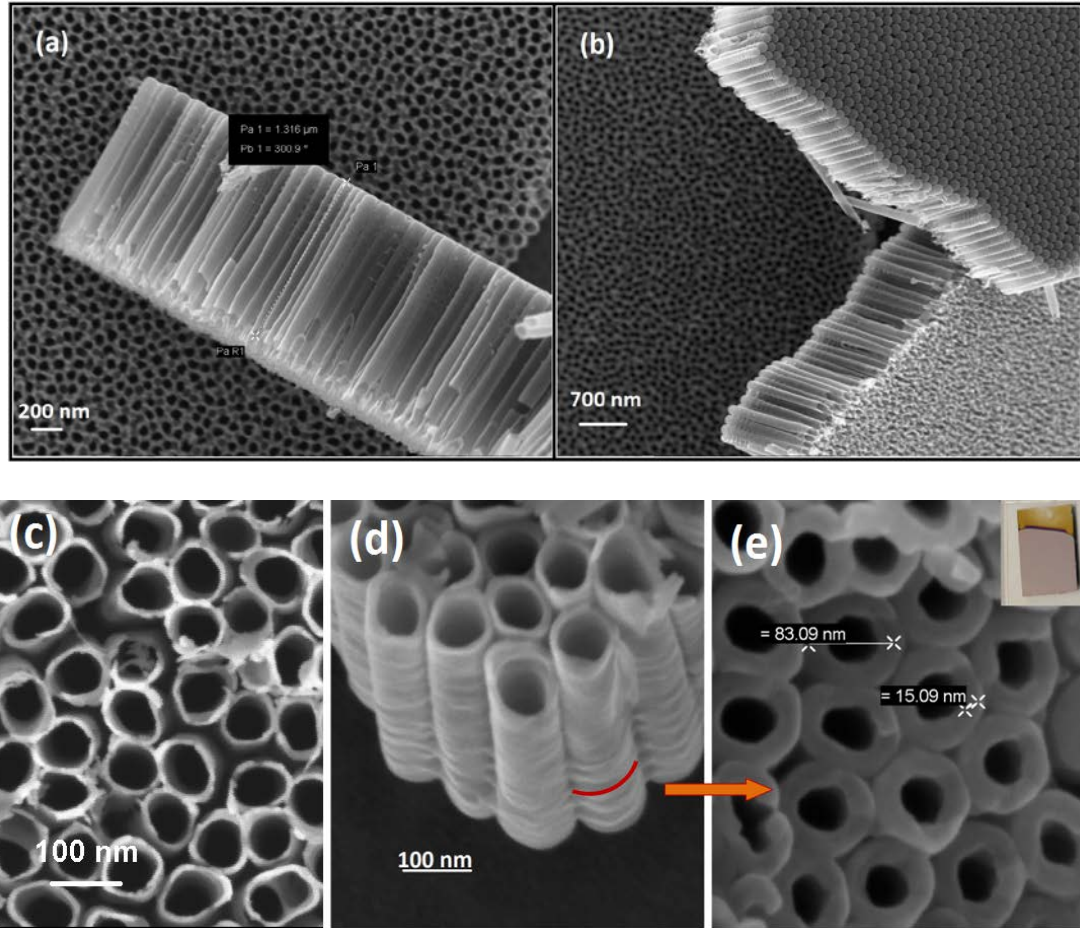
**Figure 4.4** (a) and (b) FESEM images of the as-anodized organic TF-TNAs showing the topside, cross-section and backside of the nanotube arrays. (c), (d) and (e) FESEM images of the annealed organic TF-TNAs showing slight changes in the wall thickness from top to cross-sections near the bottom. Inset is a photograph of the annealed TF-TNAs sample.

As mentioned, the water content in the electrolyte affects both the growth (oxide formation) and etching (oxide dissolution) rates of the nanotubes if the formed metal fluorides are water-soluble. A striking effect of the water content is that smooth tube walls are obtained for low water content, whereas side wall ripples are formed at higher

contents [96]. As can be seen in Figure 4.4, the sidewalls of the organic TF-TNAs contain some ripples formed approximately at 1/3 of the length from the bottom side of the nanotubes. This is opposed to what is observed in aqueous TF-TNAs where the entire nanotube (with shorter length) is continuously and uniformly exposed to $F^-$ ions leading to the formation of ripples at the entire sidewalls. This effect is clearly evident from the TEM images of the aqueous and organic TF-TNAs samples shown in Figure 4.5. The reason for this effect is that for higher water contents, the fluoride-rich layer between the tubes shows a faster etching speed (chemical dissolution rate) than the growth speed of the tubes into the underlying substrate; since the $F^-$ ions are soluble in the water content of the electrolyte and that water has lower viscosity than the ethylene glycol, such higher fluoride containing medium can easily diffuse between the nanotubes walls and start the formation of small cavities. Thus, owing to the higher migration velocity of fluorides compared with $O^2$, the chemical dissolution rate of the oxide is locally increased in those thinned regions which results in additional local etching of the nanotubes at their sidewalls leading to formation of bands/ripples in the walls of the nanotubes.
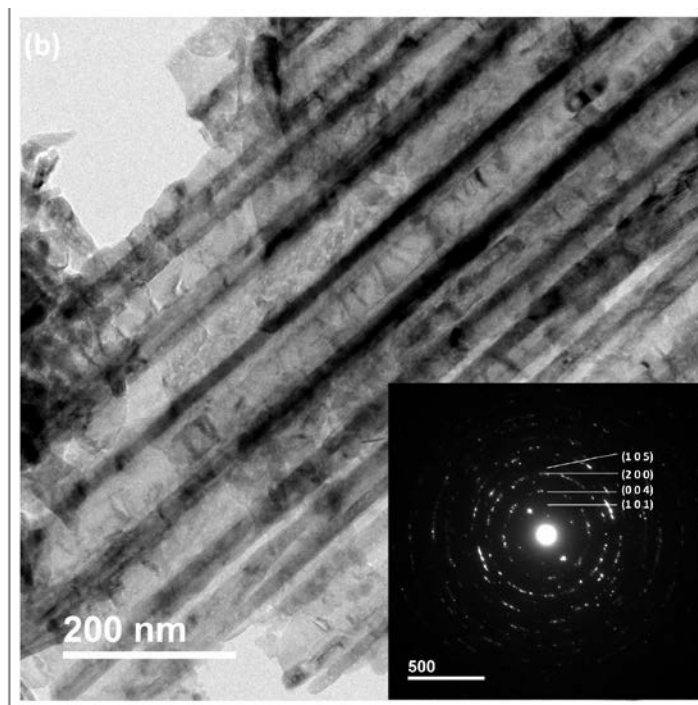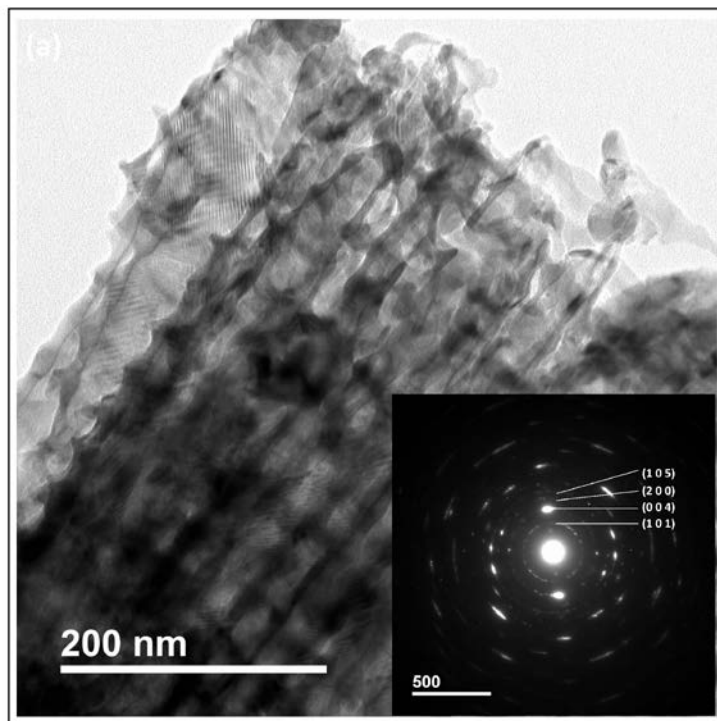
**Figure 4.5** TEM Images of (a) aqueous and (b) organic TF-TNAs and the corresponding diffraction patterns.

Figure 4.5 (a) shows the TEM image of the crystalline TF-TNAs formed in aqueous electrolyte with ripples formed on the entire length of the tubes. In the case of organic TF-TNAs (Figure 4.5 (b)), the sidewalls are formed as straight and smooth lines with no gap in between. Note that the bottom sides of these nanotubes with small fraction of ripple are not shown in this image. The diffraction patterns shown in the insets reveal the polycrystalline nature of the nanotubes with the (101), (004), (200) and (105) planes corresponding to the tetragonal titania anatase in both samples. In the case of aqueous TF-TNAs, the diffuse diffraction spots in the pattern indicate the presence of lattice disorder and defects in the structure. However, in the case of organic TF-TNAs, the presence of distinct diffraction spots confirms the presence of perfect crystals.

In order to study the crystallization and annealing behavior of the anodized TF-TNAs, in-situ high temperature glancing incidence X-ray diffraction (HT-GIXRD) was used to detect the information about the crystalline phases only from the film. The as-anodized organic TF-TNAs sample was heated from room temperature to 450 °C at heating rate of 1 °C/min in air and the XRD patterns were recorded using a glancing angle of 1° at different temperature increments from room temperature up to 450 °C. The sample was then annealed at 450 °C for 4 hours followed by recording the XRD patterns after annealing at 450 °C and cooling down to room temperature, at 25 °C. As shown in Figure 4.6, the crystalline anatase $TiO_2$ starts to form at 350 °C with the main characteristic peak of (1 0 1) plane at diffraction angle of 25°, and those of (0 0 4), (2 0 0) and (1 0 5) planes shown at 36°, 48° and 54° (ICDD PDF 01-071-1176), respectively. The XRD analysis on both aqueous and organic samples revealed that the onset of

crystallization temperature in TF-TNAs is slightly lower than that of the $TiO_2$ nanotubes (~ 450 °C) grown on Ti film [5].
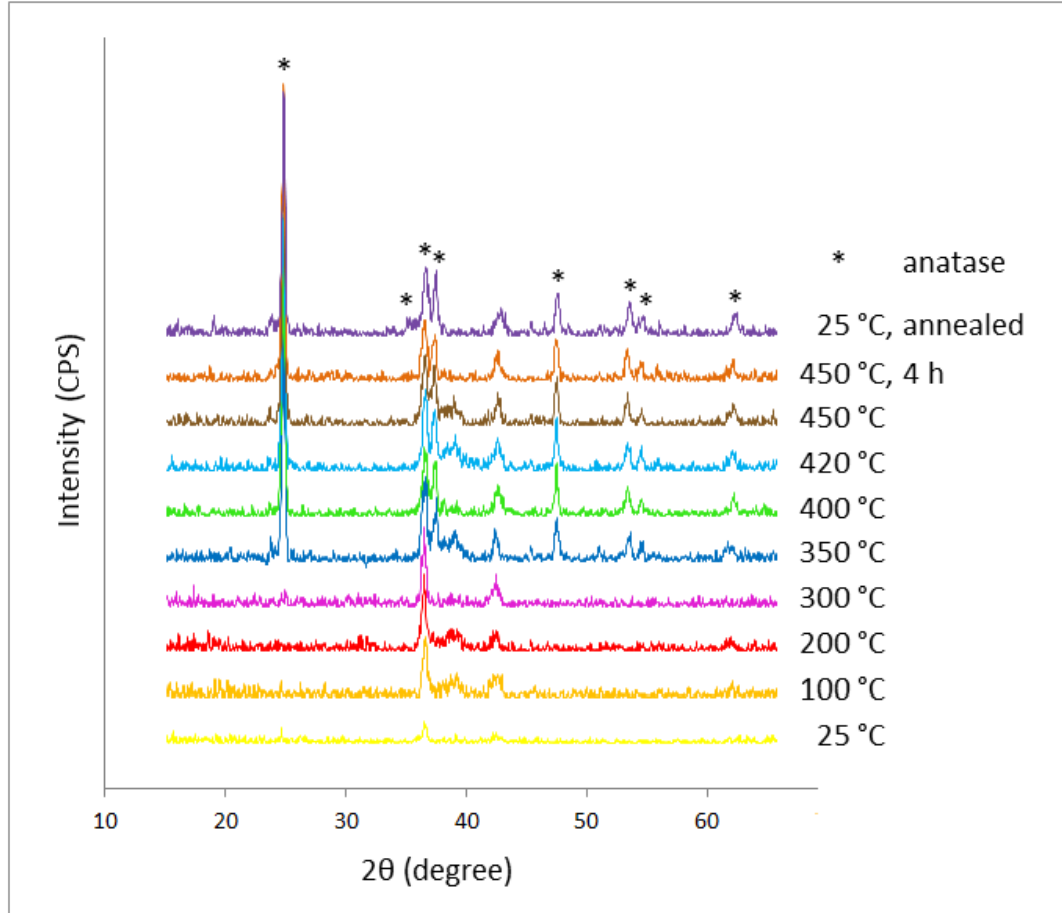


**Figure 4.6** (a) HT-GIXRD patterns of organic TF-TNAs as a function of annealing temperature.

Figure 4.7 (a) and (b) show high resolution XPS spectra of the Ti $2p$ and O $1s$ the organic TF-TNAs sample after heat treatment. The Ti $2p$ with two peaks obtained corresponding to Ti $2p_{3/2}$ and Ti $2p_{1/2}$ photoemission spectra observed at 459.5 and 465.2 eV, respectively, with a spin orbit splitting of 5.7 eV, indicating (as expected) the $Ti^{4+}$

chemical state. Figure 4.6 (c) shows O 1$s$ photoemission spectra at 531 eV which corresponds to the oxygen bonded to Ti$^{4+}$. The shoulder peak on the higher binding energy side of the main O 1$s$ peak at approximately 532.5 eV originates from the adsorption of hydroxyl groups on the surface [97]. The Ti 2$p$ and O 1$s$ peak positions were found to be in agreement with the Ti-O binding energies in TiO$_2$ after annealing confirming the formation of titanium oxide [98].
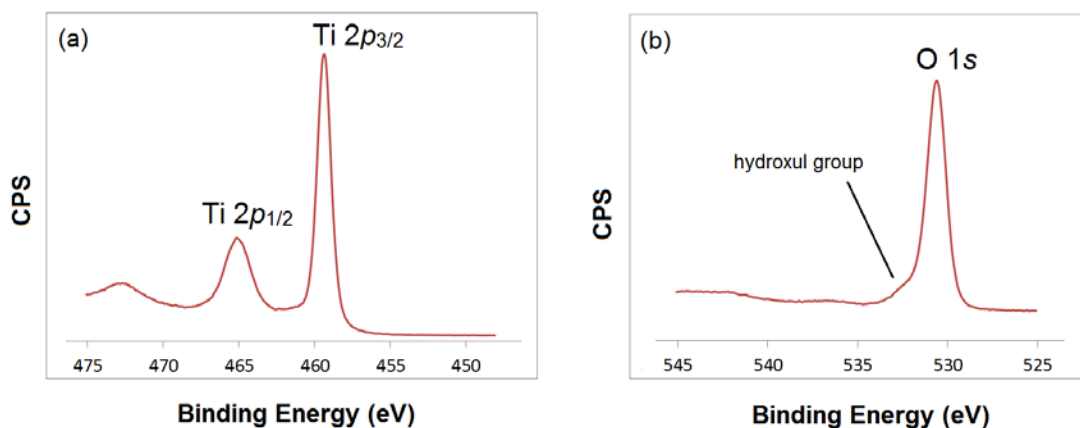


**Figure 4.7** (a) and (b) High resolution XPS spectra of the Ti 2$p$ and O 1$s$ peaks of annealed organic TF-TNAs sample.

## 4.3 Growth Mechanism of Thin-Film TiO$_2$ Nanotube Arrays on 3D FIB Micropatterned Isolated Islands

In order to investigate the growth mechanism of TiO$_2$ nanotubes on 3D isolated islands, the sputtered Ti film was patterned using the FIB before the anodization. The patterned thin-film was then anodized under the same conditions used for synthesis of the organic TF-TNAs sample. Figure 4.8 shows the FIB micropatterned cylindrical and cubic arrays of isolated 3D islands, each with a volume of ~78.5 and ~100 µm$^3$, respectively,

on Ti films. The thickness of the Ti film is ~1.6 μm which can be distinguished from the Si substrate based on the contrast in the SEM image in Figure 4.8. The presence of small cracks on the surface is due to the local heat generated from the high energy gallium ion bombardment [99].

Formation of the $TiO_2$ nanotube array is influenced by three main factors. In 3D isolated islands, the Ti layer is in electrical contact with conductive substrate (silicon) only along the base and not at the sidewalls; thus, the growth is only guided by the charge path combined with the distribution of the electrical field in the Ti layer underneath. The EDS elemental map and chemical composition of the $TiO_2$ islands after anodization are shown in Figure 4.9. According to this map, presence of Ti and O only on the patterned areas versus the Si in the milled area confirms that the patterned regions are perfectly isolated from their surroundings. A small non-uniformity in the Si map is observed which is due to the presence of Ti debris inside the channels as a result of milling process.
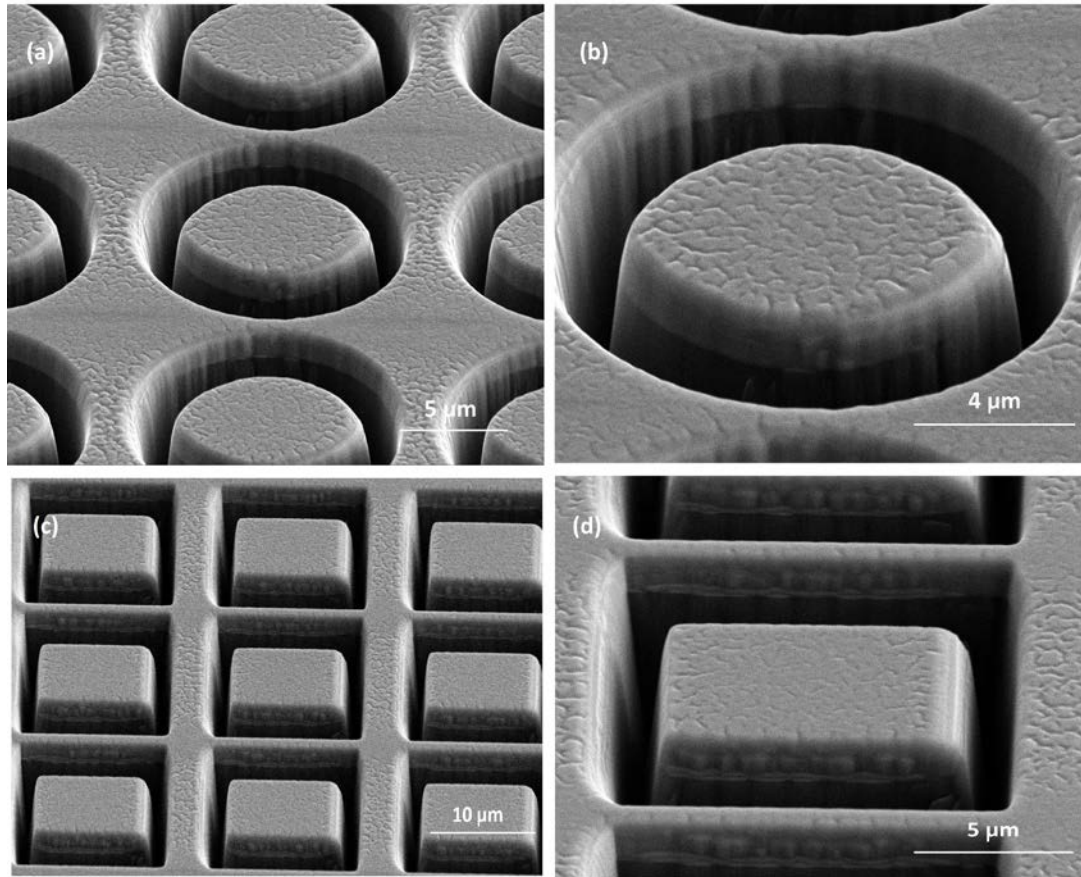
**Figure 4.8** (a-d) Cross-section view FESEM images of the FIB micropatterned 3D cylindrical and cubic arrays of isolated 3D islands at different magnifications.
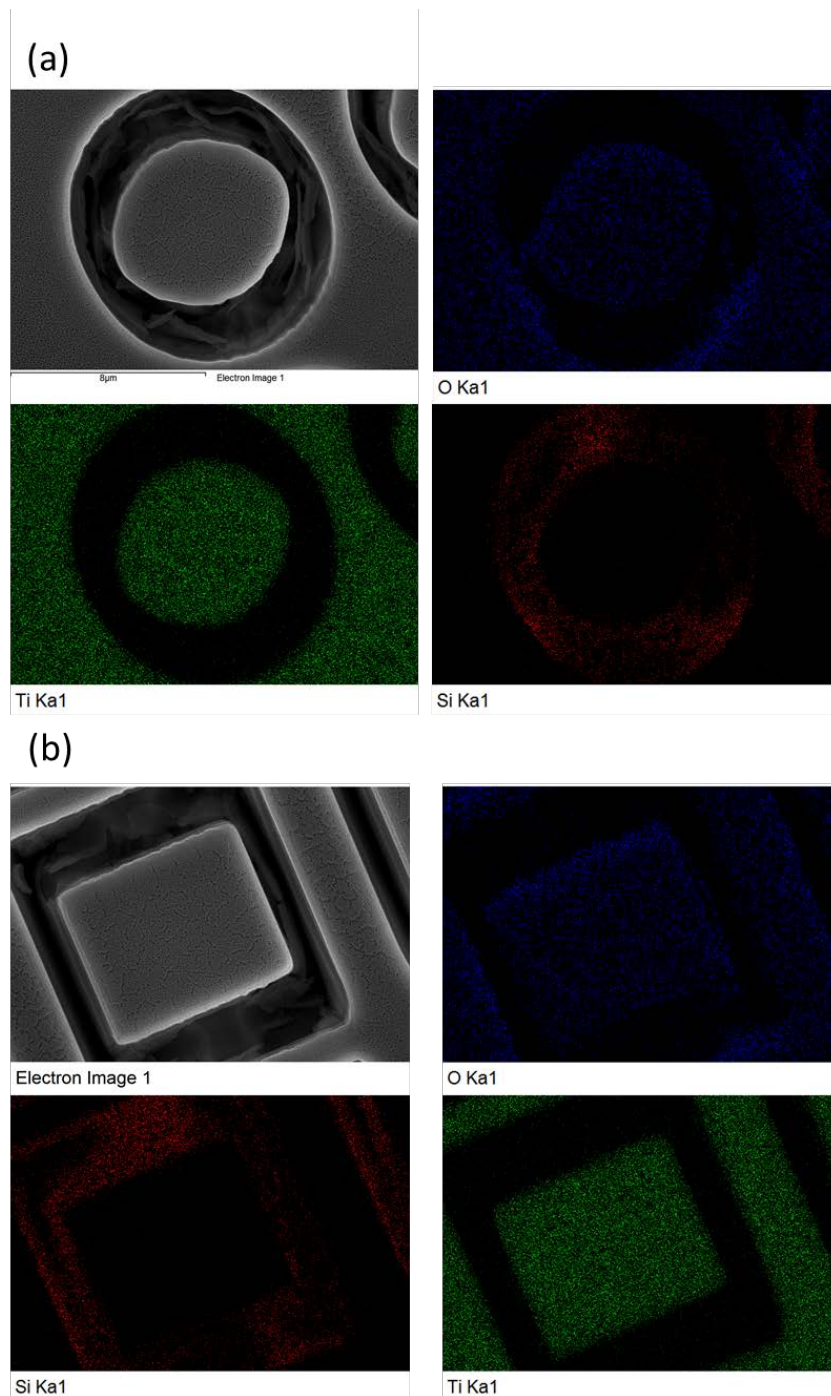
**Figure 4.9** Top-view FESEM images and the corresponding EDS elemental map of as-anodized TF-TNAs grown on (a) cylindrical and (b) cubic FIB micropatterned 3D islands which confirms electrical isolation of the patterned region from the surroundings.

Figure 4.10 shows the FESEM micrograph of the as-anodized TF-TNAs grown on net-shape micropatterned cylindrical and cubic islands at different magnifications. Uniform growth of the nanotubes can be observed on both types of geometries, particularly, at the edges and the sidewalls of the islands. Moreover, the porous surface of the nanotube arrays is extended from the top to the sidewalls of the islands.
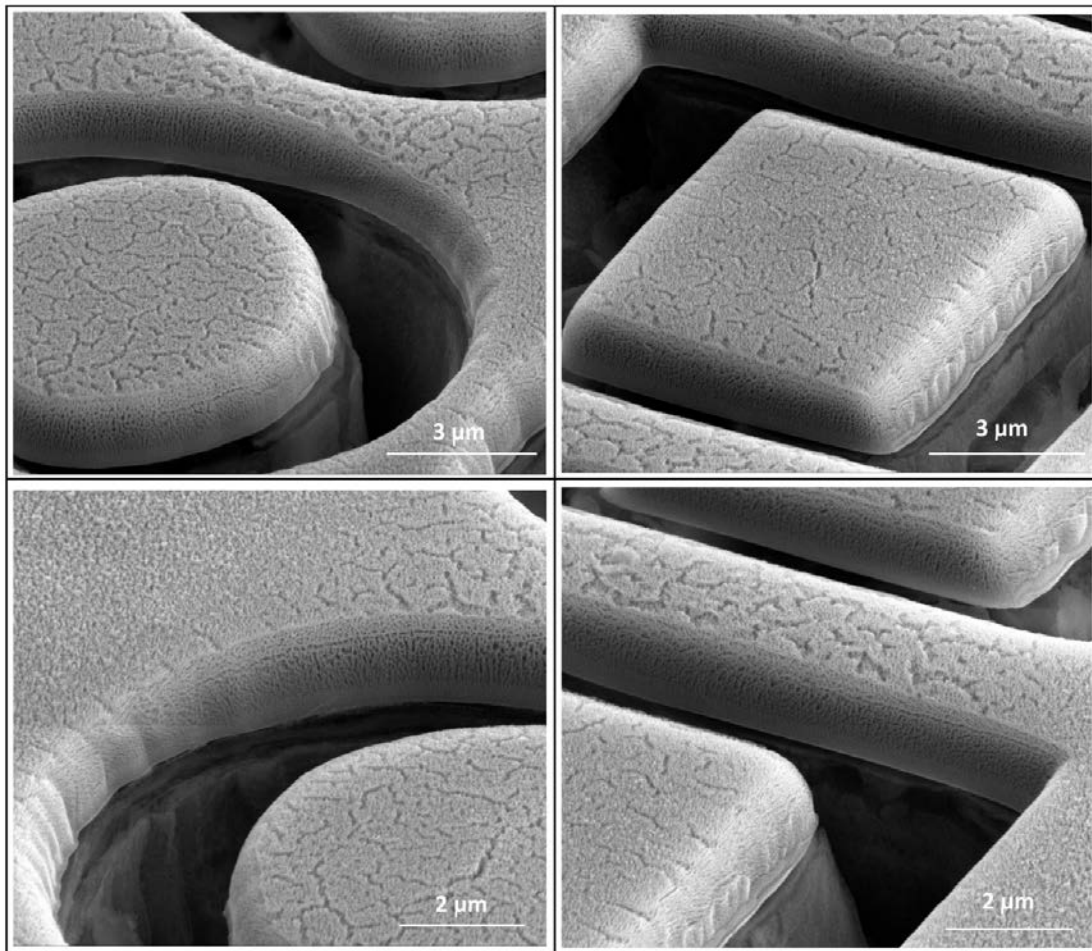


**Figure 4.10** (a-d) Cross-section view FESEM images of the as-anodized FIB micropatterned 3D islands at different magnifications.

In order to view the growth morphology of nanotubes at the sidewalls of the islands, a close-view FESEM micrograph of typical annealed TF-TNAs on cylindrical island is taken by making a cut-section in the middle of the island and at the edge. The morphology of the nanotubes on the curved surface was seen to be strongly dependent on the corresponding electric field distribution. As seen in Figure 4.11 (a), the cut-section view in the middle of the island reveals the formation of vertically-oriented nanotubes as expected. Clearly, due to the excess of $O^{2-}$ and $F^-$ ions in the electrolyte adjacent to the surfaces of the 3D islands at the top and sidewalls, growth of $TiO_2$ nanotubes involves initially with formation of porous structure via fast diffusion of the $O^{2-}$ from the surfaces and oxidation of Ti to $Ti^{4+}$; this step competes later with dissolution of $TiO_2$ by incorporation of the $F^-$ ions in the growing $TiO_2$ lattice which forms the water-soluble $TiF_6^{2-}$ complexes. Meanwhile, the growth is controlled by the distribution of electrical field gradually from vertical to horizontal direction. It is known that at electrostatic equilibrium, the electric field upon the surface of a conductor is directed entirely perpendicular to the surface [100]. It is also known that on the surface of an irregularly-shaped conductor, the charge density ($\sigma$) is the highest at locations along the surface where the object is most curved such as at sharp points or edges. According to Gauss's Law, the field intensity ($E$) is high just above a sharp point with a small radius of curvature ($R$). This can be shown through the following relations:

The potential on the surface of a sphere of radius $R$ is:

$$V = \frac{1}{4\pi\varepsilon_0}\frac{Q}{R}$$

(4.6)

The surface charge density ($\sigma$) on the sphere is also related to the charge ($Q$) as the following:

$$Q = 4\pi R^2 \sigma \qquad (4.7)$$

Thus,

$$V = \frac{1}{4\pi\varepsilon_0} \frac{4\pi R^2 \sigma}{R} = \frac{R\sigma}{\varepsilon_0} \qquad (4.8)$$

where, $\varepsilon_0$ is the permittivity constant of the dielectric material surrounding the charge.

Solving for $\sigma$, we obtain:

$$\sigma = \frac{\varepsilon_0 V}{R} \qquad (4.9)$$

and hence, the electric field will be:

$$E = \frac{\sigma}{\varepsilon_0} \qquad (4.10)$$

As the surface starts to curve on the edges, the nanotubes tend to gradually orient according to the surface curvature while they are still interconnected at the roots. In fact, this orientation results from deflection of the nanotubes on the walls of islands guided by the change in the direction of electric field normal to the surface plane and outward to the surface in such a way that the open side of the nanotubes is always in the direction of the surface normal while its closed end is connected to the $TiO_2$ barrier layer (Figure 4.11 (c)). While the ion diffusion is uniformly possible from each side of the island walls, the

larger electrical field at the edges of curved sidewalls of the islands results in concentration of F$^-$ ions at the edges between the sidewalls of the islands and their surface; thus, the TiF$_6^{-2}$ dissolution competes with the TiO$_2$ formation and results in formation of a strip of nano-porous structure at the edges [93]. Schematic of Figure 4.11 (d) illustrates the growth morphology of deflected nanotubes under applied electric field as we get close to the sidewalls of the islands.
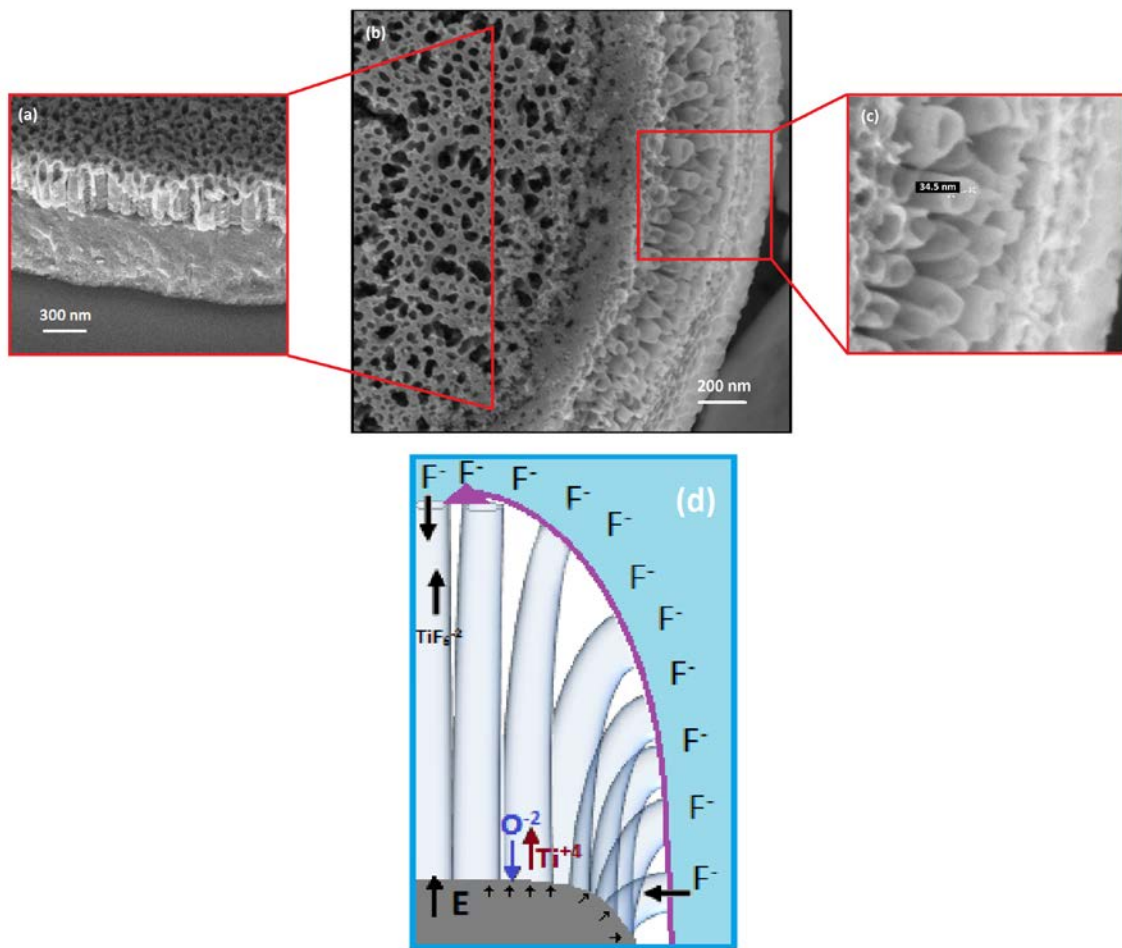


**Figure 4.11** (a) Cross-section view FESEM micrograph of the marked line in (b) which shows top view FESEM micrograph of the TiO$_2$ nanotube arrays in cylindrical island after annealing. (c) High magnification FESEM micrograph of the marked area on (b)

showing gradually deflecting nanotubes grown on the sidewall of the island. (d) Schematic showing the mechanism of growth of deflected nanotubes under applied electric field.

## 4.4 Conclusion

Electrochemical growth of self-organized TF-TNAs on silicon substrate via anodization of sputtered Ti on silicon is shown through two different routes. Vertically-oriented nanotube arrays with average diameter of ~30 nm and length of ~1.5 µm are synthesized at different potentials and growth times in aqueous and organic based types of electrolytes. It was shown that the growth of TF-TNAs in aqueous HF based electrolyte is only possible at temperature below 5 ºC which adds to the complexity of the process in comparison to the use of organic based $NH_4F$ electrolyte. The fabrication and growth morphology of TF-TNAs on 3D isolated islands was successfully demonstrated using a one-step focused ion beam (FIB) technique. The effect of electric field distribution on the growth morphology of TF-TNAs on 3D isolated areas was studied. It was found that the field-enabled transport of mobile ions results in formation of deflected nanotubes on the sidewalls of the islands. This work demonstrates the use of the FIB technique as a simple, high resolution and mask-less method for high aspect ratio etching for creation of isolated islands and shows great promise toward the use of the proposed approach for the development of metal-oxide nanostructured devices and their integration with micro and nano-electromechanical systems (MEMS/NEMS) and integrated-circuit (IC) devices.

# CHAPTER 5

# FINE-TUNING THE ELECTROCHEMICAL PROPERTIES OF TiO$_2$ NANOTUBE ARRAYS BY DOPING

## 5.1. Overview

Among different crystal structures and morphologies of TiO$_2$ materials, oriented anatase nanotube arrays show the highest activity for photocatalysis as well as solar energy conversion efficiency [1, 101]. One major challenge regarding the use of these nanostructures in photochemical applications is the large band gap of TiO$_2$ which makes it useful only for excitation < 400 nm [102]. Therefore, strategies have been applied for realizing the TiO$_2$ for visible and thus solar light response. Two key approaches to achieve this are dye-sensitization and so-called doping with species that essentially reduce the band gap of the material [22]. By introducing dopants of similar or different ionic radius, the lattice structure can be tuned which may further tune the electronic structure and optical behavior by introducing electronic states in the gap. Generally, the major challenge in analysis of doping mechanism in doped material is the detection of dopant which is an extremely small fraction of the host material. The underlying hypothesis in this chapter is that the incorporation of strontium in the TiO$_2$ lattice has been made possible via one-step in-situ electrochemical anodization and annealing process which has resulted in enormous enhancement in photocatalytic activity of the material. Extensive study of the doped TiO$_2$ nanotubes has been accomplished through the use of state-of-the art bulk analysis and surface spectroscopy techniques such as X-

ray crystallography and X-ray absorption spectroscopies to understand the doping mechanism. On the other hand, the use of microscopy techniques such as scanning electron microscopy (SEM), and atomic resolution transmission electron microscopy (TEM) has enabled reliable identification of success or failure of doping as well as the mechanism involved. The experiments in this chapter will explore possible mechanisms of the strontium doping into the $TiO_2$ structure, accompanied by investigation of the induced nanostructural changes in the bulk and surface structure of the nanotubes. With this aim, we compare the structural and optical properties of the un-doped and doped $TiO_2$ nanotubes at different concentrations.

## 5.2 *In-situ* Synthesis and Characterization of Strontium-Doped TiO₂ Nanotubes

Arrays of closed-end highly-ordered vertically oriented $TiO_2$ and strontium doped nanotube arrays (with an average inner diameter of ~100 nm) were grown using the potentiostatic anodization process on 2 cm x 2 cm strips of polished titanium (0.25 mm thick, Alfa Aesar) in a two-electrode cell configuration as described in section 3.1.1. Prior to anodization, the strips were rinsed in an ultrasonic bath of ethanol and cold DI water for 1 h and 15 min, respectively. Pt mesh was used as the counter electrode and located 2 cm away from the Ti electrode immersed in the electrolyte. Samples were anodized and doped in-situ in an electrolyte containing 0.1 M $NH_4F$ mixed with 0.02 M, 0.04 M, 0.06 M anhydrous strontium hydroxide (Sr $(OH)_2$), 99% (from Pfaltz and Bauer Inc.) at 20 V for 3 h at 20 °C. The pH of the electrolyte was controlled by addition of 0.1 M $H_3PO_4$ to the solution. Subsequently, samples were annealed at 450 °C for 4 h with heating and cooling rates of 1 °C/min. After anodization, the samples were ultrasonically rinsed in DI water and dried under a stream of nitrogen.

Table 5.1 shows the Sr content in the TiO$_2$ nanotubes samples that are determined based on ICP MS data averaged over two measurements on annealed samples and from XPS measurements over 2 different spots on the surface of two sets of as-prepared and annealed samples, respectively. The undoped TiO$_2$ and the lowest to the highest strontium containing samples are named hereafter T, ST1, ST2 and ST3, respectively. Note that the dopant concentrations determined based on XPS analysis are considered as the basis for examination of surface sensitive properties while the ICP-MS results are used for bulk properties evaluation.

**Table 5.1** Sr content in (atomic %) in doped TiO$_2$ nanotubes samples from ICP MS and XPS measurements shown over the full range.

| Sample \\ Method | | ST1 | ST2 | ST3 |
|---|---|---|---|---|
| **Solution Concentration (M)** | | 0.02 | 0.04 | 0.06 |
| **ICP-MS[*] (At. %)** (number of repeat measurements: 2) | Annealed | 1.5 ± 0.1 | 3.0 ± 0.2 | 8.0 ± 0.1 |
| **XPS (At. %)** (number of repeat measurements: 4) | As-anodized | 1.12 ± 0.02 | 3.9 ± 0.2 | 4.6 ± 0.44 |
| | Annealed | 0.82 ± 0.03 | 1.09 ± 0.03 | 1.34 ± 0.09 |

[*]ICP-MS performed by Mr. Gene Weeks at UGA Lab for Environmental Analysis

It is worth noting that a particular discrepancy was observed between the effective content of Sr$^{2+}$ within the samples before and after annealing with their initial concentrations in the solution during the anodization process. Moreover, the as-anodized samples show higher values of the dopant on the surface compared to the annealed ones

(as measured by the XPS), which could be due to further diffusion and distribution of the dopant from the surface toward inside the film along the nanotubes.

## 5.2.1. Effect of Processing Conditions on Morphology of $Sr^{2+}$-Doped $TiO_2$ Nanotubes

Figure 5.1 shows a typical FESEM top-view image from the surface and backside of the annealed $Sr^{2+}$-doped $TiO_2$ nanotubes grown in electrolyte containing 0.04 M $Sr(OH)_2$ at 20 V for 3 h. The surface morphology of the nanotubes was found to be unchanged after doping. The tube diameter and the tube length were $100 \pm 10$ nm and ~1 µm, respectively.
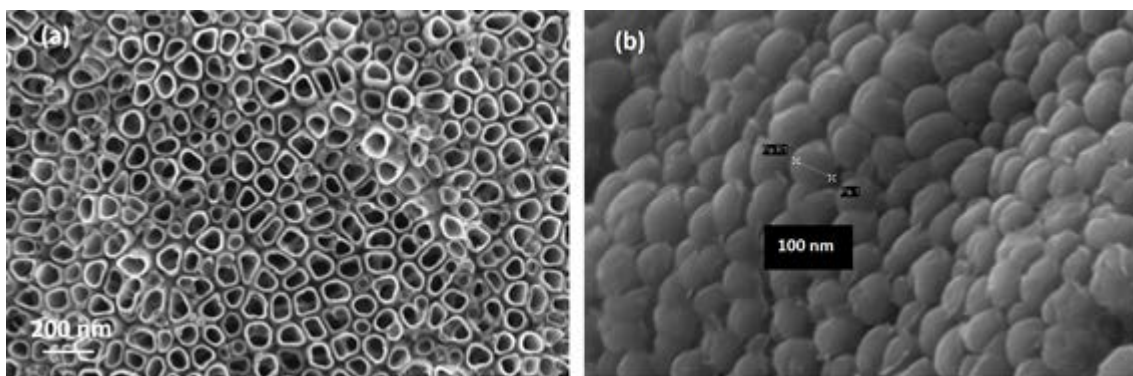


**Figure 5.1** (a) Typical top-view FESEM image of the surface and backside of an annealed $Sr^{2+}$-doped $TiO_2$ nanotubes (ST2 sample).

However, cross-sectional characterization of the fabricated Sr-doped $TiO_2$ nanotubes revealed that tube length is a function of the electrolyte pH and the dopant content. This effect is shown in Figure 5.2 in which the length of Sr-doped nanotubes is changing from about 0.7 $\mu$m to 1.4 $\mu$m in 0.02 M dopant concentration by changing the electrolyte pH from 2 to 3 (Figure 5.2 (a) and (b)). This effect shows that increasing the

pH of the electrolyte from 2 to 3 resulted in doubling the tube length which can be considered as a factor in the preparation of doped nanotube arrays with different lengths. Grimes and co-workers observed the same trend upon the fabrication of un-doped titania nanotube arrays where longer nanotubes formed in higher pH solutions [5]. Also, slight change (~ 30% decrease) in the length was observed when the dopant content is increased from 0.02 M to 0.04 M. This can be attributed to the consumption of the $F^-$ ions by the dopant atom via formation of $SrF_2$ (with solubility of 0.039 g/100 mL) in the water electrolyte which finally results in decreased concentration of the reacting fluoride in the electrolyte surrounding the nanotubes and as a result lowering the rate of tube growth [103].
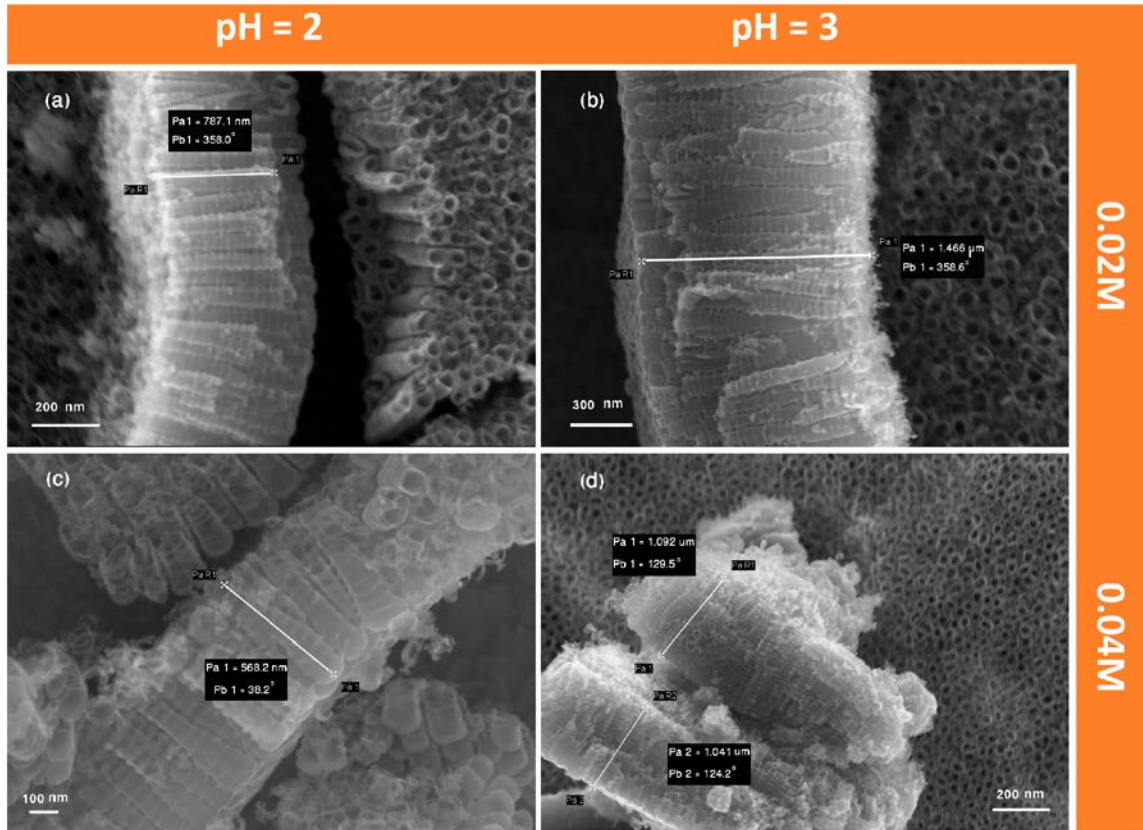
**Figure 5.2** FESEM cross-sectional views of the as-prepared $Sr^{2+}$-doped $TiO_2$ nanotubes for (a) ST1 @ pH = 2, (b) ST1 @ pH = 3, (c) ST2 @ pH = 2 and (d) ST2 @ pH = 3.

### 5.2.2 Study of Doping Mechanism in $Sr^{2+}$-Doped $TiO_2$ Nanotubes

5.2.2.1. Bulk Structural Analysis of $Sr^{2+}$-$TiO_2$ Nanotubes: Effect of Dopant on the Lattice Structure

*5.2.2.1.1 TEM/HRTEM Analysis*

Figure 5.3 shows a typical cross-section view TEM image and the EDS spectrum and the corresponding EDS map of a single $Sr^{2+}$-doped $TiO_2$ nanotube along longitudinal direction. The EDS spectrum reveals the presence of Ti K and Sr L peaks in the doped

sample. Also, the EDS Sr L map extracted based on Sr L line reveals a homogenous distribution of the Sr along the length of the tube. The relative concentration of the Sr based on this peak estimated from the EDS is ranged from 0.2-1 atomic %.
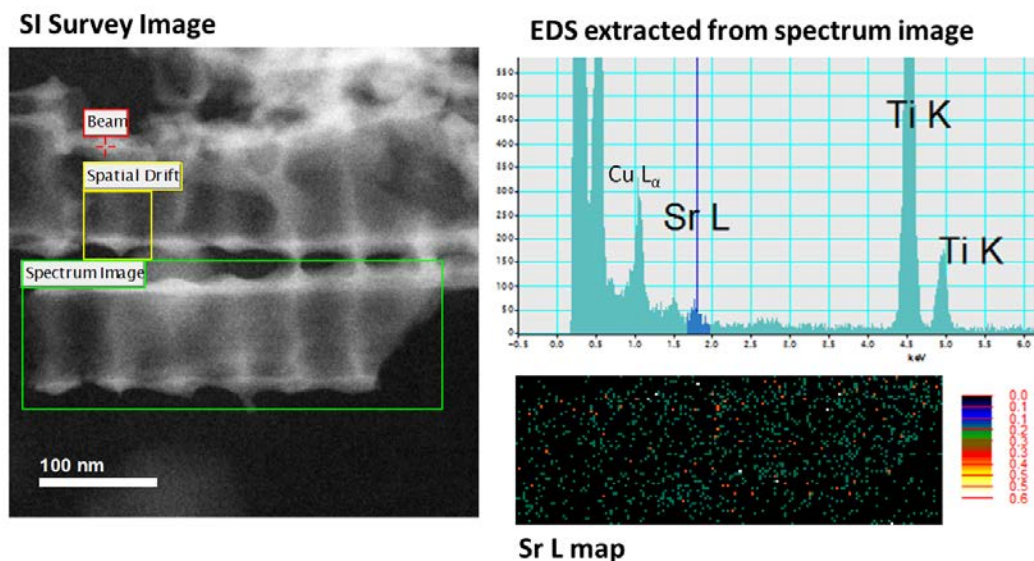


**Figure 5.3** Cross-section view TEM image and the EDS spectrum and the corresponding EDS map of a (annealed) single $Sr^{2+}$-doped $TiO_2$ nanotube (prepared in electrolyte containing 0.04 M $Sr(OH)_2$ and @ pH = 3) along longitudinal direction.

Figure 5.4 shows a closer view of an annealed $Sr^{2+}$-doped nanotube with the corresponding diffraction pattern shown in inset (Figure 5.4 (a)). As shown in this figure, the bulk of the nanotube is composed of a crystalline region in the middle with clear lattice fringes indicating the crystalline structure of the nanotubes. The orientation of the crystals is clearly observed from the diffraction pattern of the middle region with the majority (101) oriented planes observed from the indexing of the fast Fourier transform (FFT) as shown in the inset in Figure 5.4 (b). The HRTEM image and the FFT

reconstructed image in the inset of Figure 5.4 (c) show the *d*-spacing of 0.35 nm which correspond to (101) planes. However, as shown, the crystalline region is encompassed with a fairly thick amorphous layer of ~ 15 nm that extends to the entire length of the nanotube. This amorphous layer is thicker compared with the a few nanometer amorphous layer typically seen in undoped $TiO_2$ nanotubes synthesized similarly in aqueous solution (Figure 5.4 (d) and (e)).
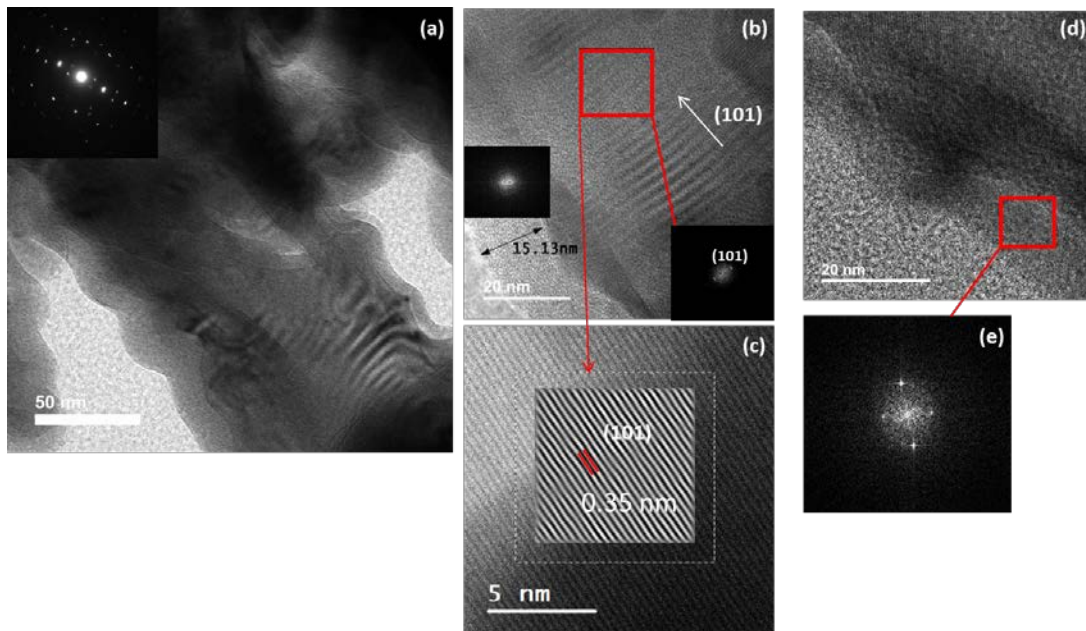


**Figure 5.4** (a) Cross-section view TEM image of annealed ST2 sample and the corresponding diffraction pattern in the inset. (b) A magnified region of (a) showing the preferred orientation of the (101) crystallographic planes in FFT. (c) HRTEM image and the FFT reconstruction of the crystalline region. (d) The TEM image of undoped $TiO_2$ nanotube and the corresponding diffraction pattern of the outer layer in (e).

*5.2.2.1.2 XRD Analysis*

In order to perform detail analysis of the bulk and surface of the doped $TiO_2$ nanotubes, it is required to understand the unit cell and crystallographic structure of anatase. Figure 5.5 shows the lattice structure of the anatase with the lattice parameters denoted by a, b, and c, the $TiO_6$ octahedra and the $R_{ax}$ and $R_{eq}$ (the distances between a $Ti^{4+}$ ion and its nearest and next-nearest neighbor $O^{2-}$ ions, respectively).
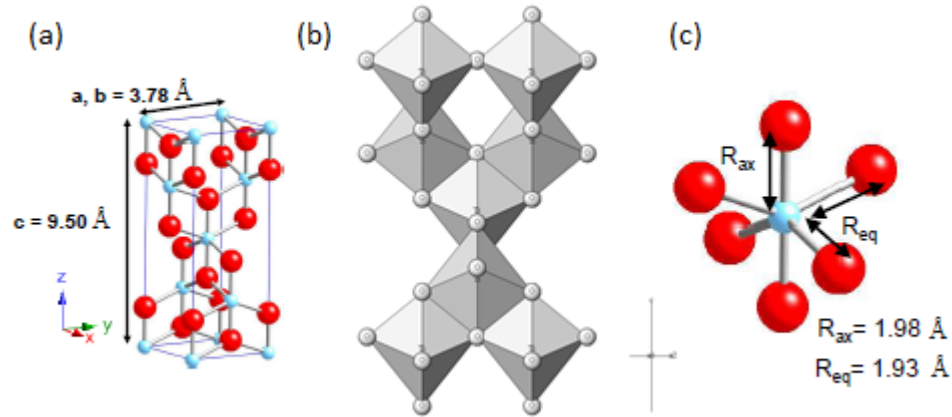


**Figure 5.5** Unit cell (left), crystallographic structure (center) and $TiO_6$ octahedrons (right) of anatase with oxygen in (red) and titanium in (blue). The lattice parameters are denoted a, b, and c, while $R_{ax}$ and $R_{eq}$ are the distances between a $Ti^{4+}$ ion and its nearest and next-nearest neighbor $O^{2-}$ ions, respectively [102].

Figure 5.6 shows the XRD patterns of the annealed undoped (pure) and Sr-doped $TiO_2$ nanotube arrays prepared in electrolyte with three different dopant concentrations at pH = 3. All patterns confirm with reflections from $TiO_2$ anatase phase which crystallizes within the $I4_1/amd$ space group (tetragonal cell) after annealing. No evidence for phase segregation was found from the XRD patterns. Note that the peak position of titanium at $2\theta = 40.5°$ was considered as the reference position for comparison of the undoped and

doped $TiO_2$ samples. In general, as the dopant level is increased, gradual shifts in the lattice parameters of the host material is observed due to the strain induced when the dopant is incorporated into the periodic crystal lattice. According to Vegard's law, the average lattice parameter varies linearly with dopant concentration in the crystal, and typically the deviations from linearity are indications of phase transitions or segregation [104].

Inspecting Figure 5.6, it was found that the anatase (101) peak shifts towards smaller $2\theta$ values with increasing Sr dopant concentration as observed in close-up view of the (101) shown in Figure 5.6 (b). This shift can be attributed to the incorporation of the $Sr^{+2}$ with larger ionic radius (1.18 Å) than that of $Ti^{4+}$ (0.605Å) into the crystal lattice of $TiO_2$. The shift in (103), (004) and (200) peak positions are also shown in Figure 5.6 (c-d). As the concentration of the dopant increases, it is expected that more $Sr^{+2}$ ions are incorporated into the $TiO_2$ crystal lattice and as a result the corresponding peaks are more shifted to the higher angle side. In order to investigate the reproducibility of the XRD measurements, the Table 5.2 shows the two-theta peak positions corresponding to (101) and (004) planes that are obtained from repeated XRD experiments on all samples.
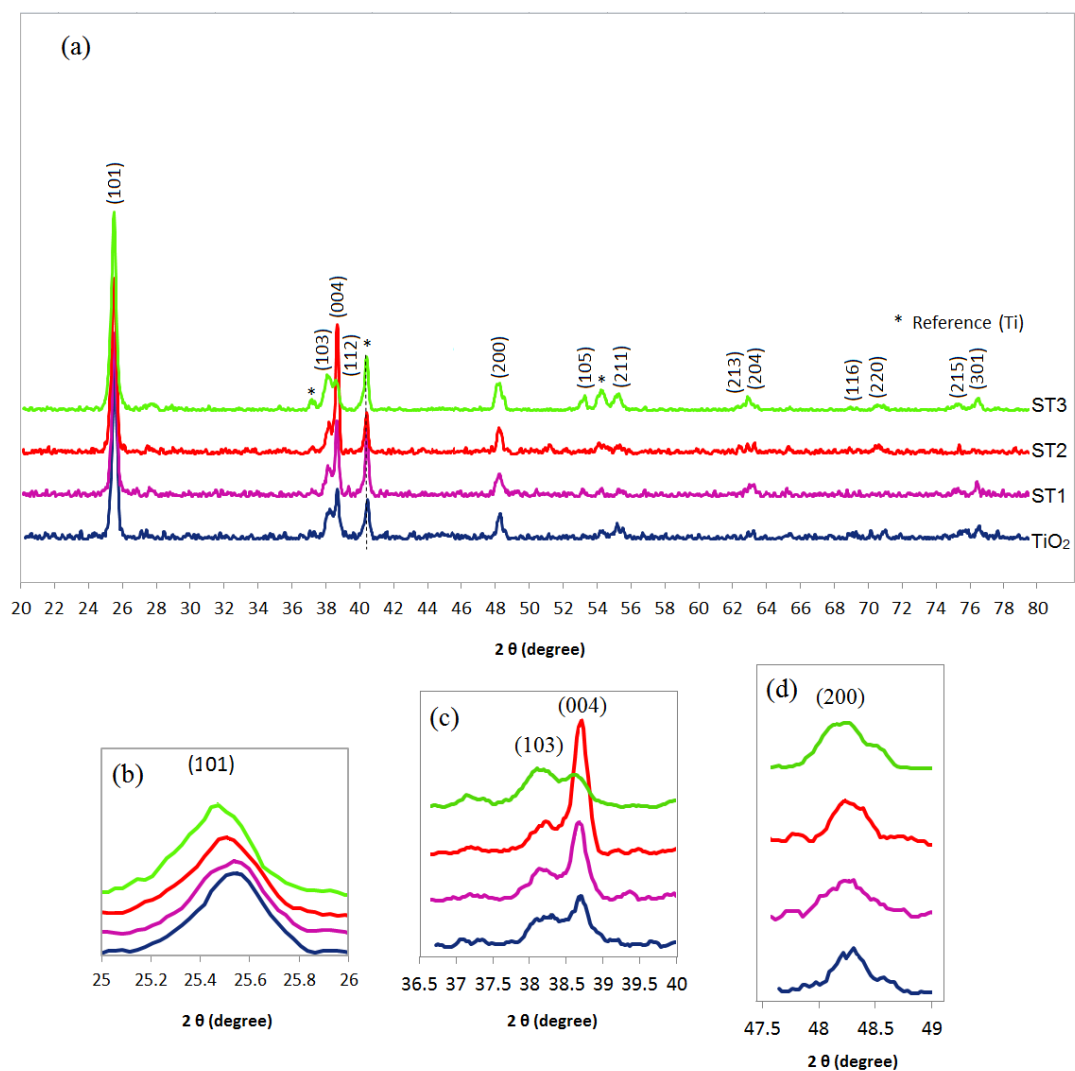
**Figure 5.6** XRD patterns of undoped and $Sr^{2+}$-doped $TiO_2$ nanotube samples obtained at different Sr-dopant concentration and electrolyte pH = 3 shown in (a). Close-up view of (b) (101), (c) (103) and (004), (d) (200) peaks.

**Table 5.2** Two-theta values (in degree) obtained from repeated XRD experiments corresponding to (101) and (004) planes in all samples.

| Experiments | 1 | | | | 2 | | | |
|---|---|---|---|---|---|---|---|---|
| Samples<br>Planes | T | ST1 | ST2 | ST3 | T | ST1 | ST2 | ST3 |
| **(101)** | 25.505 | 25.426 | 25.419 | 25.375 | 25.493 | 25.477 | 25.395 | 25.392 |
| **(004)** | 38.645 | 38.615 | 38.614 | 38.585 | 38.654 | 38.619 | 38.612 | 37.929 |

Based on Scherrer's formula peak broadening is essentially associated with crystallite size and non-uniform strain (micro-strain) due to shifts of atoms from their ideal positions which result in structural strain and disorder in $TiO_2$ crystalline lattice structure. The crystallite size of the undoped and the doped samples were calculated from Scherrer formula. The calculated sizes of the crystallites were found to be changing in the range of 25 nm to 35 nm; however, no trend was observed between the doped samples with respect to the undoped one. The unit cell of anatase $TiO_2$ is illustrated in Figure 5.7 (a). The anatase with tetragonal crystal system is composed of Ti atoms (gray) and the O atoms (red) with lattice parameters of $a = b = 3.7845$ Å and $c = 9.5143$ Å. A 90° rotated view of the unit cell is shown in Figure 5.7 (b) with octahedral interstitial indicated in black circles and the (101) plane in blue.
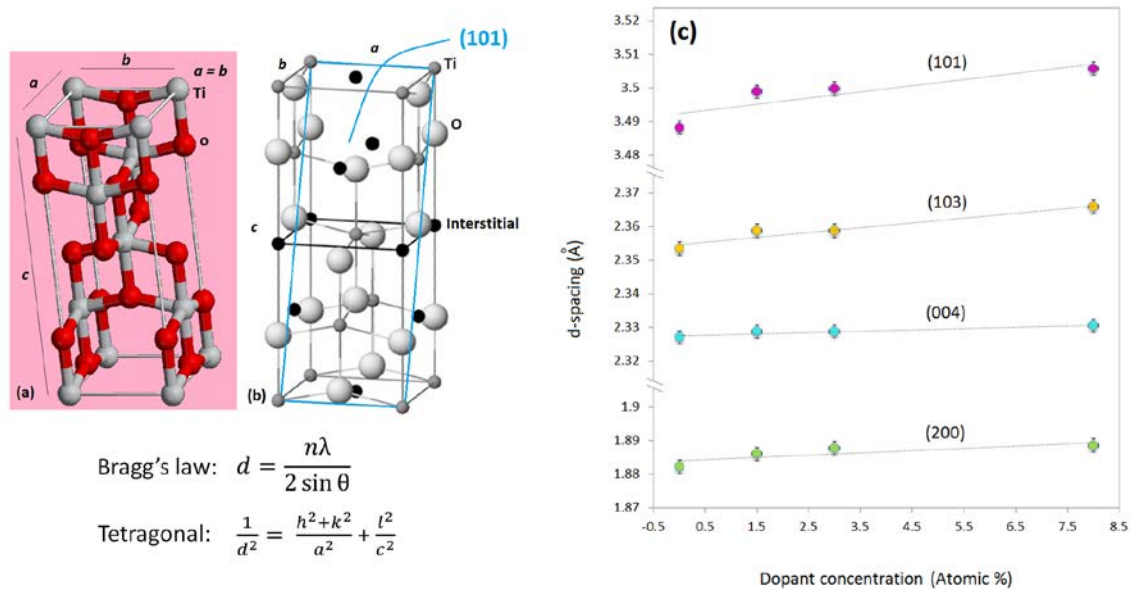
**Figure 5.7** (a) Unit cell of anatase TiO$_2$, Ti (gray) and O (red) spheres. (b) 90° rotated view of unit cell shown in (a) with octahedral interstitial indicated in black circles and (101) plane in blue [105]. (c) Plot of variation of calculated inter-planar *d*-spacing as a function of doping concentration determined from ICP-MS measurements on the bulk.

The change in the *d*-spacing in (101), (103), (004) and (200) planes in doped samples is calculated from the well-known Bragg's law and shown as a function of dopant concentration in Figure 5.7 (c). The main source of error in lattice parameters determination, for X-Ray Diffractometers with Bragg-Brentano geometry, is related to the alignment of instrument (zero 2theta offset and peak position) [106]. This effect is taken into account in our measurements by alignment of the instrument before performing the scans and by using the Ti peak corresponding to the metallic titanium in the substrate as the reference peak for all samples. The accuracy of the measurements was also determined based on the instrument precision of 0.02° measurement for the 2-

theta angle in the Bragg-Brentano geometry, which allows an accuracy of 0.002 Å for the lattice parameters and determination of the error bars. Based on these calculations, it was found that the values of *d*-spacing in all planes increase linearly with the amount of Sr dopant. This can be related to random substitution of the dopant atom in the $TiO_2$ lattice, either for Ti atom or in interstitial sites (black circles) as shown in Figure 5.7 (b).
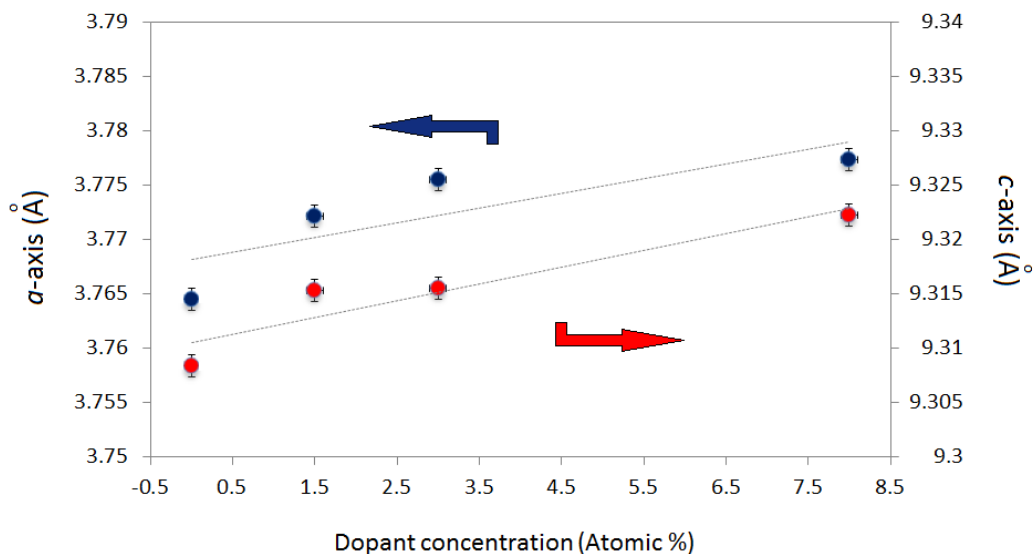


**Figure 5.8** Plot of variation of lattice parameters *a* and *c* as a function of doping concentration determined from ICP-MS measurements on the bulk.

Figure 5.8 shows changes in the lattice parameters *a* and *c* as a function of doping concentration. It was observed that both *a*-axis and *c*-axis have slightly increased with increasing the dopant content compared with that of undoped anatase. Such modification of the lattice cell parameters is an indication of the effective accommodation of the divalent $Sr^{2+}$ cation by the lattice. This linear variation of the cell parameters along both axes is in accordance with Vegard's law which confirms successful incorporation of $Sr^{2+}$

into $TiO_2$ lattice. Note that the *a*-axis and the *c*-axis values were calculated from (200) and (004) planes, respectively.

By looking at the changes in the intensity of (004) peak with increasing dopant content, it was observed that the intensity is increased from undoped sample to ST2. However, a sudden change in the peak intensity can be seen in the (004) reflection in the highest doped sample ST3 (Figure 5.6). Since the (004) reflection is related to changes in dimension along the *c*-axis, it appears that the lattice has slightly distorted along the *c*-axis in ST3 sample.

Based on the above observations from the XRD measurements and the changes in the lattice parameters, it is suggested that the $Sr^{2+}$ has entered the $TiO_2$ lattice either in the interstitial sites or as substitutional for $Ti^{4+}$. No other phase formation was observed from XRD analysis. However, the possibility of grain-boundary segregation and surface phase segregation may also be valid. As such, clustering of strontium in the form of SrO on the sub-nanometer layers on the very top surface of the nanotubes is examined in the following sections thorough surface sensitive techniques and HRTEM in detail.

When dopant ions are larger than those in the matrix, grain boundaries can often accommodate such large ions much more easily because of their more open structures and due to strain energy minimization [107, 108]. Charged dopants (acceptors or donors) cations, during the interaction with the electrostatic fields, established in the near grain boundary regions because of nonstoichiometry at the grain boundaries, tend to segregate to or deplete from the grain boundaries depending on the charge polarity to minimize the total electrostatic energy. On the other hand, if the size of the dopant ions is significantly

different from that of the matrix cations on the substitutional site, considerable strain field is created around the alien ions due to the large ionic mismatch. The high strain energy has to be released in some way for the system to stabilize. Before the solid state solubility of the dopant is achieved, those alien ions can be better accommodated in the grain boundaries than in the bulk [107].

Ikeda and Chiang [109, 110] have investigated the GB segregation of $TiO_2$ which were both explained theoretically and experimentally. Using a pure space-charge model at high temperatures, it was predicted that segregation and grain boundary potential only depended on the net bulk dopant concentration given constant individual defect formation energies and the temperature. At a specific temperature, there existed an isoelectric point where the boundary potential equaled to zero. With assumption of the individual defect formation energies, they found this isoelectric point varied with temperature at specific oxygen partial pressure and slightly lied at the donor-doped composition due to the defects from reduction.

Ling, et al. have also reported the precipitation and identification of second phase(s) in high temperature processing of strontium-doped $TiO_2$ materials [111]. Their observations indicate that ($< 0.5$ mol %), strontium segregates to the grain boundaries to form a second phase of $SrTiO_3$ below the solubility limit. Above 1200 °C, this second phase is continuous; shape instability causes it to break up into discrete particles below 1200 °C. At higher strontium concentration (about 2 mol % Sr), nucleation of $SrTiO_3$ crystallites has shown to occur both inside the $TiO_2$ grains and at the grain boundaries [111]. These observations reveal the possibility of GB segregation of Sr in $TiO_2$, noting

that high sintering temperatures provides sufficient energy as a driving force for movement of the large ion to the GBs.

In our investigation of the incorporation of Sr dopant into $TiO_2$ lattice, the first possible mechanism can be associated to the Sr substitution for Ti atom. The lattice expansion in both directions in all doped samples as well as the slight linear increase in *d*-spacing between (004) and (200) planes indicate uniform changes in the lattice. Due to a significantly higher effective ionic radius of $Sr^{2+}$ (1.18 Å) than that of $Ti^{4+}$ (0.605Å), the presence of Sr either as a substitutional or interstitial ion, seems very possible to result in the lattice expansion in all directions.
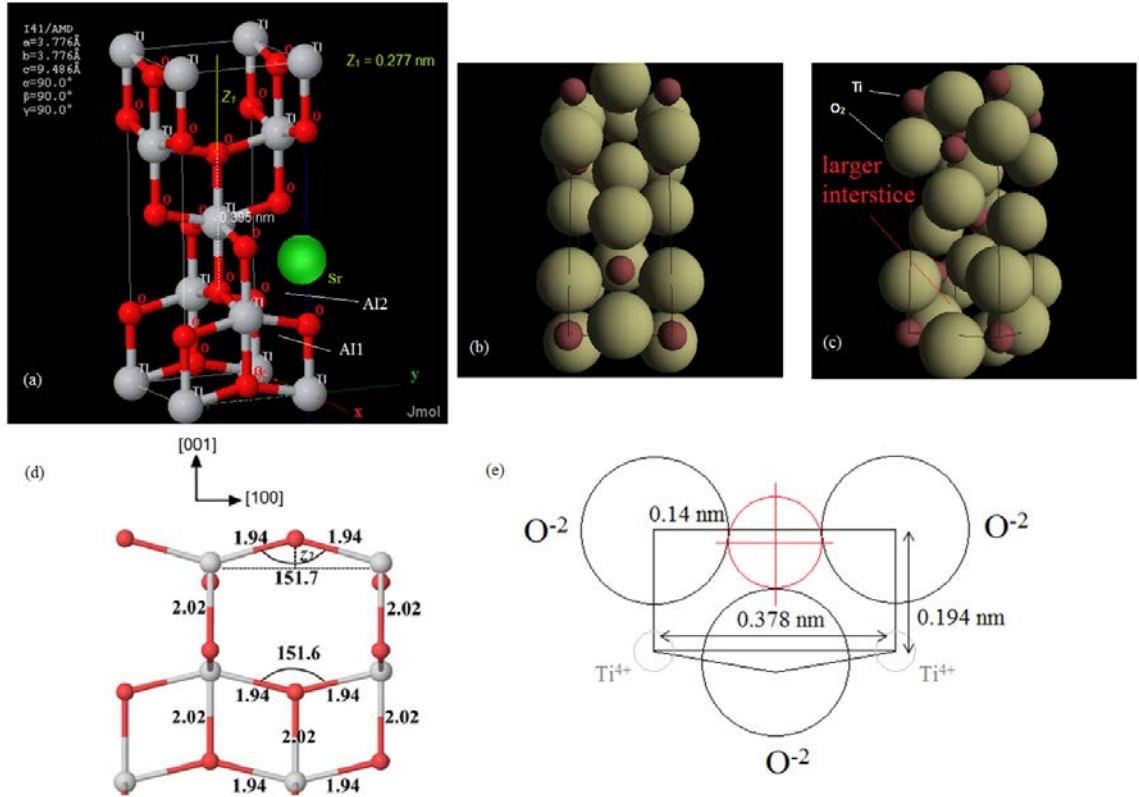
**Figure 5.9** The 3D unit cell of anatase (a) with specified O-Ti-O bond length in the middle and the void length along the *c*-axis. (b) and (c) Hard-sphere model of the anatase lattice at different views showing the larger interstitial site. (d) Side views of the atomic arrangements of the anatase $TiO_2$ (001)-2×2 structure. Ti and O atoms are denoted by light gray and red (dark) balls, respectively. All bond lengths and angles on this image are given in angstroms and in degrees, respectively. (e) (200) plane with $O^{2-}$ anions and $Ti^{4+}$ cations positions and the interstitial site in red. Image (d) reprinted with permission from Mete et al. [112, 113]. Copyright 2012 from American Physical Society.

According to Steveson et al., there are two interstitial sites in anatase (AI1 and AI2 in Figure 5.9 (a)), both of which are surrounded by oxygen atoms in a distorted octahedral arrangement [113]. In order to investigate the possibility of fitting a Sr ion in

the interstitial site in the anatase structure, we performed a geometric calculation for finding the size of the largest sphere that can fit into the interstitial space in the anatase lattice structure. For this purpose, we considered the case if the Sr ion can be positioned at the larger interstitial site (AI2). The geometric calculations have been restricted to hard-sphere model system of molecules—i.e., idealized molecules that have finite size but no forces involved (Figure 5.9). Based on the Shannon and Prewitt ionic radii, the effective ionic radius of $Ti^{4+}$ and $O^{2-}$ with six-fold coordination in anatase are 0.61 Å and 1.40 Å, respectively [114]. The cell structure around the interstitial site is the same as that around the Ti atoms, except for the distances of the oxygen along the $z$-direction [115]. This distance was calculated to be (0.137 nm) knowing the radius of $O^{-2}$ (0.14 nm), the length of O-Ti-O bond (0.396 nm) in the middle of the cell and the dimension of the cell along the $c$-axis (0.948 nm). The results of these calculations revealed that the largest ion that can fit in the octahedrally coordinated interstitial site is ~ 0.057 nm. This reveals that the 6-fold coordinated with the effective ionic radius of 0.116 nm cannot fit the free space of the anatase. Consequently, the insertion of such a large ion in such a small empty space may enhance the possibility of the local lattice distortions associated with the lattice modulations due to the presence of large dopant.

It has been reported that the photoreactivity of oxide semiconductors, such as $TiO_2$, is closely related to defect disorder [116]. Therefore, their photoreactivity and related performance can be modified by shifting the defect equilibria. Table 5.2 and 5.3 show the Kröger−Vink [117] and traditional notations of defects for $TiO_2$ and $Sr^{2+}$-doped $TiO_2$ and the basic defect equilibria in the $TiO_2$ [108].

**Table 5.3** Kröger−Vink and traditional notation of defects for $TiO_2$ and $Sr^{2+}$-doped $TiO_2$

| traditional notation | description | Kröger−Vink notation |
|---|---|---|
| $Ti_{Ti}^{4+}$ | $Ti_{Ti}^{4+}$ ion in the titanium lattice site | $Ti_{Ti}^{x}$ |
| $Ti_{Ti}^{3+}$ | $Ti_{Ti}^{3+}$ ion in the titanium lattice site | $e'$ |
| $V_{Ti}$ | titanium vacancy | $V_{Ti}''''$ |
| $Ti_i^{3+}$ | $Ti_i^{3+}$ in the interstitial site | $Ti_i^{\bullet\bullet\bullet}$ |
| $Ti_i^{4+}$ | $Ti_i^{4+}$ in the interstitial site | $Ti_i^{\bullet\bullet\bullet\bullet}$ |
| $O_O^{2-}$ | $O_O^{2-}$ ion in the oxygen lattice site | $O_O^{x}$ |
| $V_O$ | oxygen vacancy | $V_O^{\bullet\bullet}$ |
| $O_O^{-}$ | $O_O^{-}$ ion in the oxygen lattice site | $h^{\bullet}$ |
| $Sr_{Ti}^{2+}$ | $Sr_{Ti}^{2+}$ ion in the titanium lattice site | $Sr_{Ti}''$ |
| $Sr_i^{2+}$ | $Sr_i^{2+}$ ion in the interstitial site | $Sr_i^{\bullet\bullet}$ |

**Table 5.4** Basic defect equilibria in $TiO_2$ using Kröger−Vink notation

$$O_O^{x} \Leftrightarrow V_O^{\bullet\bullet} + 2e' + \frac{1}{2}O_2 \qquad (1)$$

$$Ti_{Ti}^{x} + 2O_O^{x} \Leftrightarrow Ti_i^{\bullet\bullet\bullet} + 3e' + O_2 \qquad (2)$$

$$Ti_{Ti}^{x} + 2O_O^{x} \Leftrightarrow Ti_i^{\bullet\bullet\bullet\bullet} + 4e' + O_2 \qquad (3)$$

$$O_2 \Leftrightarrow V_{Ti}'''' + 4h^{\bullet} + 2O_O^{x} \qquad (4)$$

$$nil \Leftrightarrow e' + h^{\bullet} \qquad (5)$$
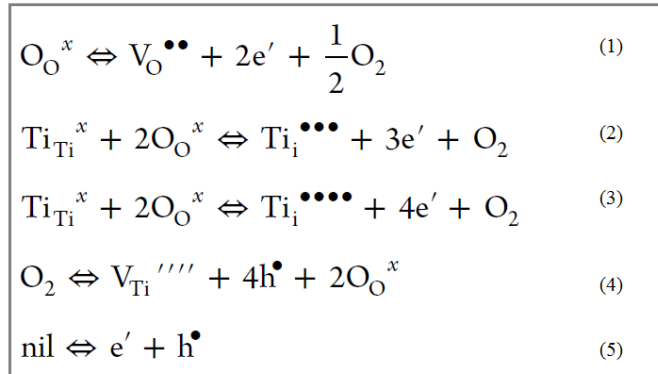
Based on the results obtained from calculation of the interstitial site in the $TiO_2$ lattice and the fact that interstitial Sr is unlikely to happen, the possibility of incorporation of the $Sr^{2+}$ dopant substitution for $Ti^{4+}$ in coordination number six with charge compensating oxygen vacancies can be examined as the following:

$$SrO \overset{TiO_2}{\rightleftarrows} Sr''_{Ti} + O^x_O + V^{\bullet\bullet}_O \tag{5.1}$$

in Kröger−Vink notation.

This defect disorder is governed by ionic charge compensation of strontium:

$$[Sr''_{Ti}] = V^{\bullet\bullet}_O \tag{5.2}$$

Thus, the residence of larger-sized $Sr^{2+}$ in substitutional sites would also cause volume-compensating oxygen vacancies as shown experimentally and theoretically earlier. As such, defect clusters such as $[Sr''_{Ti} - V^{\bullet\bullet}_O]$ could occur along different [hkl] directions in the $TiO_2$ lattice resulting in alteration of the atomic distances [118].

5.2.2.2. Surface Analysis of $Sr^{2+}$-$TiO_2$ Nanotubes: Effect of Dopant on the Surface and Electronic Structure of $TiO_2$

*5.2.2.2.1 XPS Analysis*

In order to investigate the composition, surface properties and chemical states of Ti, O and Sr in terms of the effect of dopant concentration, X-ray photoelectron spectroscopy (XPS) analysis was performed on the as-anodized and annealed nanotube arrays. All peak position numbers reported here are extracted from the XPS data and corresponding fitted components with details of fitted peaks given in Appendix B. For more clarity on the general trends due to the presence of the Sr dopant, the fitted peaks are not combined with the overall XPS spectra in this chapter.

Before performing the XPS measurements on the surfaces of the nanotube samples, the XPS depth profile analysis was performed to obtain information about the lateral elemental distribution along the length of the nanotubes in doped samples. Figure 5.10 shows a typical depth profile result of the $Sr^{2+}$-doped $TiO_2$ nanotubes displayed in a 2D colored map which was performed along the vertical axis of the nanotube arrays. The etching rate of the instrument was calibrated using a $Ta_2O_5$ standard (0.19 nm/sec for the $Ar^+$ ion energy of 2000 eV). Based on the relative sputtering rates reported for the $Ta_2O_5$ and $TiO_2$ using the same ion energy in Ref. [119], the sputter rate of $TiO_2$ was estimated to be ~ 0.14 nm/sec. The depth profiling was carried out on a spot size of 400 µm and every scan was performed after each etching cycle of 3 min on the sample. A total of 9 cycles were performed which resulted in etching of about 324 nm of the material (~1.3 of the tube length) along the nanotubes. The O 1$s$, Ti 2$p$ and Sr 3$d$ scans were recorded on the sample after each cycle. Based on the etching rate, the depth of each cycle was estimated to about 25 nm.

The results of depth profiling are shown in Figure 5.10. As shown, a shift is observed from the first scan to the next scans after etching the first layer which is related to an actual difference between the charge conditions of the top layer, i.e., the unsputtered layer of a sample and the subsurface sputtered layers. This shift is caused from a new charge equilibrium occurring as the sputter gun ions interact with the surface.

Figure 5.10 (a) shows the O 1$s$ map with a homogeneous distribution of lattice oxygen along the nanotubes. The stacked depth profile plot of the O 1$s$ photoemission spectra is shown in Figure 5.10 (d). A comparison between the O 1$s$ peak of the first and the last scans revealed the presence of a broadened peak in that last scan. A careful peak

fitting analysis of this broadened peak (as shown in Appendix B) revealed the Sr-O contribution at 532.3 eV in a small portion to the O 1s peak in addition to two other peaks occurring at 531.4 eV and 530.4 eV which can be attributed to the Ti-O contribution with O and Ti at different chemical states (from the nonstoichiometry that is induced in the $TiO_2$ structure by the presence of dopant). It should be noted that the attribution of the shoulder peak at higher binding energy (~ 532 eV) to chemisorbed oxygen is not valid, because the etching procedure is performed in the vacuum chamber and there is low chance for the bombarded oxygen atoms making new bonds with on the surface.

Figure 5.10 (b) shows the Ti $2p$ map with a fairly noticeable change in the distribution of Ti $2p$ core level photoemissions with respect to the binding energies and the geometry of the nanotubes which reveals variation of the oxidation states of Ti from the surface along the nanotubes. This can be well explained based on the stacked depth profile Ti $2p$ photoemission spectra shown in Figure 5.10 (e). It can be seen from this spectra (and from the deconvoluted peaks given in the Appendix B) that as we move from the surface toward the bulk of the nanotubes, the pair peaks of $Ti^{4+}$ start to shrink and shoulder pair peaks associated with $Ti^{3+}$ and $Ti^{2+}$ start to develop at 457.5 eV and 455 eV that correspond to the partial reduction of $Ti^{4+}$ to $Ti^{3+}$ and $Ti^{2+}$ states, respectively. It should be mentioned that the depth profiling XPS experiment has been carried out in a separate analysis chamber after annealing of the doped nanotubes; thus, the surfaces of the nanotubes were further oxidized upon exposure to air during the transport from the growth chamber to the analytical setup which may result in re-oxidation of $Ti^{3+}$ and $Ti^{2+}$ back to $Ti^{4+}$ on the very top surface. Despite this surface oxidation, the reduction in titanium along the nanotubes is still observed.
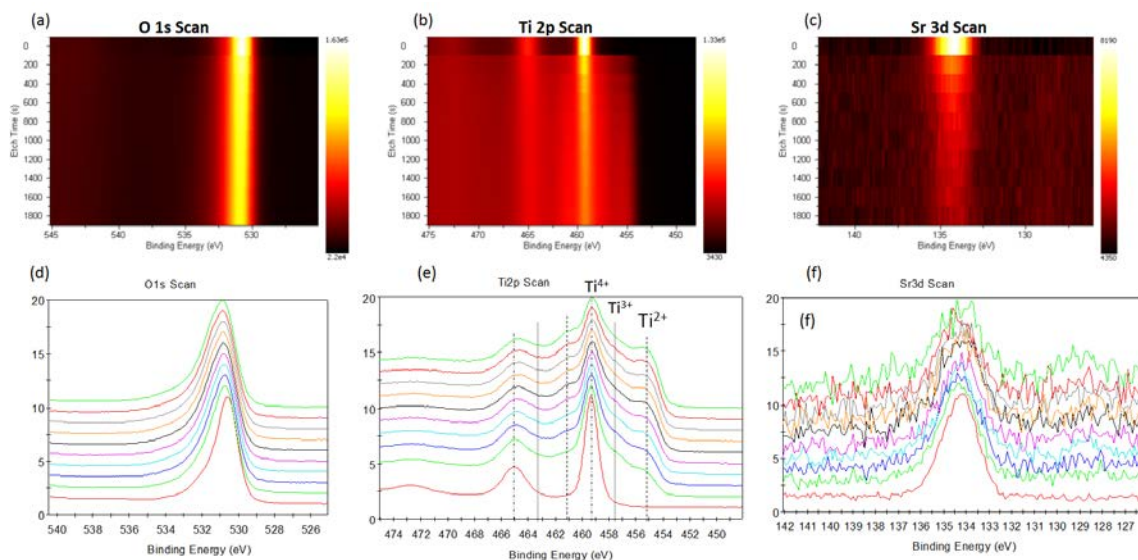
**Figure 5.10** XPS depth-profile elemental maps of (a, d) O 1*s*, (b, e) Ti 2*p* and (c, f) Sr 3*d* showing the lateral elemental distribution along the nanotube length.

Figure 5.11 shows the XPS results as a function of dopant concentration for as-anodized $Sr^{2+}$-doped $TiO_2$ in an electrolyte with pH = 2. The Sr 3*d* core level XPS spectrum is shown in Figure 5.11 (a) which confirms the presence of strontium in all doped samples while the peak intensities of the Sr 3*d* are shown to increase with increasing the Sr dopant concentration. The main peak positioned at 133.7 eV is attributed to Sr $3d_{3/2}$ and the shoulder peak positioned at 135.5 eV corresponds to Sr $3d_{5/2}$.

Figure 5.11 (b) shows O 1s photoemission spectra at 530.2 eV for un-doped $TiO_2$ nanotube sample which is assigned to lattice oxygen in anatase $TiO_2$ (Ti-O bond). By adding the strontium dopant atom to the compound and as the concentration is increased, a shoulder peak at the higher binding energies side of O 1*s* starts to develop and grow to

higher intensities in the sample with the highest dopant content. This shoulder peak position in the highest doping content sample corresponds to the binding energy of 531.7 eV which is attributed to the undercoordinated $TiO_{0.9}$ and is indication of formation of oxygen deficient $TiO_2$ due to addition of lower valence $Sr^{2+}$. The other peak could be attributed to surface bridging O atoms and hydroxyl O atoms. Also, as the dopant content is increased, the Ti peaks shifts to higher binding energies. Generally, chemical shift in XPS peaks is related to the change in binding energy of a core electron (electrostatic interaction between core electron and the nucleus) of an element due to a change in the chemical bonding of that element. This binding energy (BE) is influenced by changes in the electrostatic shielding of the nuclear charge from all other electrons in the atom (including valence electrons) due to removal or addition of electronic charge as a result of changes in bonding. Thus, the shift in O and Ti peaks in all doped nanotube samples compared to undoped $TiO_2$ can be explained in the presence of $Sr^{2+}$ in the $TiO_2$ lattice and as a result the relocation of electron density from the $Ti^{4+}$ and $O^{2-}$ in its surroundings. This result in the oxygen become more ionic and the Ti become more cationic. The Ti $2p$ spectra with two peaks were obtained for all samples as shown in Figure 5.11 (c). These peaks correspond to Ti $2p_{1/2}$ and Ti $2p_{3/2}$ photoemission spectra occurring at 464.6 eV and 458.9 eV for undoped $TiO_2$ nanotubes sample respectively, and with a spin orbit splitting of 5.7 eV in all samples. The shift toward higher binding energies in Ti spectra can be explained similarly to that of oxygen. Note that sample ST2 with intermediate dopant content is slightly off-trend from others in terms of peak position. Considerable change in the peak intensities of Ti as a function of dopant concentration is also observed. This

could be related to presence of metallic Sr or SrO on the surface which causes the photoemission from Ti to be hindered.

Surface properties of the annealed (crystalline) $Sr^{2+}$-doped $TiO_2$ samples are shown in Figure 5.12. A similar trend as discussed above was observed in the peak intensities in terms of the dopant concentration in Sr $3d$ core level XPS spectrum as shown in Figure 5.12 (a). However, there is no sign of metallic Sr accompanied by the fact that all peaks in Sr spectra have shifted toward higher binding energies confirming the presence of more cationic $Sr^{2+}$ in the form of oxide in all doped samples. Also, a shoulder peak at higher binding energy side of the main peak in Sr spectrum started to form and grow as the dopant content is increased which is related to the oxygen bonded to Sr. The peaks in Figure 5.12 (c) correspond to Ti $2p_{1/2}$ and Ti $2p_{3/2}$ photoemission spectra occurring at 465.1 eV and 459.4 eV for undoped $TiO_2$ nanotubes sample respectively, and with a spin orbit splitting of 5.7 eV in all samples which confirms that both signals correspond to $Ti^{4+}$ and the titanium oxidation state have remained unchanged by the doping at different levels. The change in the peak intensities of both O and Ti as a function of dopant concentration in Figure 5.12 (b) and (c) is insignificant. Interestingly, the change in peak intensities and the peak shifts as a function of dopant concentration in both Ti and O photoemission spectra are precisely matched. Based on quantitative elemental analysis from XPS data, the chemical stoichiometry of the $TiO_2$ was obtained.
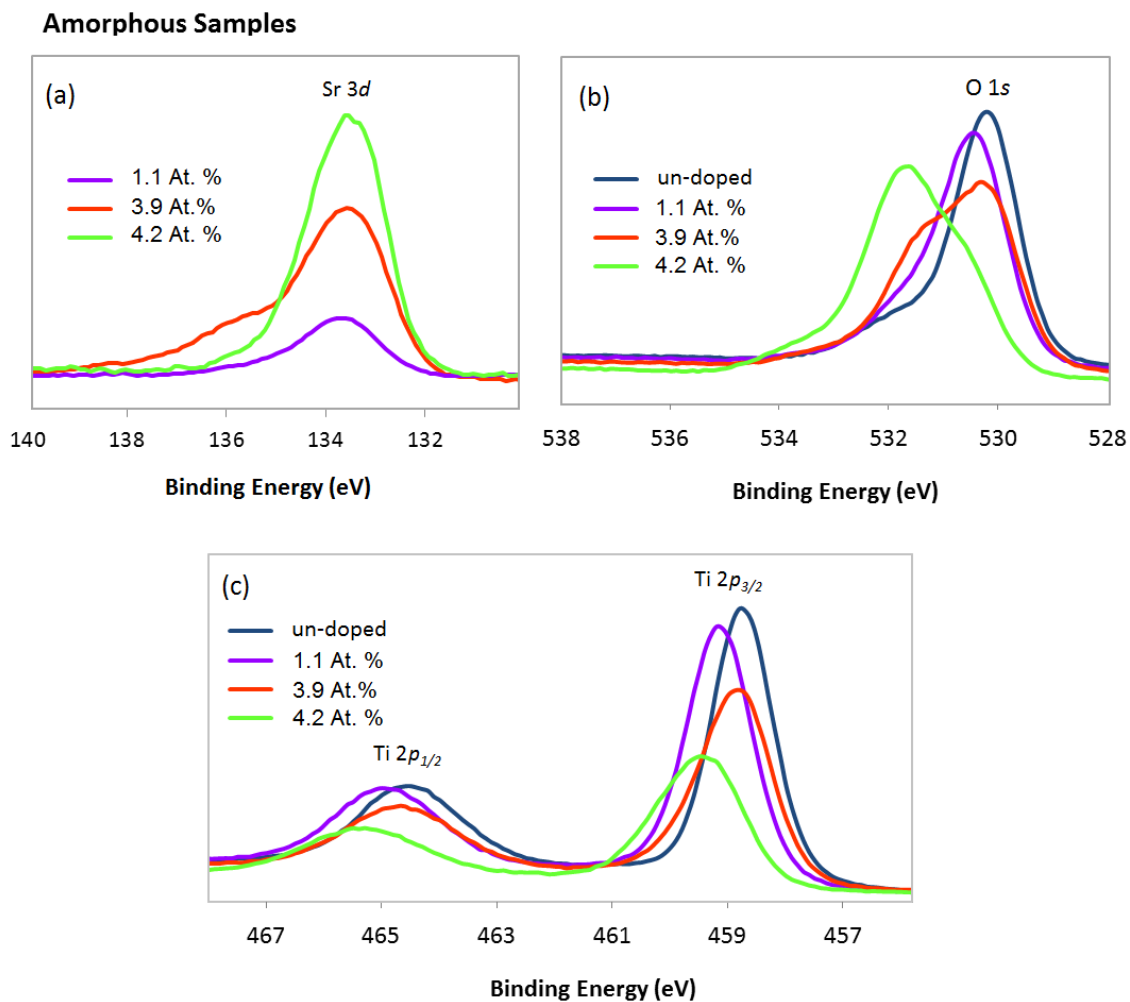
**Figure 5.11** XPS spectra for as-anodized (amorphous) $Sr^{2+}$-$TiO_2$ nanotube samples showing (a) Ti $2p$, (b) O $1s$ and (c) Sr $3d$ as a function of Sr-dopant concentration in electrolyte pH = 2.
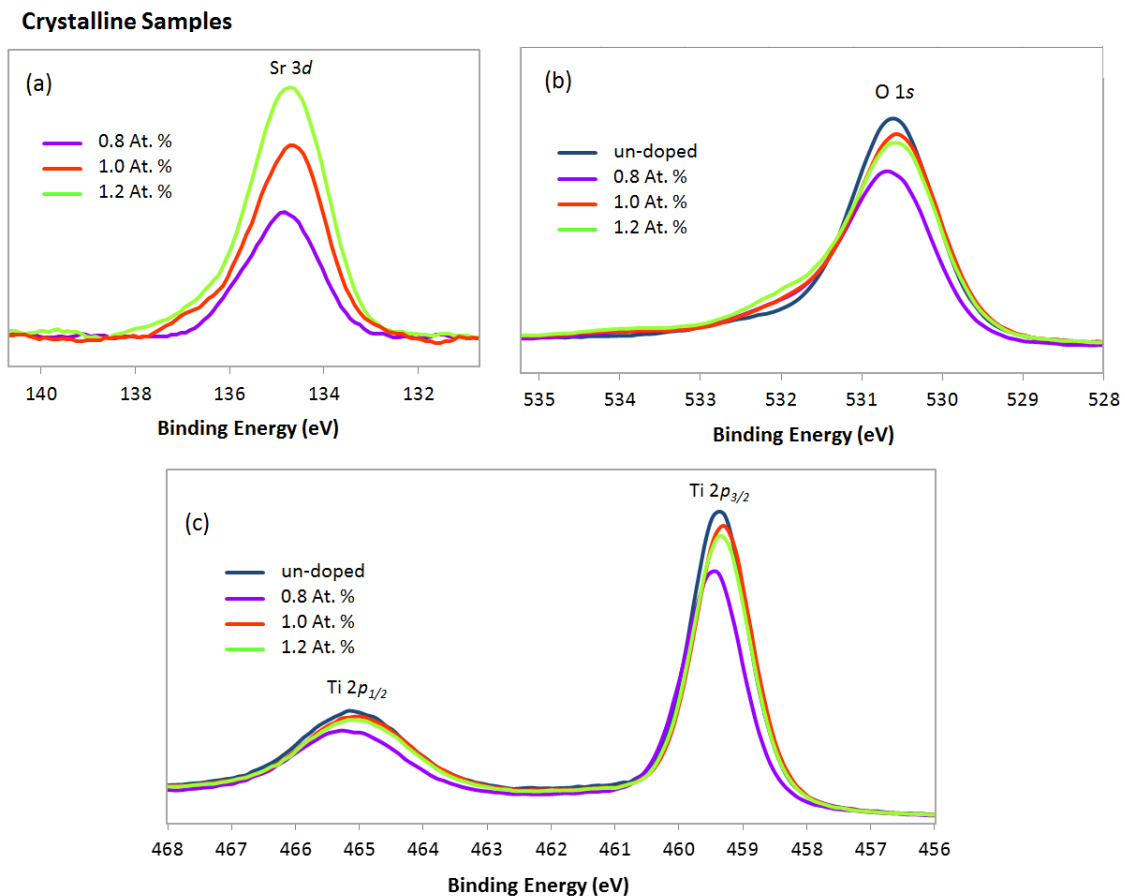
**Figure 5.12** XPS spectra for annealed (crystalline) $Sr^{2+}$-$TiO_2$ nanotube samples showing (a) Ti $2p$, (b) O $1s$ and (c) Sr $3d$ as a function of Sr-dopant concentration in electrolyte pH = 2.

It is known that withdrawal of valence electron charge increase in BE (oxidation) and addition of valence electron charge decrease in BE (reduction). Comparing the XPS data in amorphous (as-anodized) and crystalline (annealed) undoped and $Sr^{2+}$-doped $TiO_2$ nanotube samples in Figure 5.11 and Figure 5.12 confirm formation of metal oxides ($TiO_2$) as a result of annealing process.

*5.2.2.2.2 NEXAFS Analysis*

In order to probe local changes in electronic structure and chemical bonding of the Ti and O atoms in the doped $TiO_2$ nanotubes in the presence of the Sr dopant, the near edge X-ray absorption fine structure (NEXAFS) soft X-ray absorption spectra is used, due to its high sensitivity to the bonding environment of the absorbing atom. NEXAFS is an element specific technique which encompasses the part of X-ray absorption spectrum where the energy of the incident X-ray, $E$, is about the first 30 eV above the actual absorption edge [120] (Figure 5.13). In this region, the ejected photoelectrons with low kinetic energy (large wavelength) experience multiple backscattering events, not only from the atoms constituting the first shell around the absorbing atom, but also from the further shells at the nearest neighbors. These multiple scattering events create modulation features in the NEXAFS region that are very sensitive markers of the local electronic and geometric structure [21].

NEXAFS is also an ideal technique for investigation of the electronic states of $TiO_2$-based materials. NEXAFS spectra are clear fingerprints of titanium oxides which show significant differences in the structure due to a change of the crystallographic phase as well as to Ti reduction [121]. Due to high sensitivity of the O K-edge and Ti L-edge peaks to the local bonding environment, this technique can provide diagnostic information about the crystal structures and oxidation states of various forms of doped and undoped titanium oxide compounds [122]. In addition, the directional electric field vector ($\bar{E}$) of the X-rays can be used to probe the direction of chemical bonds of the atoms.

86
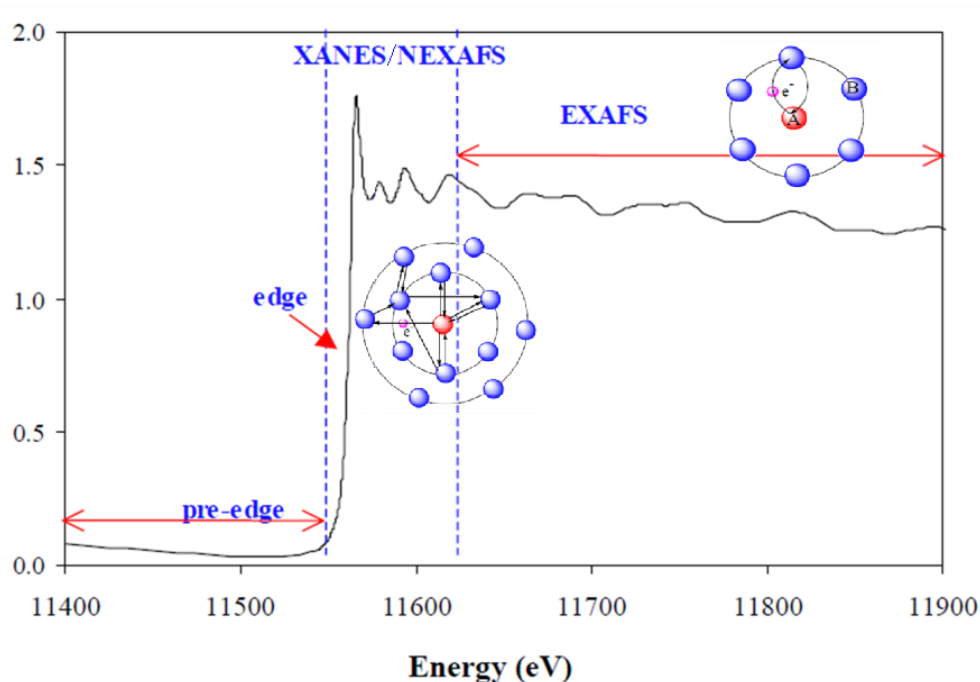
**Figure 5.13** An X-ray absorption spectrum, showing four different regions. Single scattering of ejected photoelectron with high kinetic energy creates the EXAFS features whereas NEXAFS features are formed due to multiple scattering of low kinetic energy photoelectron [21].

Before we proceed to the analysis of the results, it is useful to note that the Ti $L_{3,2}$-edge NEXAFS results from transitions from $2p_{3/2}$ and $2p_{1/2}$ to the final state of Ti $3d_{5/2,3/2}$ character in transition metals due to small spin– orbit coupling in the $2p$ shell of $3d$ and crystal field when the Ti ion forms a compound. Single-crystalline $TiO_2$ spectra show well resolved peaks in the range between 455 and 470 eV which correspond to the transitions from the Ti $2p$ core level to the unoccupied Ti $3d$ state. The Ti L -edge shows two groups of peaks arising from the spin-orbit splitting of Ti $2p$ core level into $2p_{3/2}$ and $2p_{1/2}$ levels (namely, $L_2$ and $L_3$) with ~ 6 eV energy separation. These levels are further

split due to crystal-field effects [121, 122]. The splitting within each edge into multiple peaks is due to spin orbital and crystal effects. For example, the relative intensities of the $L_3$-edge doublets $a_1$ and $a_2$ (similar for $L_2$-edge) and their energy separation are related to the strength of the crystal field. In general, the larger the crystal field, the more intense the $a_1$ peak relative to $a_2$, the larger the separation [123]. In $TiO_2$, the second peak of the $L_3$ resonance further splits $a_2$ into $a_{2'}$ and $a_{2''}$. In addition, the relative intensities of the $a_{2'}$ is larger than that of $a_{2''}$ in anatase and is smaller in rutile (Figure 5.14 (a)).
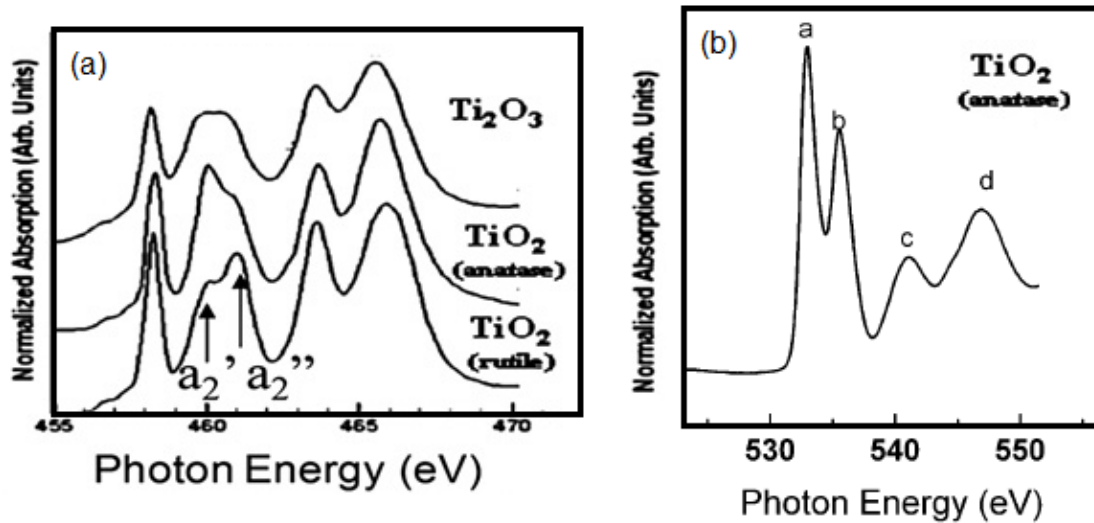


**Figure 5.14** (a) Ti $L_{3,2}$-edge NEXAFS of annealed $Ti_2O_3$, anatase and rutile structures, (b) O K-edge NEXAFS of anatase [123].

On the other hand, the O K-edge probes the O $2p$ projected unoccupied density of states in the conduction band. Due to hybridization between O $2p$ and Ti $3d$ or Ti $4sp$. transitions into the O $2p$–Ti $3d$ hybridized bands which split into peaks a and b because of the crystal field, and transitions into O $2p$–Ti $4sp$ hybridized bands (peaks c and d) as shown in Figure 5.14 (b).

In this work, NEXAFS with sampling depth of a few nanometers was performed on the surface of the annealed doped and undoped $TiO_2$ nanotubes by acquiring peak intensities as a function of the incident X-ray photon energy in the vicinity of the titanium L-edge (445−490 eV) and the oxygen K-edge (520−590 eV) regions. The data here are shown as normalized intensities versus photon energy of the incident beam. In order to probe the Ti-O bond directionality, the NEXAFS data were collected varying the angle between the electric field vector of the x-rays and the surface of the nanotubes arrays with the photon beam fixed at parallel, in 55° and perpendicular to the surface normal of the sample. Due to natural polarization of the Synchrotron radiation, NEXAFS has great capability for identifying particular orientation on a surface. Thus, such angle dependence of the X-ray absorption can be used to probe the orientation of resonant bonds due to dipole selection rules. The structure of anatase is conceivable as a close packing of large oxygen atoms with titanium atoms in every second octahedral interstitial site in a zigzag alignment as shown earlier. Every titanium atom is thus surrounded by an oxygen octahedron. The atoms have a pronounced ionic character, resulting in a strong crystal field that distorts the octahedral symmetry.

The formation of $TiO_6$ octahedra is confirmed by analyzing the characteristic spectral line shapes of the Ti L-edge features. Figure 5.15 shows the magic angle (55°) NEXAFS spectra of the titanium 2$p$ ($L_{2,3}$-edge) and oxygen 1$s$ (K-edge) for annealed (crystalline) $TiO_2$ and $Sr^{2+}$-doped $TiO_2$ nanotube samples with three different dopant concentrations. (For doping contents in the samples refer to XPS measured values for annealed samples in Table 5.1). At this angle, there is no orientation preference. These spectra represent the orbital character of the spectral features of the O 1$s$ and Ti 2$p$

unoccupied states in the conduction band and its hybridization with different orbitals such as Sr in the doped system.

From Figure 5.15 (a), we observe that the Ti $L_{3,2}$-edge NEXAFS of annealed $Sr^{2+}$-doped $TiO_2$ and $TiO_2$ nanotube samples exhibits an intensity pattern $a_{2'} > a_{2''}$ which is similar to that of anatase. Likewise the XRD data from the bulk of the nanotubes, this result confirms that no phase change has been also occurred on the surface of $Sr^{2+}$-doped $TiO_2$ nanotubes after annealing. Also, the Ti L-edge with two doublet peaks is observed between 455 and 470 eV. In the $TiO_2$ anatase structure, the Ti $2p$ spin−orbit interaction splits into the $L_3$ ($2p_{3/2}$) and $L_2$ ($2p_{1/2}$) levels with a separation of 5.5 eV. The $L_2$ and $L_3$ adsorption edges are further split into two doublet peaks of $t_{2g}$ and $e_g$ as sub-bands which is due to the crystal field effect. It was found that the shape of the L and K absorption spectra in all data taken here is typical for titanium and oxygen of $TiO_2$ in the anatase structure as reported in the literature with slight variations in the intensity and splitting in the spectra of the doped samples compared to undoped $TiO_2$ nanotube that can be related to the presence of strontium. In fact, along with the insertion of $Sr^{2+}$ ion into the interstitial sites in anatase $TiO_2$ nanotubes, electrons are doped into the lattice by filling the empty conduction bands for the charge compensation due to presence of $Sr^{2+}$. Hence, such modification is expected to be reflected in the electronic structure of the anatase $TiO_2$, in the Ti $L_{3,2}$-edge and O K-edge spectra as shown in Figure 5.15.

As can be seen, the relative intensity of the main peaks and the crystal field splitting to the $t_{2g}$ and $e_g$ orbitals of ~1.8 eV in Ti L-edge and 2.5 eV in O K-edge spectra in all samples strongly matches the known spectra for the anatase phase and confirms that the oxidation states of $Ti^{4+}$ has remained unchanged which is strongly in agreement with

the XPS data. Generally, owing to the localization of charge in Ti $3d$ orbitals in $Ti^{3+}$, a shift the absorption peaks to lower photon energy is usually observed [123].

A change in intensity of $t_{2g}$ and $e_g$ peaks with respect to dopant concentration is clearly seen. This change reveals whether or not the dopant atom is pulling the electrons away from Ti atom. As shown in Figure 5.15 (a), the sample with highest dopant content shows the highest intensity which is indicative of electrons leaving the Ti $3d$ orbitals due to presence of neighboring Sr. Also, the relative intensities of the doublet in $L_3$- $e_g$ which is normally higher for the lower energy peak to the higher energy one in the anatase is the same for all doped samples.

A close inspection of the O K-edge spectra reveals slight changes in the intensity as well as the $t_{2g}$- $e_g$ splitting as shown in Figure 5.15 (b) with respect to doping. The decrease in intensities of the doped samples is an evidence of a reduction in O $2p$–Ti $3d$ bands, which is consistent with the higher intensity of the corresponding XANES at the Ti L-edge in doped samples compared to the undoped $TiO_2$ as shown in Figure 5.15 (a)). In fact, this further implies charge relocation from Ti $3d$ to O $2p$ which results in Ti–O bonds become more ionic. On the other hand, the magnitude of this splitting depends on the strength of the field created by the point charges which is in turn affected by the point charges distance from the central atom and from the overall magnitude of each charge. The observed decrease in the magnitude of splitting relative to the amount of dopant indicates that the presence of dopant Sr may cause the O atoms occupy sites at different distance from the Ti as the center atom in the octahedra and therefore create different degrees of distortion and/or different stacking of the octrahedra units from what is observed from the symmetry in undoped $TiO_2$. This effect may strengthen the hypothesis

of the Sr atom occupying the interstitial sites on the surface of the nanotubes; since the distance between the Sr and O atoms is less in this case than the Sr to Ti atoms, the O orbitals are more likely to be affected by adjacent dopant atom. In summary, it can be concluded that $Sr^{2+}$ doping only alters the Ti and O ions interaction in the $TiO_2$ lattice on the surface and has no evident effect on their individual charge states.
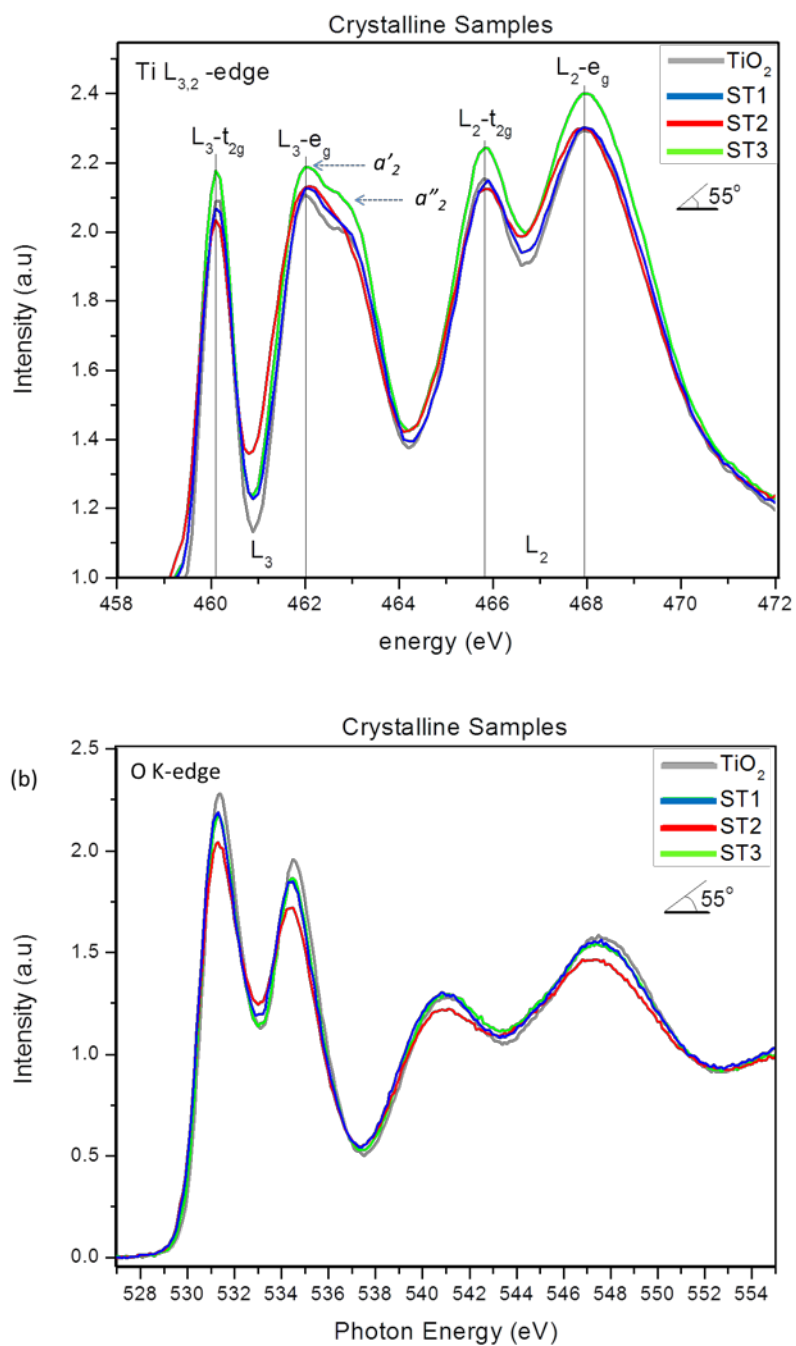
**Figure 5.15** NEXAFS spectra of (a) titanium $2p$ ($L_{2,3}$-edge) and (b) oxygen $1s$ (K-edge) for annealed (crystalline) $TiO_2$ and $Sr^{2+}$-doped $TiO_2$ nanotube samples with three different dopant concentrations taken at magic angle.

The NEXAFS data were also measured at different incident beam angles on ST3 sample which is the $Sr^{2+}$-doped $TiO_2$ nanotube sample with the highest doping level. Figure 5.16 illustrates the schematic of the relation between the X-ray incident beam and the X-ray electric field vector ($\bar{E}$) with respect to the nanotubes orientation in the sample used for NEXAFS experiment. As shown, the data were collected varying the angle between the electric field vector of the x-rays and the surface of the nanotubes arrays with the photon beam fixed at parallel, in 55° and perpendicular to the surface normal of the sample.

Figure 5.17 illustrates the NEXAFS spectra of titanium $2p$ ($L_{2,3}$-edge) and oxygen $1s$ (K-edge) recorded on the $Sr^{+2}$-doped $TiO_2$ nanotubes with the highest dopant content (sample ST3) in three different experimental geometries where the incident beam is parallel, in 55° and perpendicular to the principal axis of the nanotube arrays. As can be seen in Figure 5.17 (a), the Ti L-edge spectra for ST3 sample are similar to those reported earlier for the $TiO_2$ anatase phase in terms of the shape of the peaks and the crystal field splitting, but with the main discrepancy in the intensities with respect to the $\bar{E}$ direction. Starting by the normal incidence, which has the highest intensity in the Ti L-edge spectra of Figure 5.17 (a), the $\bar{E}$ vector which is normal to the incident beam has also the largest projection in the direction normal to the tube wall. Therefore, the higher intensity of the peaks in this direction implies the existence of a preferential orientation of the crystals in a specific direction where $\bar{E}$ vector is highly involved in the promotion of the electrons from occupied to unoccupied orbitals. The texture analysis of the ST3 nanotube sample (repeated on two ST3 samples) revealed preferential orientation of the (004) planes

almost parallel to the vertical axis of the nanotubes as shown in Figure 5.18. As shown in this figure, the highest intensity if associated with (004) plane compared to (101) and (200) planes. Thus, based on the observations from NEXAFS data at normal incidence on the surface and the crystal orientation in the bulk, useful information about preferred alignment of the octahedral units with respect to crystal lattice is be obtained which can be further correlated to the orientation of the crystals on the surface to their orientation in the bulk of the nanotubes.

At magic angle of 55°, where the orientation effect is minimal, the intensity of the peak is decreased because the effect from different crystals with different orientations is canceled out. At grazing incidence where the incident beam is parallel to the surface of the nanotubes (which means also normal to the nanotube walls), the $\bar{E}$ has the larger projection along the tube axis. Therefore, the crystal orientation along the tube wall is mostly inspected in this case. The lowest intensity observed at this incident angle reveals that only part of the orbitals contribute to intensity which is consistence with the preferred orientation of the octahedral planes in the *x-y* plane.
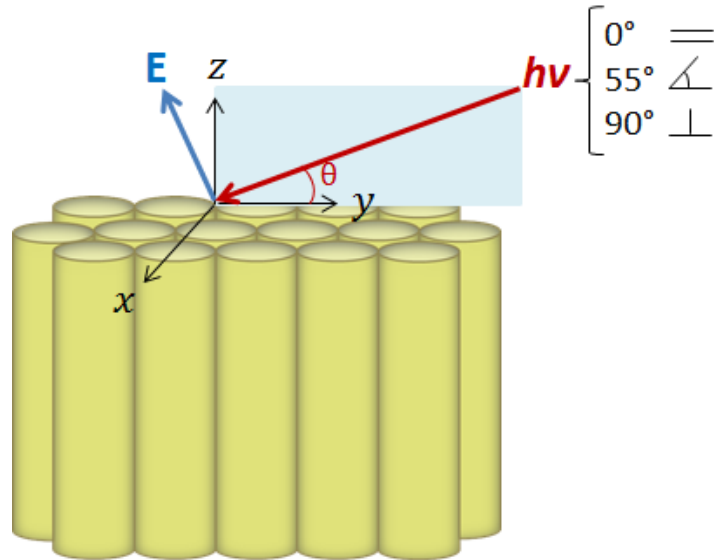
**Figure 5.16** Schematic of the relation between X-ray incident beam and the X-ray electric field vector (Ē) with respect to the nanotubes orientation in the sample used for NEXAFS experiment.

As seen in Figure 5.17 (b), the O K-edge spectra for ST3 sample are observed to be also similar to those reported earlier for the $TiO_2$ anatase phase in terms of the shape of the peaks and the crystal field splitting, however, we do not observe as much of variation in terms of orientation dependency for the oxygen by varying the incidence beam direction from grazing angle toward the normal direction in this spectra. This could be attributed to the fact that most of the information in the O K-edge spectrum is coming from the amorphous layer at the outer layer and on the surface rather than the oxygen in $TiO_2$ lattice structure.
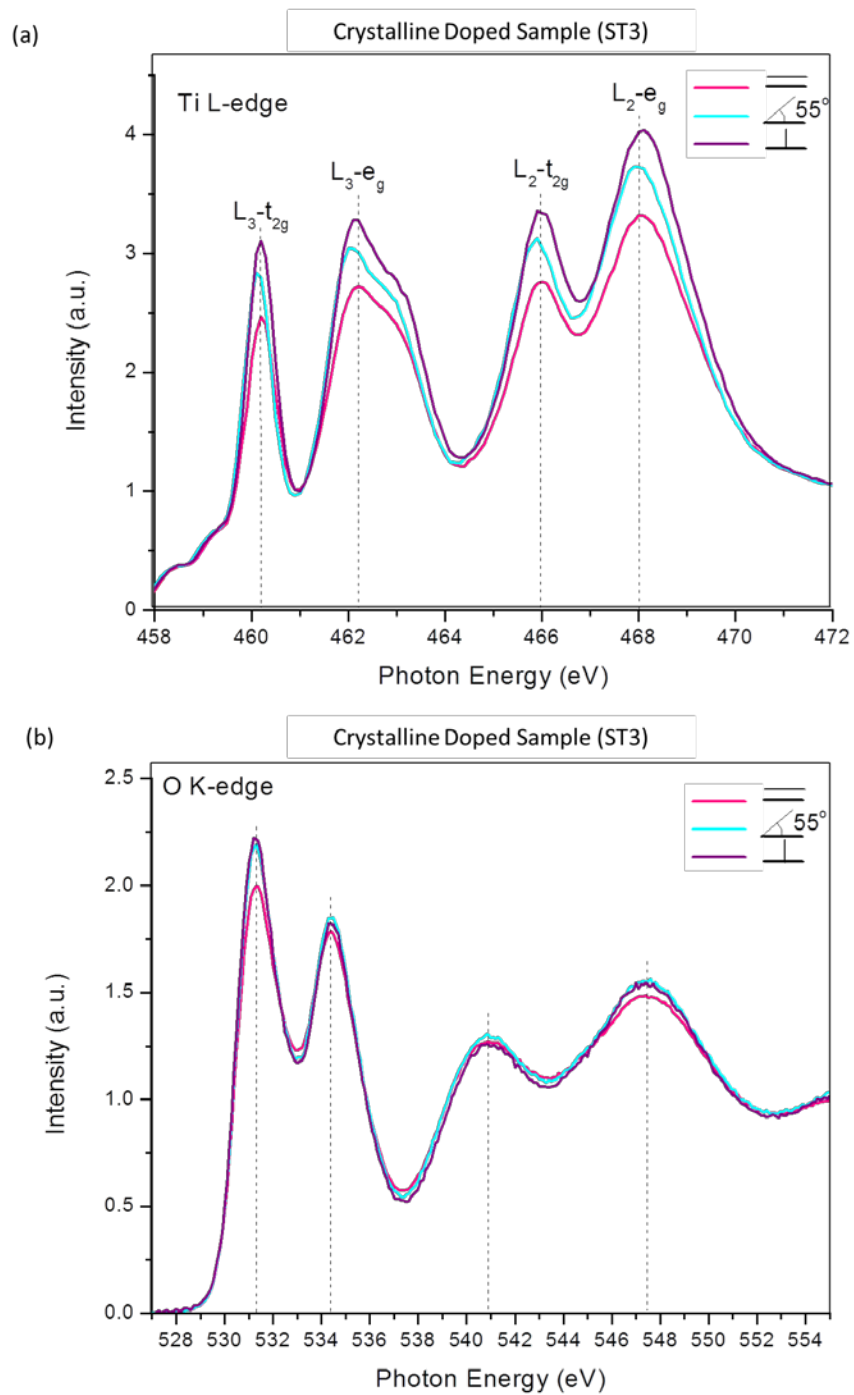
**Figure 5.17** NEXAFS spectra of (a) titanium 2*p* (L$_{2,3}$-edge) and (b) oxygen 1*s* (K-edge) recorded on the Sr$^{+2}$-doped TiO$_2$ nanotubes (sample ST3) in three experimental geometries: Ē parallel, in 55° and perpendicular to the principal axis of the nanostructure.
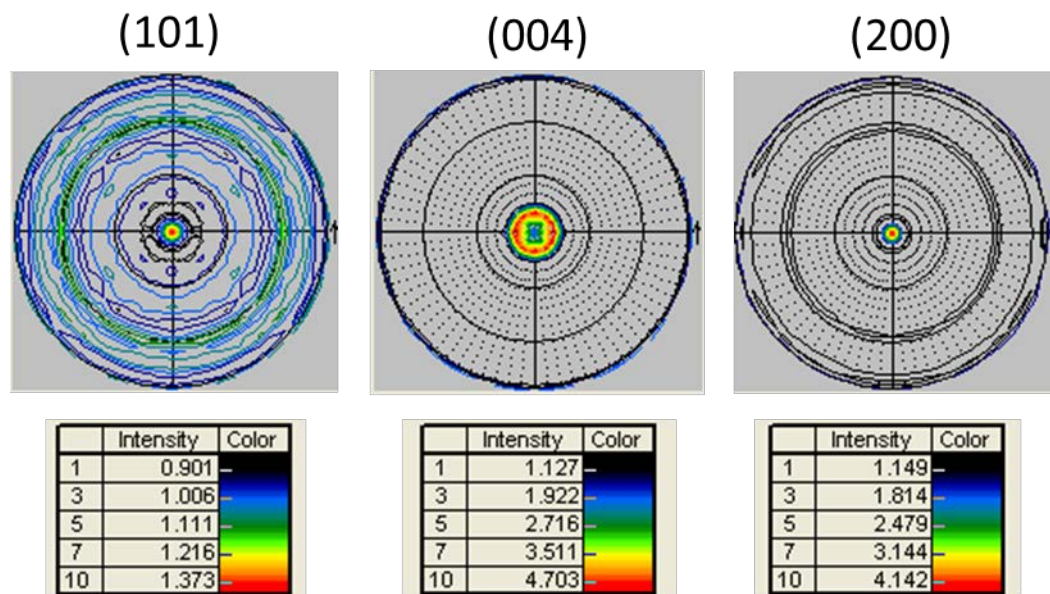
**Figure 5.18** XRD pole-figures of (101), (004) and (200) planes measured at fixed $2\theta$ angles of 25.38°, 38.5° and 48° on ST3 sample.

*5.2.2.2.3 HRTEM, EELS and STEM Analysis*

A clearer insight to understanding more details about the mechanism of doping at the atomic scale is obtained from HRTEM and Z-contrast ADF-STEM imaging combined with EELS spectra acquisition of the surface of the $Sr^{2+}$-doped $TiO_2$ nanotube (sample ST3) in STEM mode. As mentioned previously, the structure of nanotubes is composed of arrangement of several rings along the length. Figure 5.19 (a) shows the Z-contrast ADF-STEM image of a single nanotube probed from the top surface. This image is deliberately taken on a coarser length scale to observe the presence of any distributed clusters. The $Sr-M_{4,5}$, $Ti-L_{2,3}$ and O-K edges are used to extract the EELS SI mapping data with the details of background subtraction in Sr M-edge spectra provided in Appendix C. Generally, the contrast in Z-contrast STEM images is the directly related to

the atomic number. A significant contrast change in Z-contrast images was observed between some regions on the surface of the ring. This means the brighter regions are composed of heavier elements than Ti in the anatase structure. The method of G.A. Botton [124] has been used here to extract the Sr M-edge map which matches well with the Sr position edge and has become more pronounced after removing plural scattering (see Appendix C for more details). The Sr M map also matches well with the bright contrast in the SI survey image. As can be seen from Figure 5.19 (a), the brighter area is indicative of the Sr-rich region and reveals relatively non-uniform distribution of Sr on the surface. From the EELS-SI map of oxygen, titanium and strontium, it appears that the O and Ti are uniformly distributed on the surface whereas the Sr is mostly segregated at the inner edge of the tube. This is clearly observable from the Z-contrast image taken at higher magnification on the ring as shown in Figure 5.20. As can be seen from the STEM SI maps, the bulk region of the ring is composed of a homogeneous distribution of Ti and O; however, a nanometersize cluster of Sr-rich region is formed at the most interior boundary of the nanotube surrounded by Ti and O containing medium.
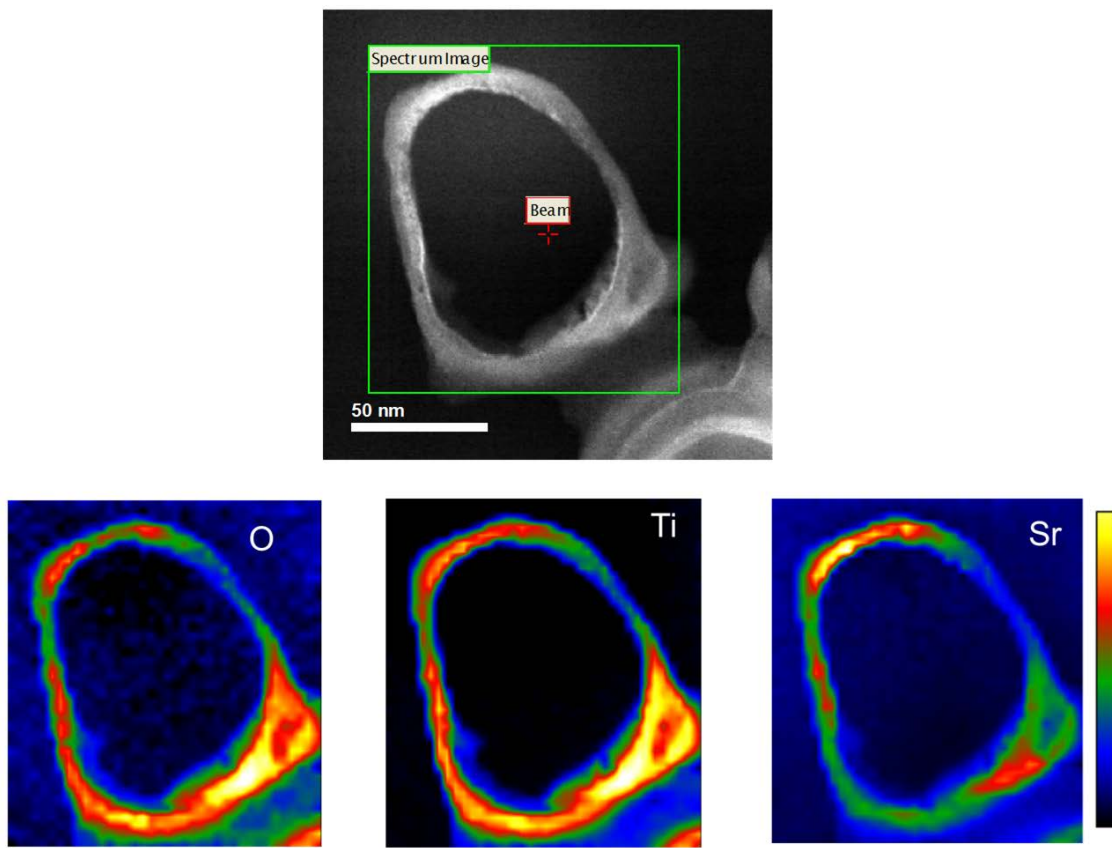
**Figure 5.19** Top: Z-contrast STEM image of the surface of a single $Sr^{2+}$-doped $TiO_2$ nanotube; bottom: the corresponding EELS-SI map of oxygen, titanium and strontium.
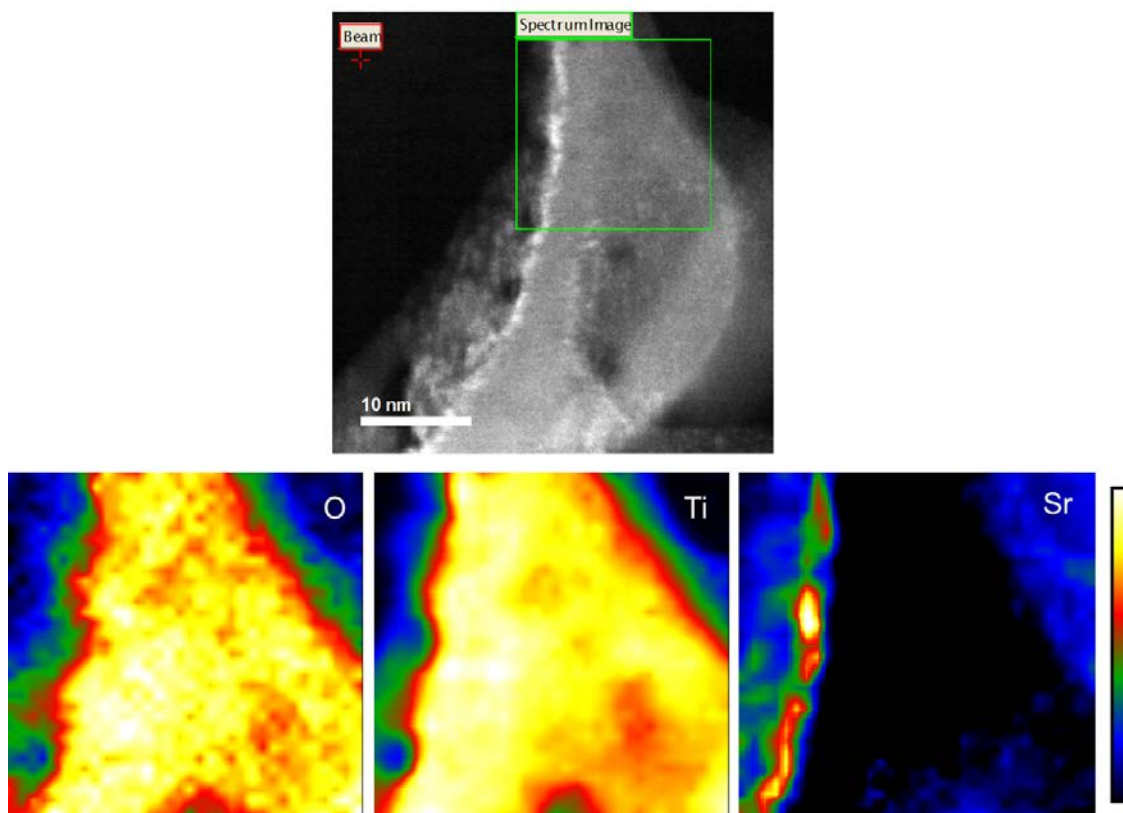
**Figure 5.20** Top: higher magnification Z-contrast STEM image of the surface of a single Sr$^{2+}$-doped TiO$_2$ nanotube; bottom: the corresponding EELS-SI map of oxygen, titanium and strontium.
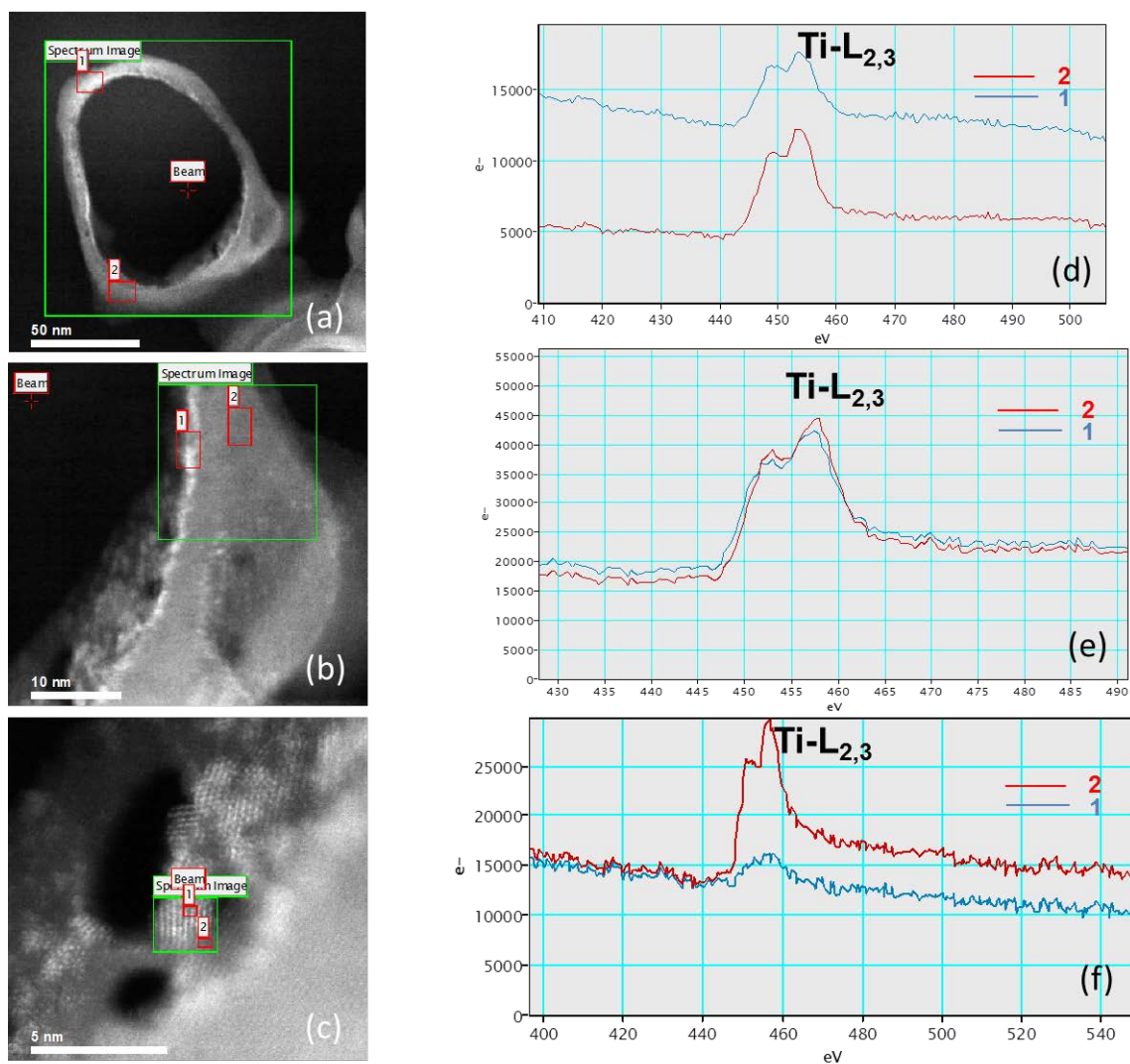
**Figure 5.21** (a-c) Top view Z-contrast STEM image of the surface of a single $Sr^{2+}$-doped $TiO_2$ nanotube at different magnifications; (d-f) the corresponding Ti L-edge EELS spectra taken from two spots in the selected region on the STEM image on the ring.

Comparisons of $Ti$-$L_{2,3}$ signals from different regions on the surface of the doped nanotube is shown in Figure 5.21. As shown, the signal intensity of $Ti$-$L_{2,3}$ varies between the scans over Ti-rich regions in the middle and the Sr-rich region at the edges

on the ring. A significant change is observed for scans over the magnified Sr-rich region as shown in Figure 5.21 (c) and (f). In certain cases, the segregation-induced enrichment of the surface layer results in the formation of low-dimensional surface structures. This is the case when the local concentrations surpass certain critical limits [108]. This result reveals that in the highest doped nanotube sample, as we move toward the interior edge of the nanotube, the Sr-rich region segregates into nanoclusters of a completely new phase forming heteronanostructures (HNSs) that gradually merges into the $TiO_2$ lattice in intimate vicinity of the interface.
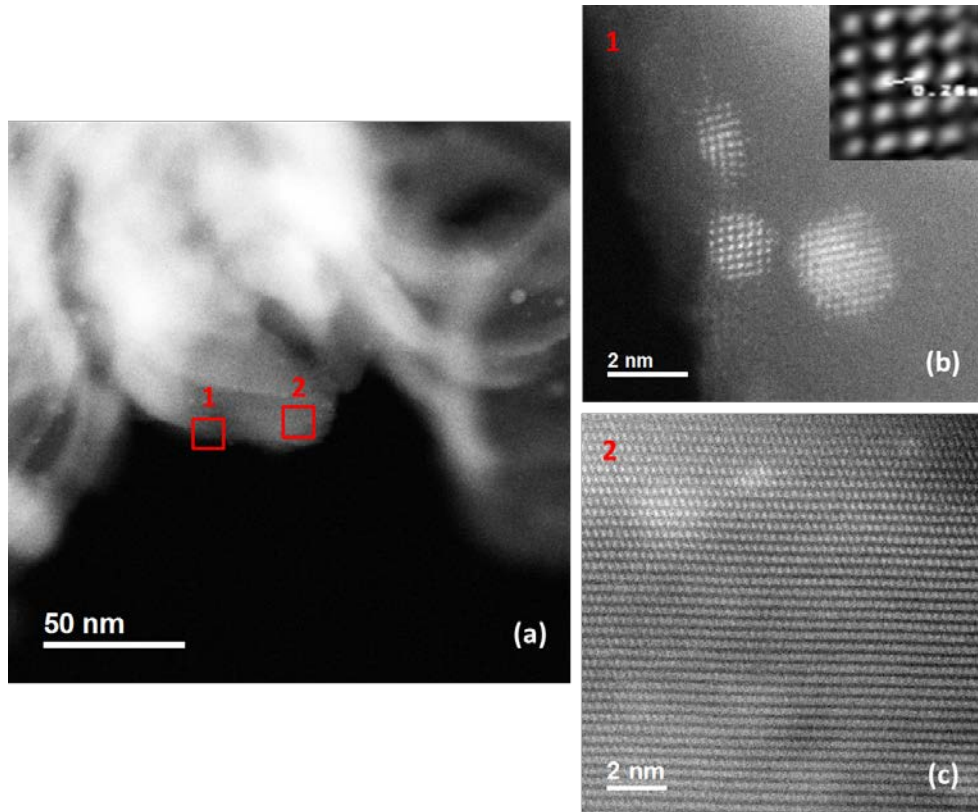


**Figure 5.22** (a) Z-contrast STEM image of the surface of a few rings of $Sr^{2+}$-doped $TiO_2$ nanotubes. (b) and (c) High resolution images taken from specified regions in (a)

showing segregation of cubic SrO at the edge with the lattice parameter of 0.26 nm in the simulated image in inset.

Figure 5.22 shows the Z-contrast STEM images of a few rings of $Sr^{2+}$-doped $TiO_2$ nanotubes. It is observed that from Figure 5.21 (a) that the Z-contrast intensity is drastically changing between the two heterophases. The atomic structure of the segregated nanoclusters was seen to be matching the cubic lattice of SrO with the measured lattice parameter of 0.26 nm. The atomic resolution Z-contrast STEM images of different regions on the rings are shown in Figure 5.23. The middle region of the ring specified as b and shown in Figure 5.23 (b) shows the arrangement of the Ti atoms in the anatase $TiO_2$ with tetragonal structure and the lattice parameters as measured in FFT reconstructed image of $a = b = 0.38$ nm. A few bright spots can be also observed in this image. As we go along the arrow to region c, a number of bright spots start to appear in the vicinity of the $TiO_2$ lattice. These bright spots correspond to Sr atoms that are randomly distributed in the lattice of $TiO_2$ and have caused displacement of some atoms from their original position in the lattice. The nanoclusters were also observed to be changing gradually to a similar structure to that of $TiO_2$ matrix at the vicinity of the heterointerface. However, as we get close to the interior edge of the ring, the segregated SrO clusters with cubic structure are observed with the atomic arrangement in (111) planes as shown in FFT reconstructed image. The $d$-spacings from these regions are measured to be in a range from 0.293 to 0.298 nm, corresponding to the (111) planes. As a result, it is concluded that such preferential growth of the SrO on the surface and at the interior edges of the nanotubes can be related to the disordering and instability of the surface atoms acting as nucleation sites for the growth of nanoclusters.
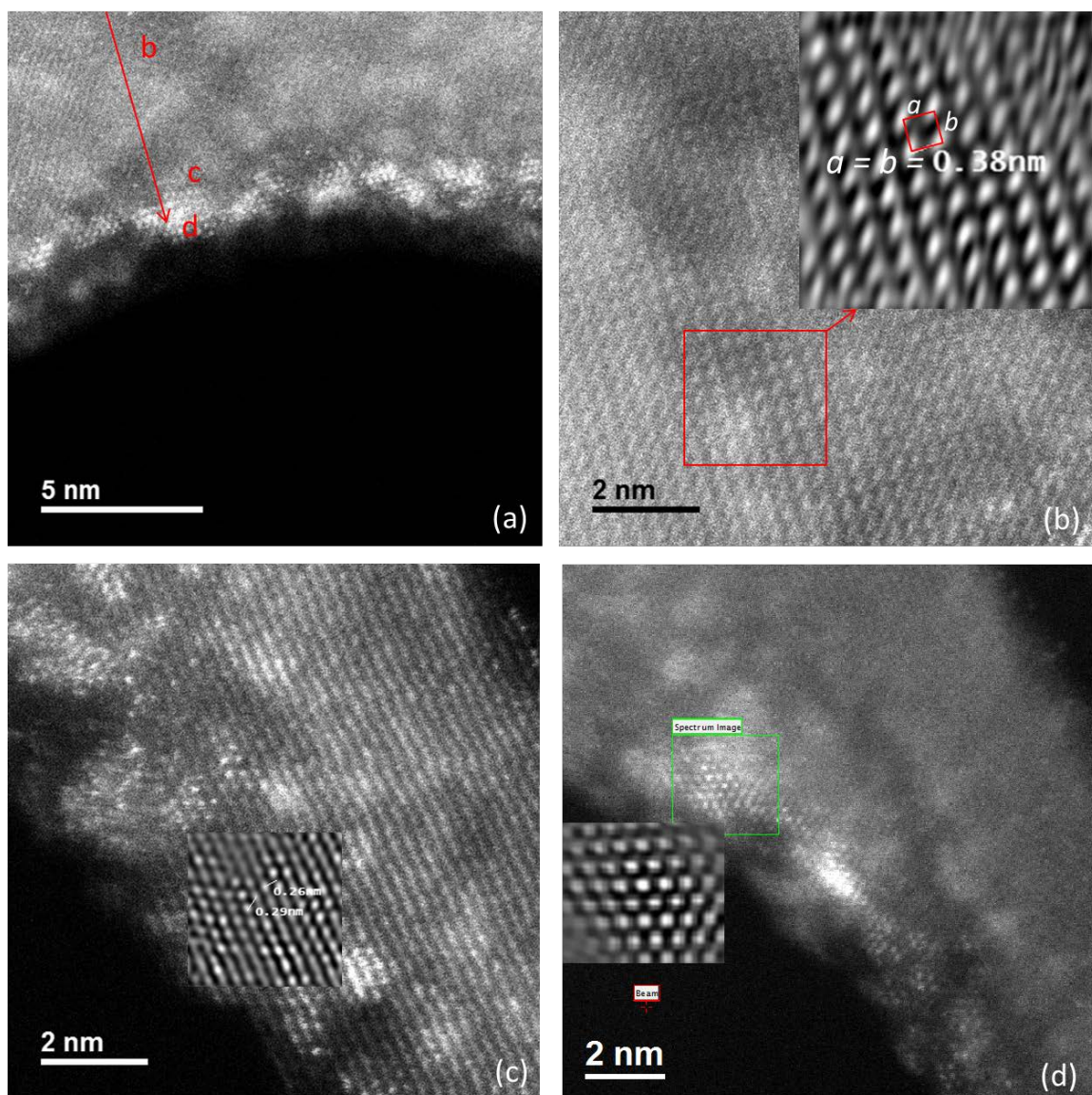
**Figure 5.23** (a-d) Atomic resolution Z-contrast STEM images of the surface of a ring of $Sr^{2+}$-doped $TiO_2$ nanotube showing the distribution of Sr in different regions on the surface.

The significance of formation of SrO nanoclusters in the $TiO_2$ anatase matrix can be regarded as the effect of the presence of the heterointerface between the SrO and $TiO_2$ in photocatalytic efficiency of the material as reported by Chen et al. [125]. The authors have investigated, for the first time, the photoactivity properties of $TiO_2$ nanotubes filled with $TiO_2$ nanoparticles and further coated with a layer of strontium oxide. Their result revealed that the SrO-coated $TiO_2$ nanotubes show higher solar-to-electricity conversion efficiency ($\eta$) than the uncoated nanotubes. This improvement has been related to the possible effect from the presence of the SrO as a thin potential barrier layer that inhibits the charge recombination at the electrode/electrolyte interface, thereby increasing the efficiency. It has been also suggested that there is a possibility that the treatment with SrO can form a surface layer $SrTiO_3$ on $TiO_2$ nanotubes, (with higher CB level than pure $TiO_2$), an effect that has been already shown to improve the efficiency of the entire material system [30, 47].

## 5.3. Optical Absorption Measurements of $Sr^{2+}$-doped $TiO_2$ Nanotubes

In order to investigate the optical properties of the fabricated electrodes, UV-Vis absorption spectra were measured for the synthesized $Sr^{2+-}$doped nanotube arrays after annealing. The absorption edge for each sample is also displayed in higher magnification in inset. In the case of sample ST2 at pH = 3 and samples ST3 at pH = 2,3, the absorption edge is mixed with some unwanted scattered components. The absorption edge in these samples is determined similar to optical bandgap determination from Tauc plot; using a moving average smoothing technique, the absorption edge was obtained by finding the x-

intercept of a section of straight line at the most steep part of the curve (on the absorption

spectrum) extended to the x-axis (Figure 5.24 (a)) [126].
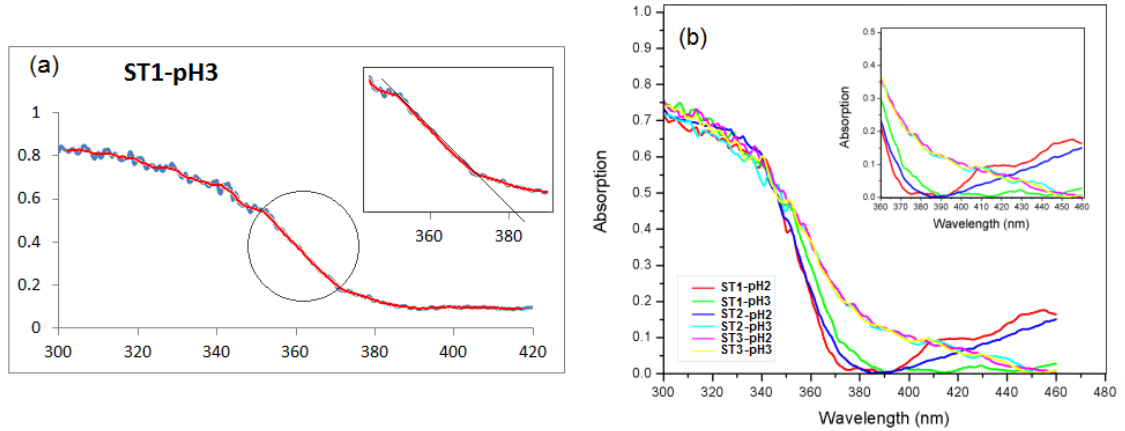


**Figure 5.24** (a) Smoothing UV-vis absorption spectrum of a typical sample (annealed

ST1-pH3) using the moving average technique; the slope of the most steep part of the

curve is shown in the inset. (b) Variation of the UV-vis absorption spectra of annealed

$Sr^{2+}$-doped $TiO_2$ nanotube samples with different Sr-dopant concentrations and pH

values. The absorption edge is observable in the magnified graph at the top.
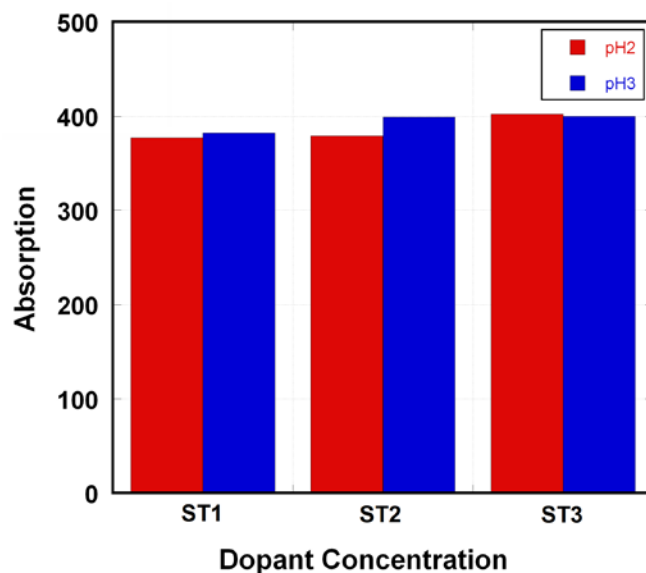
**Figure 5.25** Variation of the absorption edge in samples with Sr-dopant concentration and pH of electrolyte. Note that the red squares correspond to pH = 2 and the blue ones relate to pH = 3.

Figure 5.24 (b) shows variation of the DRS UV-vis spectra of $Sr^{2+}$-doped $TiO_2$ nanotube samples with different concentrations of the dopant. In general, the absorption edge of the $Sr^{2+}$-doped $TiO_2$ nanotube samples shows a red shift with increasing the Sr dopant concentration. Also, increasing the pH of the electrolyte results in red shifting of the absorption edge of the material at given dopant concentration. In case of pH = 2, by increasing dopant concentration, the absorption increases from 377 ± 2 nm to 379 ± 2 nm and reaches the maximum value of 402 ± 2 nm at the highest dopant concentration. When the pH is changed to 3, increasing dopant concentration resulted in slightly enhancement of the corresponding absorption edge values in samples ST1 and ST2; however, this trend was not observed in sample ST3 as slightly lower absorption edge value of 400 ± 2 nm was obtained compared to that of 402 ± 2 nm for the same dopant concentration at pH = 2

(Figure 5.25). The overall trend observed in all samples can be attributed in detail to the relation between processing parameters and the morphological and electrochemical properties of the synthesized nanotubes. As seen in this Table 5.4, both processing parameters such as dopant concentration and the pH of the electrolyte affect primarily the tube length of the samples. The error bar for the absorption edge values indicate the maximum typical error in the absorption edge for reference materials following internal calibration and spectral processing. As mentioned earlier, the change in tube length in terms of pH is much more significant in the samplesST1 and ST2, while in the case of the sample ST3, although the tube length is not doubled, still 300 nm increase in the length is observable when the pH is changed from 2 to 3.

**Table 5.5** Summary of the Properties of Sr-doped $TiO_2$ nanotube samples in terms of processing parameters.

| Processing Parameters | | Properties | |
|---|---|---|---|
| Sample | pH | Average Tube Length ($\pm 0.05\mu m$) | Abs. Edge ($\pm 2$ nm) |
| ST1 | 2 | 0.7 | 377 |
|  | 3 | 1.4 | 382 |
| ST2 | 2 | 0.5 | 379 |
|  | 3 | 1.0 | 399 |
| ST3 | 2 | 1.1 | 402 |
|  | 3 | 1.4 | 400 |

## 5.4 Conclusion

In this chapter, fabrication of $Sr^{2+}$-doped $TiO_2$ nanotubes via one step electrochemical anodization technique was reported. Self-organized nanotube arrays of $Sr^{2+}$-doped $TiO_2$ have been fabricated and characterized at various concentrations of $Sr(OH)_2$ and at different electrolyte pHs. Characterization of the as-anodized nanotubes revealed that dopant concentration, up to the solubility limit of $Sr(OH)_2$, and pH of the electrolyte significantly influence the morphology and length of the doped nanotubes. The doping mechanism of highly ordered $Sr^{2+}$-doped $TiO_2$ nanotube arrays were discussed by detail analysis of the bulk structure and surface characteristics of the doped nanotubes using XRD, XPS and NEXAFS measurements. At low dopant concentrations, it was shown that the Sr-doping results in expansion of the tetragonal lattice of the $TiO_2$ nanotubes. Furthermore, the insertion of the dopant was shown to change the oxidation states of Ti along the length of the nanotubes. The NEXAFS surface analysis of the doped nanotubes revealed that $Sr^{2+}$ doping only alters the Ti and O ions interaction in the $TiO_2$ lattice on the surface and has no evident effect on their individual charge states. In addition, from NEXAFS experiments at different incident beam angles, a relation was obtained between the preferential crystal orientation in the highest doped nanotubes sample obtained from texture analysis of the bulk and the orientation of the octahedral units on the surface. The combination of high-resolution Z-contrast imaging and EELS SI mapping also revealed possible phase segregation of SrO on the surface of the nanotubes

at highest doping level. Formation of such heterointerfaces between the SrO and $TiO_2$ phases observed in the highest doping content in $Sr^{2+}$-doped $TiO_2$ nanotubes can be also considered as a key feature in evaluation of the possibility of enhancement in photocatalytic properties and thus, the use of such material as a functional nanomaterial for other applications. The results of the surface and bulk analyses suggested that the structural modification from Sr dopant in the $TiO_2$ nanotube structure was strongly sensitive to the dopant concentration as well as the growth conditions. It was also revealed that Sr doping of $TiO_2$ nanotubes up to the concentration close to the salt solubility limit can red shift the absorption edge of the material to as long as 402 nm. The incorporation of the Sr in the $TiO_2$ lattice as well as the formation of Sr- rich $TiO_2$ clusters on the surface may have contributed to a decrease in the bandgap and the enhancement in the photocatalytic activity as discussed in Appendix A.

# CHAPTER 6

# DEVELOPMENT OF THIN-FILM STRONTIUM TITANATE

# NANOTUBE ARRAYS ON SILICON

## 6.1 Fabrication and Characterization STO NTAs

In this chapter, the fabrication, characterization and growth mechanism of thin-film $SrTiO_3$ (STO) nanotube arrays on silicon is reported for the first time.

### 6.1.1 Titanium Thin-Film Deposition

The n-type (100) Si wafer (500 µm in thickness) was cut into 1 cm x 2 cm pieces and was used as substrate for thin-film deposition. Prior to deposition, the Si substrates were degreased by sonication in acetone, methanol and isopropanol and rinsed with deionized (DI) water and dried in a nitrogen stream followed by oxygen plasma cleaning. The Ti film was then deposited onto Si substrate using dc magnetron sputtering. The chamber was first evacuated to the pressure of $2.0 \times 10^{-7}$ torr and the argon gas pressure was then maintained at $6.0 \times 10^{-4}$ torr during the deposition. The sputtering power and the deposition temperature were held constant at 125 W and 500 °C, respectively. The sputtering rate of titanium was found to be ~ 1 Å/sec. Based on this rate, the sputtering time was set to obtain a maximum sputtered thickness of 6 µm for titanium.

### 6.1.2 Growth of Thin-Film $TiO_2$ Nanotube Arrays on Si Substrate

To evaluate the effect of starting $TiO_2$ material on growth mechanism of STO NTAs, self-organized $TiO_2$ nanotube arrays were grown by electrochemical anodization

of Ti thin-films on Si substrates in two different electrolytes as explained earlier. In the first route, the TiO$_2$ nanotube arrays were grown in a conventional two electrode cell in an aqueous solution of 0.5 wt% HF and 1 M H$_2$SO$_4$ and at a constant temperature of 4 °C. The anodization voltage was held at constant voltage of 10 V during 30 min and 1 h. The second route was followed by room temperature anodization of the Ti thin-film in an organic electrolyte consisting of ethylene glycol (EG) and NH$_4$F, at the constant voltage of 40V and for the same durations. Both TF-TNAs samples were annealed at 420 °C for 4 hours and the heating rate of 1 °C/s to form crystalline anatase phase.

## 6.1.3 Synthesis and Characterization of Thin-Film SrTiO$_3$ Nanotube Arrays on Si Substrate

The two types of annealed thin-film TiO$_2$ NTAs were used in hydrothermal treatment for synthesis of thin-film STO NTAs on silicon. A 0.025M strontium containing solution was prepared by fully dissolving 0.151 g of anhydrous Sr(OH)$_2$ in 50 mL DI water. The annealed thin-film TiO$_2$ NTAs on Si substrates were immersed in the solution in a 45 mL Teflon-lined autoclave and heated at 180 °C for different reaction times. After the hydrothermal treatment, the autoclave was subsequently cooled down to room temperature. The samples were ultrasonicated in DI water to remove the residues and dried in air for characterization and electrical measurements. The pH of the starting solution was measured to be 12.
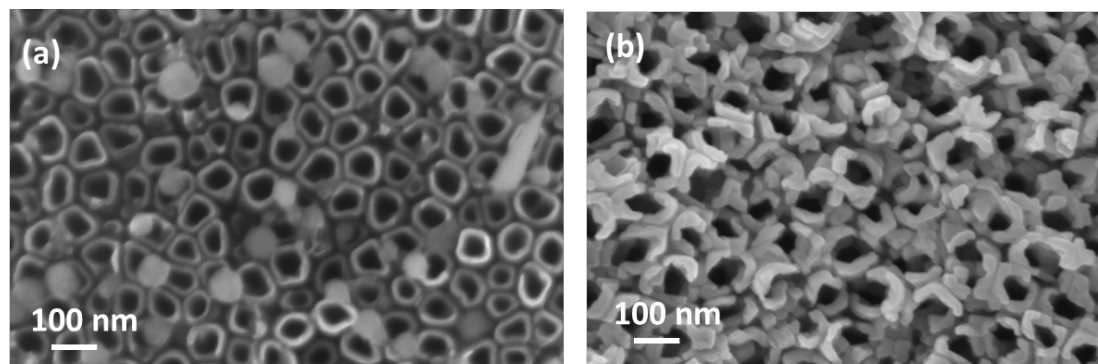
**Figure 6.1** (a) FESEM images of (a) aqueous intact $TiO_2$ NTAs and (b) partially converted organic- derived $TiO_2$ nanotubes to $SrTiO_3$ at T = 150 °C after 5.5 h.

Figure 6.1 shows the FESEM images of the aqueous and organic $TiO_2$ NTAs that were hydrothermally treated in $Sr(OH)_2$ solution at T = 150 °C and for 5.5 h. As can be seen in Figure 6.1 (a), it was found that at the same reaction temperature and time, the nanotubes prepared in aqueous route have remained intact and did not undergo the reaction and further the surface was instead covered with precipitates of the strontium oxide nanoparticles. However, in the case of organic nanotubes, the initial stages of the nucleation process has occurred (Figure 6.1 (b)). (For the comparison of the morphology of the annealed aqueous and organic $TiO_2$ NTAs on silicon, the reader is referred to section 4.2.2.)
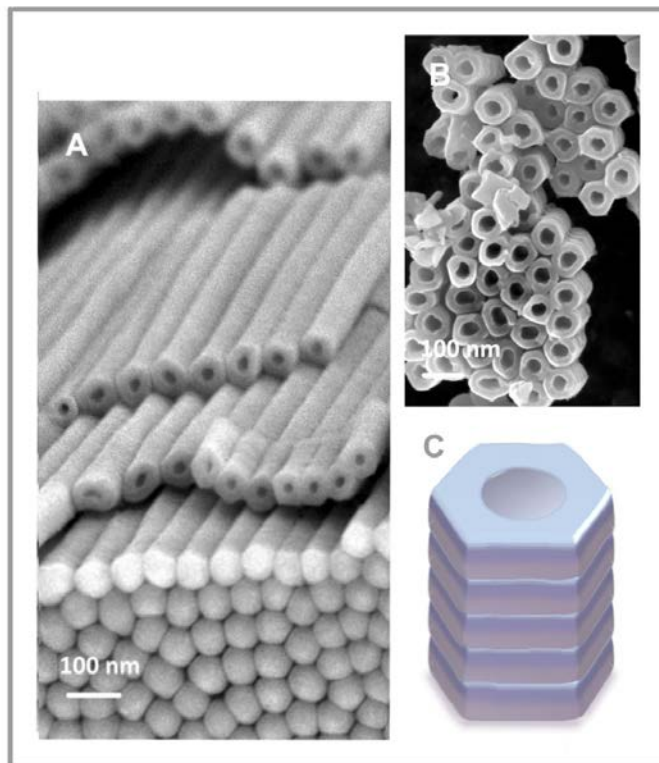
**Figure 6.2** (A) and (B) FESEM image of the bottom and top side of annealed $TiO_2$ NTAs on silicon. (C) Schematic of a single nanotube showing the hexagonal-like morphology of the tubes.

Figure 6.2 shows more details about the morphology of the organic-derived nanotubes, including back and top side of annealed $TiO_2$ NTAs on silicon. As can be seen, the backside of the nanotubes is closed and the top side is composed of an ideal close-packed arrangement of the tubes of uniform diameters ($\sim$ 50 nm) which gets smaller from the top to the bottom. A schematic of a single nanotube is shown in Figure 6.2 (C) which reveals the morphology of each single nanotube is composed of several hexagonal plates that are stacked on top of each other to form the entire nanotube. As opposed to aqueous route, such morphology is generally a characteristic of the $TiO_2$

NTAs synthesized in organic solutions. Surprisingly, it was found that the arrangement of these plates with sharp edges at the outer circumference of the tube assists the formation of highly crystalline $SrTiO_3$ crystals as compared to $TiO_2$ NTAs that are formed in aqueous solution where the nanotubes are composed of stacked rings with relatively amorphous structure around the tube. It has been also reported that the morphology of $TiO_2$ affects the growth of cubic $SrTiO_3$ [127]. Figure 6.3 shows TEM and FESEM images of the $TiO_2$ nanotubes prepared in aqueous and organic solutions for comparison of the crystallinity of the outer layers of the $TiO_2$ nanotubes. As can be observed from FFT of the selected areas on the outer edges of the nanotubes, the aqueous nanotube is composed of an amorphous layer whereas the organic nanotube has straight walls in which the grains with preferred orientation of the crystallographic (101) planes are extended to the outer layer of the tube walls. Such a single crystal type of diffraction pattern can only be produced when all nanocrystals are aligned in more or less identical crystallographic orientation. Such a difference in the crystallinity as well as the orientation of the grains at the exterior walls of the starting $TiO_2$ NTAs was found to be effective in crystallization mechanism of $SrTiO_3$ in terms of the growth rate and the final morphology of the nanotubes. Thus, the organic nanotubes were used as the template and the titanium source for synthesis and investigation of the growth mechanism of $SrTiO_3$ NTAs.
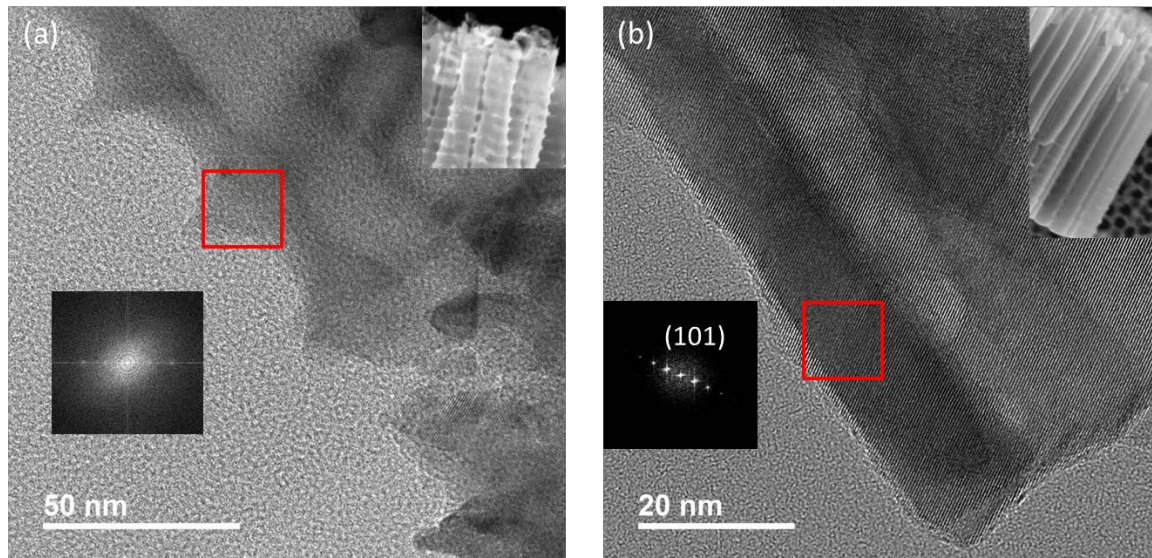
**Figure 6.3** (a) TEM and FESEM images (shown in insets) and the corresponding FFT taken from the edges of the TiO$_2$ nanotubes prepared in (a) aqueous and (b) organic solutions.
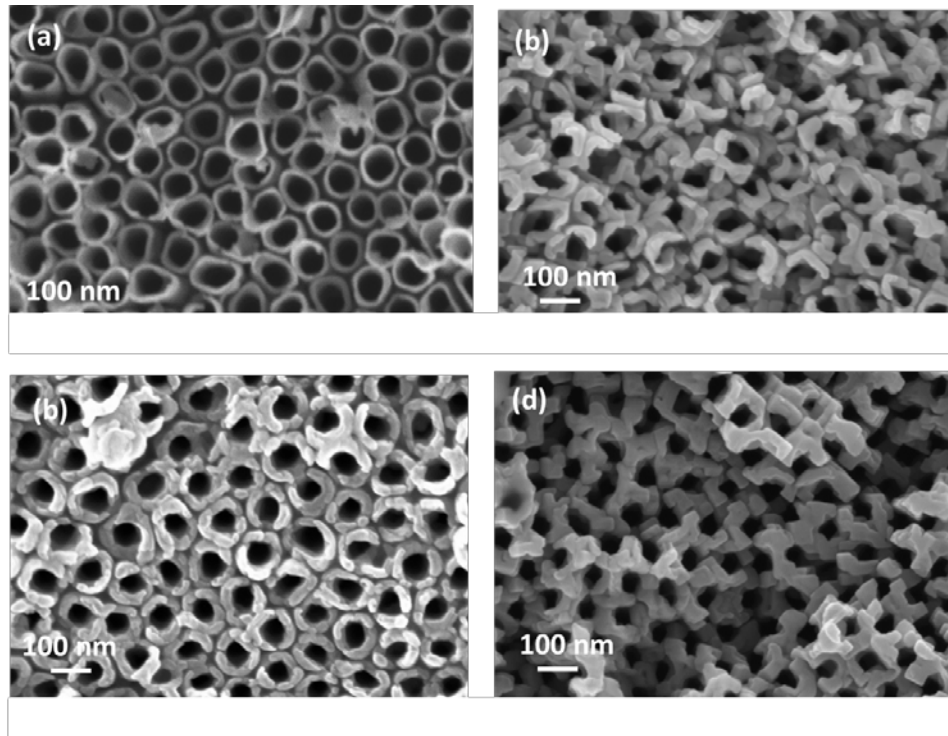
**Figure 6.4** (a) FESEM images of (a) TiO$_2$ NTs, (b) partially converted nanotubes to SrTiO$_3$ at T = 150 °C after 5.5 h and (c) partially converted nanotubes to SrTiO$_3$ at T = 180 °C after 5.5 h and (d) and cubic SrTiO$_3$ at T = 180 °C, after 18 h.



| Phase | Weight fraction |
|---|---|
| Anatase TiO$_2$ | 0.16 |
| SrO | 0.01 |
| SrTiO$_3$ | 0.83 |
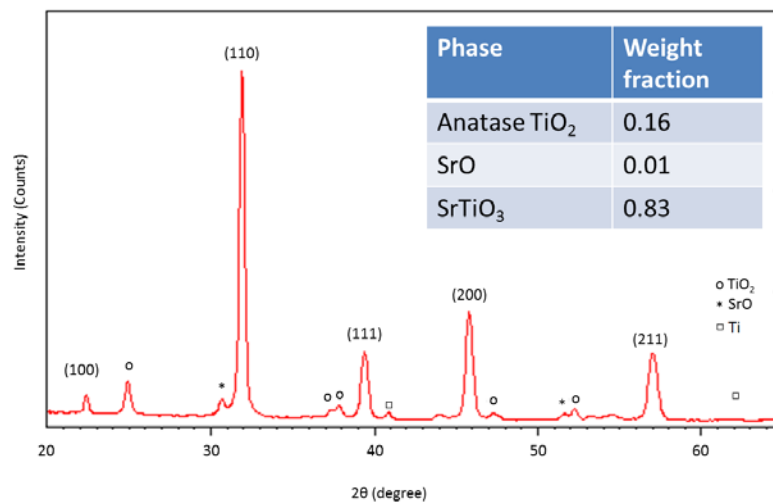
**Figure 6.5** GIXRD pattern of organic TiO$_2$ NTAs converted to cubic SrTiO$_3$ at T = 180 °C for 18 h and the quantitative phase analysis in the inset table.

Figure 6.4 shows the FESEM image of the pure and hydrothermally treated $TiO_2$ NTAs at various reaction times and temperatures. The corresponding GIXRD patterns of the $SrTiO_3$ at T = 180 °C after 18 h is also shown in Figure 6.5. It can be inferred that the reaction temperature, and more importantly the reaction time, can significantly change the morphology of the final structure. Based on the results of quantitative analysis of GIXRD data, it was found that 83 wt. % (~79 % volume fraction) of the $TiO_2$ anatase has completely converted to cubic $SrTiO_3$ according to $SrTiO_3$ after 18 h at 180 °C (JCPSD card No. 89-4934). The average crystallite size of the $SrTiO_3$ was found to be 23 nm by Scherrer analysis [128]. Small peaks corresponding to SrO and $TiO_2$ with weight fraction of ~1% were detected. No evidence of other phases was detected from GIXRD apart from $SrTiO_3$ confirming that there is no appreciable chemical reaction between the $SiO_2$ substrate and the $SrTiO_3$ at that temperature and time. The lattice spacings of the $SrTiO_3$ (100) and (110) planes are calculated to be 0.396 nm and 0.281 nm, respectively. $SrTiO_3$ samples were further analyzed by TEM. Figure 6.6 shows a low-magnification bright-field TEM image and the SAED pattern of the STO NTAs that were synthesized on silicon. The polycrystalline nature of the STO NTAs with rings indexed to (100), (110), (111) and (200) planes are observed. This reveals the formation of NTAs of cubic $SrTiO_3$ after hydrothermal treatment of organic $TiO_2$ NTAs at 180 °C for 18h.
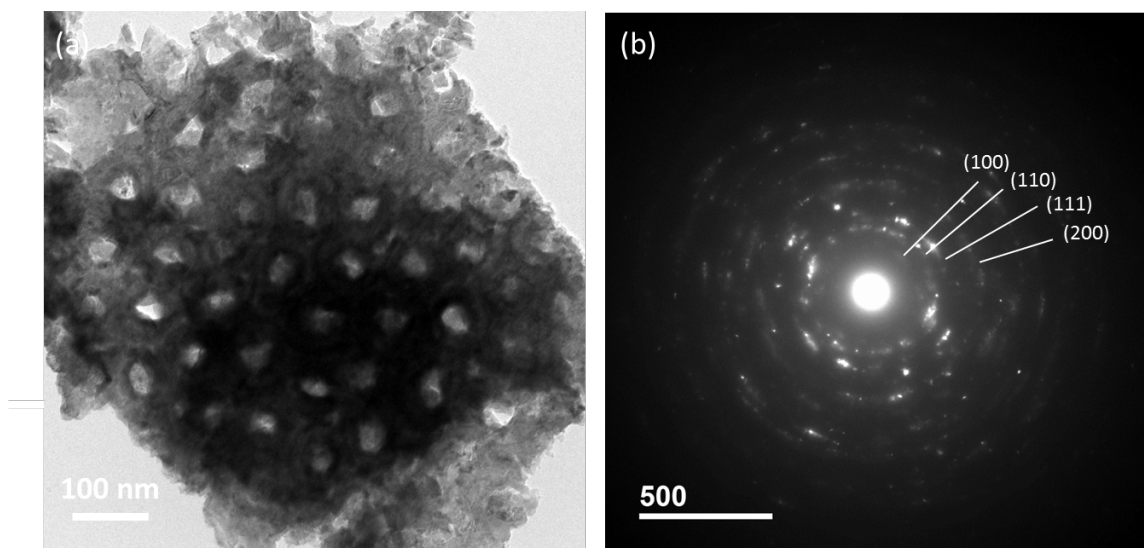
**Figure 6.6** (a) Top view TEM image of STO NTAs prepared at 180 °C for 18h and the corresponding SAED pattern showing the polycrystalline sample with rings indexed to (100), (110), (111) and (200) planes.

Figure 6.7 shows the XPS core level photoemission spectra for O $1s$, Ti $2p$, and Sr $3d$ in for synthesized $SrTiO_3$ NTAs on silicon and the corresponding binding energies summarized in Table 6.1. Results from peak fitting on all spectra additionally confirmed the complete exchange of $Sr^{2+}$ ions as well as formation of $SrTiO_3$ with the elements in chemical states associated to $SrTiO_3$.
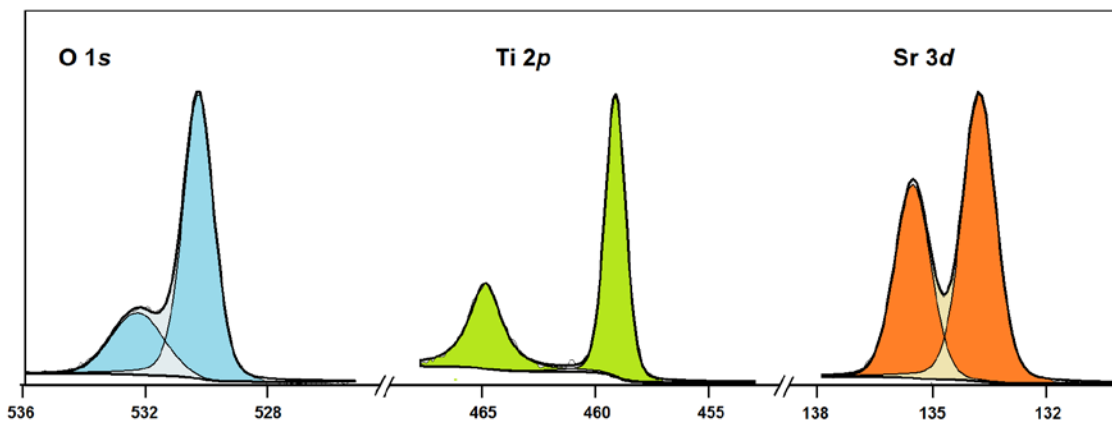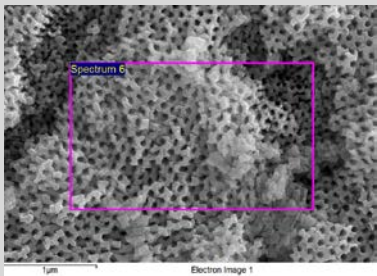
**Figure 6.7** XPS core level photoemission spectra for O 1*s*, Ti 2*p*, and Sr 3*d* in for synthesized SrTiO₃ NTAs on silicon.

**Table 6.1** XPS core level binding energies of O 1*s*, Ti 2*p*, and Sr 3*d* in for synthesized SrTiO₃ NTAs on silicon.

| | O 1*s* | | Ti 2*p* | | Sr 3*d* | |
|---|---|---|---|---|---|---|
| **Element** | $O_{lattice}$ | $O_{lattice}$ | Ti $2p_{1/2}$ | Ti $2p_{3/2}$ | Sr $3d_{3/2}$ | Sr $3d_{5/2}$ |
| **Binding Energy (eV)** | 530.225 | 532.226 | 459.085 | 464.830 | 133.750 | 135.485 |

**Table 6.2** EDS chemical composition of the SrTiO₃ NTAs obtained from different regions on the surface.

| Element | App Conc. | Intensity Corrn. | Weight% | Weight% Sigma | Atomic% |
|---------|-----------|------------------|---------|---------------|---------|
| O K | 17.74 | 0.5343 | 32.19 | 0.51 | 67 |
| Ti K | 23.10 | 0.9118 | 24.55 | 0.29 | 17 |
| Sr L | 39.93 | 0.8948 | 43.26 | 0.42 | 16 |
| Totals | | | 100.00 | | |

| Element | App Conc. | Intensity Corrn. | Weight% | Weight% Sigma | Atomic% |
|---------|-----------|------------------|---------|---------------|---------|
| O K | 15.68 | 0.5223 | 30.29 | 0.52 | 65 |
| Ti K | 22.93 | 0.9155 | 25.28 | 0.30 | 18 |
| Sr L | 39.60 | 0.8993 | 44.43 | 0.43 | 17 |
| Totals | | | 100.00 | | |
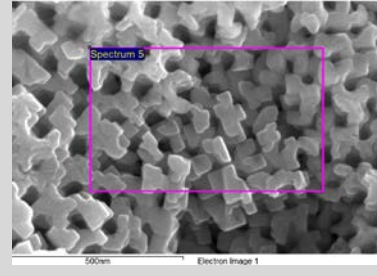
Table 6.2 shows the EDS chemical composition of the SrTiO₃ NTAs at two different areas and at various magnifications on the surface. As can be seen, the composition of the film is very close to stoichiometric ratio, i.e., Sr/Ti = 1. Figure 6.8 shows the cross section FESEM images of the SrTiO₃ nanotubes from top and bottom sides. As seen, the surface of the nanotubes is composed of cubes oriented around the nanotubes whereas the walls of the nanotubes are composed of brick-like morphology that are oriented along the longitudinal direction.
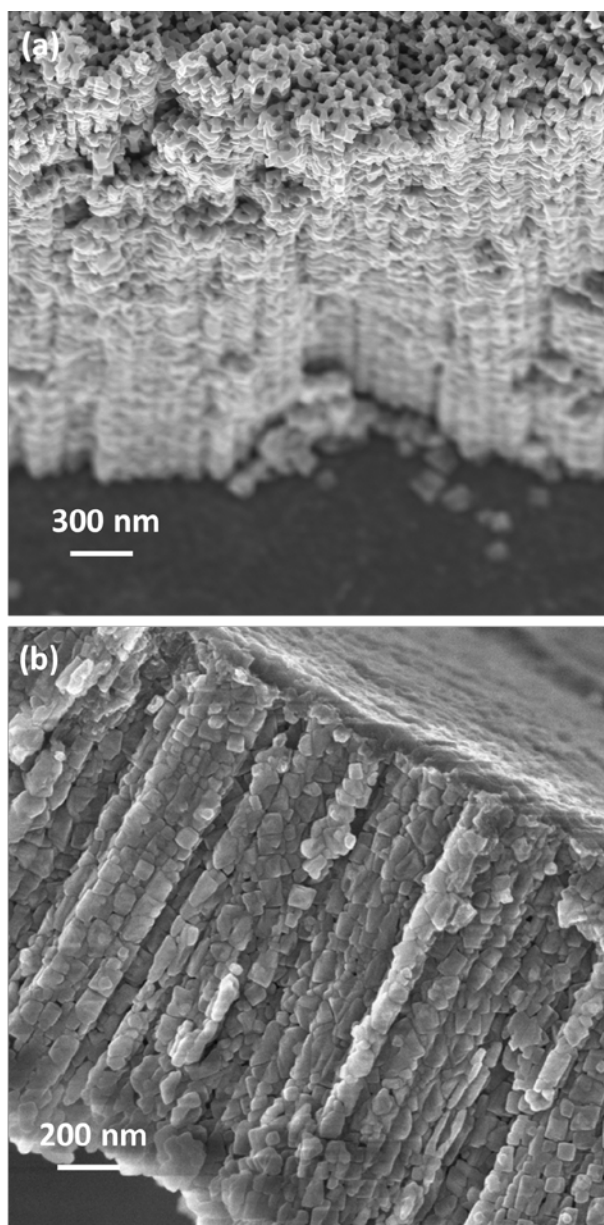
**Figure 6.8** Cross section FESEM images of the SrTiO$_3$ nanotubes from (a) top and (b) bottom views.

## 6.2 Growth Mechanism of Thin-Film SrTiO$_3$ Nanotube Arrays on Si Substrate

Generally, two major parameters control the morphology and composition of the final product in the hydrothermal process. One of these parameters is the reaction

temperature. It has been reported that the optimal reaction temperature of preparing cubic $SrTiO_3$ perovskites is about 180 °C [127]. This has been also observed in our hydrothermal process especially when the $SiO_2$ is present in the reactive environment. Below this temperature, the structure is found to be mostly composed of tiny particles forming around the $SrTiO_3$ cubes, while above this temperature, the agglomeration of the cubes results in collapse of the nanotubes structure. The other parameter is the reaction time. Different annealing times were found to influence the degree of $SrTiO_3$ crystallization. It has been reported that well-distributed cubic crystals of $SrTiO_3$ with smooth surfaces can be obtained after 12 h of the hydrothermal annealing at 180 °C [127]. By stabilizing the reaction temperature and the reaction time, we found a challenge in synthesis of cubic $SrTiO_3$ nanocrystals while preserving the shape of the nanotubes. As such, we found it necessary to investigate the growth mechanism of the thin-film $SrTiO_3$ nanotube arrays to understand the critical steps for controlling the tubular morphology during the crystallization and growth process. The growth mechanism involves three major steps that is supported by the FESEM images and schematics shown in Figure 6.9.

Likewise for the processing of other ternary oxides via a template reaction approach with a hydrothermal process, the architecture and composition of the final product is a consequence of typical dissolution-precipitation reactions that take place as the following. The formation of $SrTiO_3$ in hydrothermal treatment of $TiO_2$ is also very sensitive to the solution pH and it takes place when properly alkaline conditions (pH $\geq$ 12) are attained [129, 130]. The process starts with breaking Ti-O bond via hydrolytic attack to form a soluble $[Ti(OH)_6]^{-2}$ complex [48]:

$$TiO_2 + 2OH^- + 2H_2O \rightarrow [Ti(OH)_6]^{-2} \tag{6.1}$$

Then, the precipitation of SrTiO$_3$ takes place according to the following reaction:

$$Sr^{2+} + [Ti(OH)_6]^{-2} \rightarrow SrTiO_3 + 3H_2O \qquad (6.2)$$
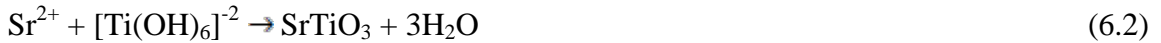
These two reactions result in the following total reaction:

$$TiO_2 + Sr(OH)_2 \rightarrow SrTiO_3 + H_2O \qquad (6.3)$$

Dissolution of TiO$_2$ and precipitation of SrTiO$_3$ occur in the vicinity of the nanotube surfaces. Since free surfaces and, hence, free [Ti(OH)$_6$]$^{-2}$ groups are mainly more available at the top and inside of the 1D tube channels, the precipitation process starts by preferential nucleation of SrTiO$_3$ at the top layer as well as the inner surface of the nanotubes. It is observed that the nucleation rate is the highest at the top surface and it drops towards the end of the nanotubes.

The phase conversion takes place via reaction (6.2) until continuous nucleation and crystallization of the SrTiO$_3$ nanocrystals is occurred through the entire thickness and along the nanotube walls (Figure 6.9 (A)). As can be seen in this figure, after the second reaction has elapsed for some time, due to the small diameter of the nanotubes, transportation or diffusion of Sr$^{2+}$ and OH to the reaction sites away from the surface becomes more difficult, and hence, reaction 1 and then reaction 2 will be retarded [48]. This is very well evidenced from Figure 6.8 wherein the crystals are larger and relatively more oriented along the tube axis at the very top and close to the open side of the nanotube arrays while they become smaller and quite randomly oriented at the end side of the nanotubes. The crystallization stage is followed by a change in the shape of the crystallites starting from the exterior side of the nanotubes walls rather than the interior side. At this step, the shape of the SrTiO$_3$ nuclei starts to gradually change to cubic-type

of crystals at the top surface and then along the walls of the nanotubes. In fact, the crystallization takes place by formation of facets in the crystallites at the exterior side of the nanotube walls while the interior side of the crystallites still remains curved as shown in Figure 6.9 (C) and (D). It appears that the presence of a single crystalline type of grains with preferential orientation of (101) planes at the outer surface of the starting (organic-derived) $TiO_2$ nanotubes walls facilitates the phase transformation and therefore the faster growth of $SrTiO_3$ cubic facets at the outer side. This can be due to the preferred adsorption of hydrated OH anions on the stoichiometric anatase (101) surface as reported elsewhere [131]. When the cubic crystallites at the exterior side of the nanotube walls enter into the growth step, continuous nucleation inside the pore region inside the nanotubes (due to more availability of the reactants in this area) is still taking pace. This results in formation of "L" shape crystallites with a concave interior and the straight facets at the exterior composing the $SrTiO_3$ crystal structure at this stage.
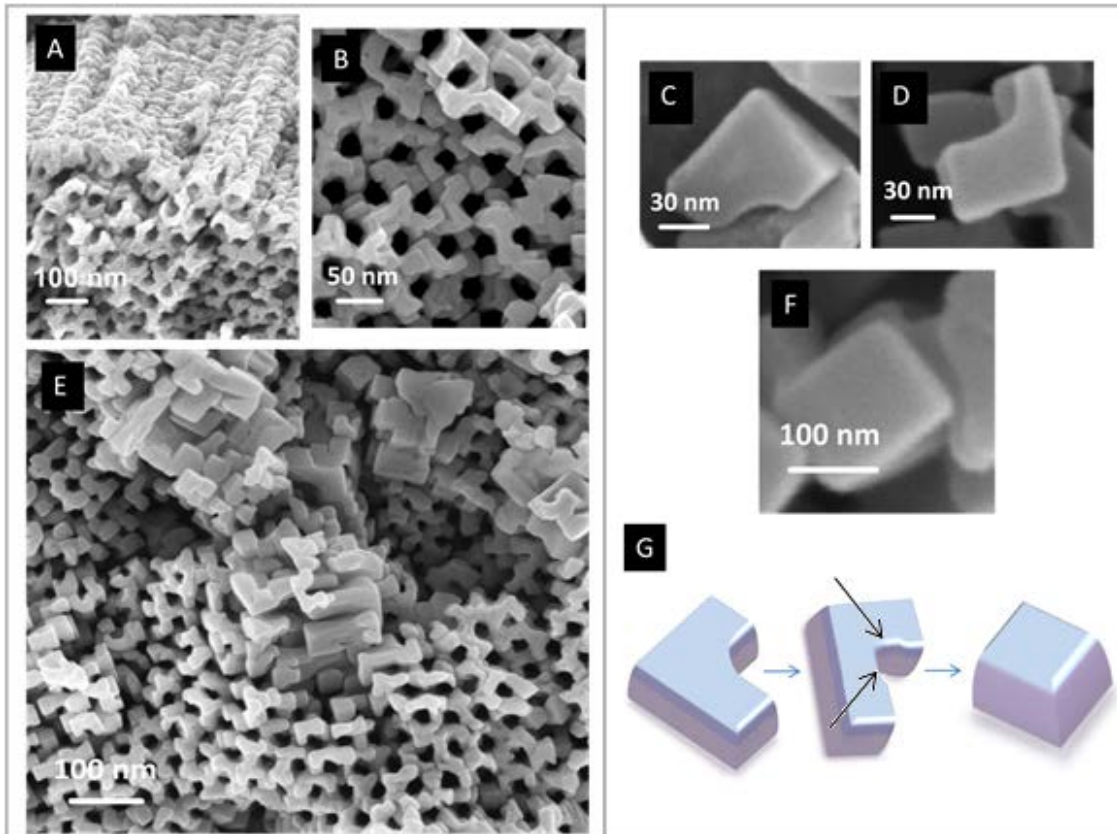
**Figure 6.9** Cross section and top view FESEM images of $SrTiO_3$ nanotubes at (A) nucleation and (B) after the growth; (C-F) STO crystallites formed around the nanotubes showing different morphology of the inner and outer surfaces. (G) Schematic showing three consecutive stages of the growth mechanism. (Black arrows show the nucleation sites at the inner side of the crystallites).

As the nucleation completely stops, the growth step is further accompanied by self-assembly of the cubes around the nanotube walls to produce highly organized arrays of cubic nanocrystals. The last step of such self-alignment takes place when the size of the crystals becomes comparable with the curvature of the nanotube. Due to steric constraints crystals start to self-organize in order to most efficiently fill the available

surface of the pore walls [132]. This process leads to the formation of large number of self-aligned cube domains (as shown in Figure 6.9 (E)) which tend to grow to single larger cubes (Figure 6.9 (F)). The smallest crystallite size at the early stages of the growth was estimated ~ 20 nm from XRD data. However, after completion of the growth, the cubes were found to grow to a size as large as 100 nm. At this point when the size of these cubes becomes comparable to the size of the pores, the nanotube structure starts to collapse into a randomly porous structure. A summary of the three stages of the growth mechanism is shown in the schematic of Figure 6.9 (G).

## 6.3 Conclusion

The fabrication, characterization and growth mechanism of $SrTiO_3$ nanotube arrays on silicon was investigated. Using a simple hydrothermal method, the growth morphology of STO NTAs on previously fabricated $TiO_2$ NTAs on silicon was investigated at various reaction times and temperatures. It was assumed that the nucleation starts from the exterior side of the nanotube walls where surface morphology and crystal orientation of the planes plays an important role in the growth rate as well as the final morphology. The as-synthesized STO NTAs were found to be crystalline with ~ 80 wt. % transformation of $TiO_2$ to stoichiometric $SrTiO_3$ at 180 °C and 18h. The size of crystallites was found to change from ~20 nm at the early stages of the growth to as large as 100 nm cubes. This is the critical point at which the cube size becomes comparable to the size of the pores and as a result the nanotubular structure starts to alter into a randomly porous structure.

# CHAPTER 7

# DEVELOPMENT OF COAXIAL HETERO-NANOSTRUCTURES

# FOR MICRO-SOFCS

## 7.1 Overview

As discussed in previous chapters, the tubular arrays of metal oxides offer a large surface area and highly defined paths for diffusion of species (e.g., electrons, holes, ions) through the tube walls and interfaces. Moreover, the functionality of ordered tube arrays can be improved when combined with the effects of heterointerfaces and the charge transfer at the nanoscale. Hence, a high surface-area nanotubular array of metal oxide that is conformally coated from inside and outside by another metal oxide is introduced as a new design scheme for more efficient charge transfer over the classical thin-film approach- for example thin-film electrolyte layers in applications such as SOFCs.

In this chapter, the development of hetero-nanostructures (HNSs) of YSZ/Sr-doped $TiO_2$/ and YSZ/STO is discussed. Arrays of vertically-oriented nanotubes of Sr-doped $TiO_2$ and STO nanotubes were chosen as the backbone structure with the wall thickness on the order of 5 nm to 20 nm to act as the support and one of the oxide layers of the HNSs. By coating the nanotubes with the second oxide layer (the best-known oxygen ion conductor oxide for SOFC electrolyte, i.e. YSZ.), a HNS will be developed that is composed of numerous parallel interfaces between the two materials that can provide arranged vertical paths for ion diffusion through the entire electrolyte layer. Here, the Sr-doped $TiO_2$ material system is going to be first used as a potential material system,

analogous to SrTiO$_3$, for investigation of the effect of dopant content on the extent of interfacial mismatch and strain generated when combined with YSZ layer as a heterolayer.

## 7.2. Fabrication of YSZ/Sr-Doped TiO$_2$ Hetero-Nanostructures

Sr-doped TiO$_2$ nanotubes with different doping levels were used as the backbone layer for coating of YSZ. (The preparation of Sr-doped TiO$_2$ nanotubes was discussed in detail in chapter 5.) Using a lab-made (liquid-delivery) metal-organic chemical vapor deposition (LD-MOCVD) system, the nanotubes were coated with the YSZ as an ion-conductor phase to form the HNSs (for details about the method refer to section 3.12.1 in Chapter 3). A combination of set of parameters such as deposition temperature, carrier gas flow-rate, solution delivery pump speed (flow-rate) and the vacuum pressure (summarized in Table 7.1) controls the quality of the coating and the growth mechanism in the regime where it is more kinetically controlled and is ideal for the film formation. At low temperatures, low pressures, low concentration of reactants and high gas flow-rates, the surface kinetics control the reaction leading to formation of an oxide film that uniformly coats the grooves and corners of the substrate. By variation of the deposition parameters such as deposition flow rate, solution concentration and deposition time, the thickness of the coating can be controlled from a few nanometers to fully fill the nanotubes gaps that are estimated about 100 nm as shown in Figure 7.1.

Table 7.1 summarizes the CVD deposition parameters and the YSZ coating properties

| CVD parameters | $T_{sub}$ (°C) | Solution flow rate (ml/sec) | N$_2$ flow rate (sccm) | O$_2$ flow rate (sccm) | Y(TMHD) (mg) | Zr(TMHD) (mg) | Precursor (ml) |
|---|---|---|---|---|---|---|---|
| | 580 | 0.01 | 40 | 200 | 6 | 50 | 25 |
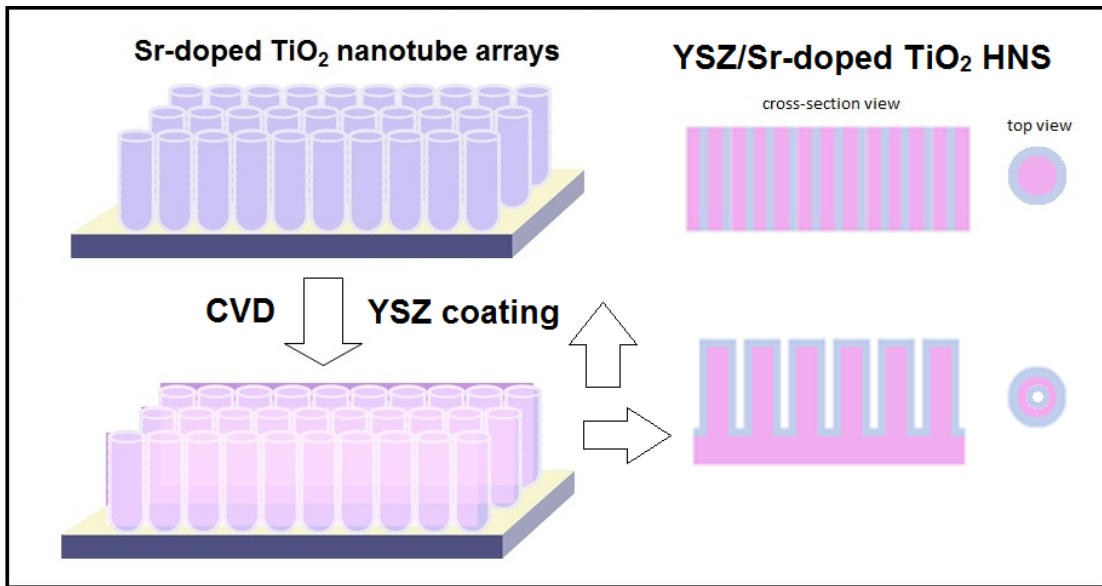


**Figure 7.1** Schematic illustrating CVD coating procedure for fabrication of Sr-doped TiO$_2$/YSZ nanotubular HNSs.

**7.2.1 Microstructure Growth and Characterization of YSZ/Sr-Doped TiO$_2$ HNSs**

Figure 7.2 (a) shows FESEM image of the annealed Sr-doped TiO$_2$ nanotubes before deposition (inset) and after deposition of YSZ. As seen in the SEM images, the

diameter of the uncoated nanotubes is ~ 100 nm and their wall thickness is ~ 5 nm. The inner and outer diameters of the original (uncoated) Sr-doped $TiO_2$ nanotubes have changed to smaller (~ 50 nm) and larger (~ 150 nm) values, respectively. Such changes in the inner and outer diameters of the nanotubes reveal that the coating has covered the walls of the nanotubes from inside and outside. The reproducibility of the fabrication of YSZ coating with the LD-MOCVD process was confirmed by performing the deposition on several nanotubes samples in a similar processing condition. The FESEM cross-sectional image of the sample (Figure 7.2 (b)) shows the full coverage of the nanotubes. From the EDS analysis, the chemical composition of the YSZ coating was obtained with the Y/Zr ratio of ~ 0.17 which revealed the composition of the coating is close to stoichiometric ratio (that was used in the precursor solution). Figure 7.2 (c) shows the schematic illustration of the conformal coating of YSZ on the nanotubes. As shown in this schematic, the nanotubes are composed of several rings that are arranges in top of each other to form the structure. In order to achieve a uniform coverage of the rings, the deposition was carried out at low pressure range (0.6-1 kPa), low solution concentration and at a low solution flow rate. However, at the same deposition temperature, increasing the solution concentration as well as its flow-rate was found to change the morphology of the coating from a uniform thin coating to a much coarser and a rough layer that results in non-uniformity of the final coating when full coverage of the nanotubes structure is desired [133].
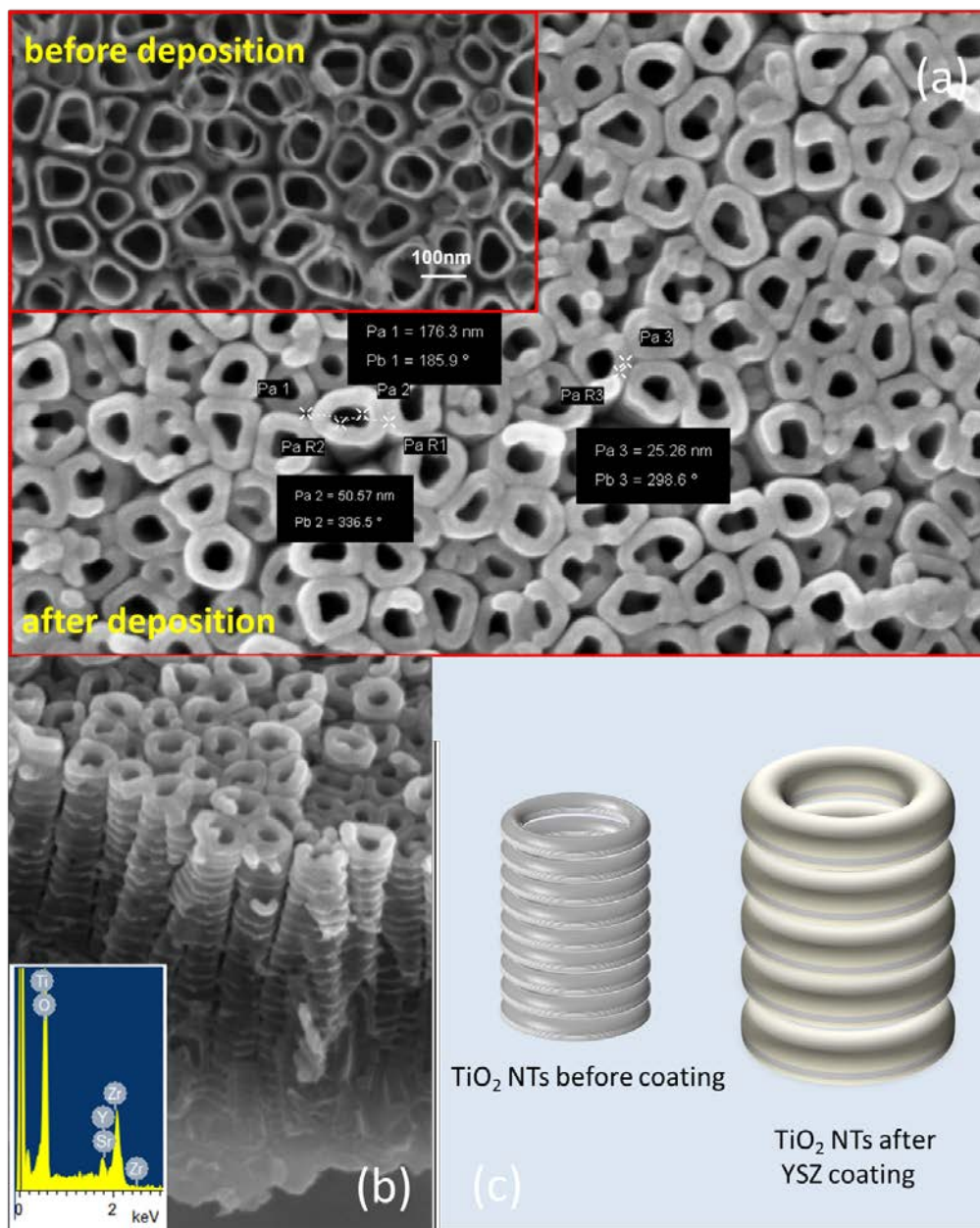
**Figure 7.2** (a) FESEM image of the annealed Sr-doped TiO$_2$ nanotubes before deposition (inset) and after deposition of YSZ. (b) Cross-section FESEM image and the corresponding EDS show the morphology of the nanotubes after coating and the chemical composition of YSZ coating. (c) Schematic illustration of the conformal YSZ coating around the rings as the component of the nanotubes structure.

In the CVD process, the deposition temperature is very critical parameter in determining the type of reactions. The substrate temperature is controlled using a very accurate temperature controller to hold the temperature in $\pm$ 1 °C range. In particular at the low temperature range, the growth rate is strongly temperature dependent and is driven by surface reactions such as heterogeneous nucleation and adsorption processes. The critical factor in all these growth kinetic studies is the growth rate. Typically, at deposition temperatures below 550 °C, the reaction in the MOCVD process is kinetically controlled; also, the process is entirely kinetically controlled at very low deposition pressure (<1 kPa), even though the deposition temperature is relatively high [134]. Based on the experimental conditions applied in this work, such as the deposition temperature (550-580 °C) and the deposition pressure (0.6-1 kPa), it was expected that the deposition is kinetically controlled. This was experimentally demonstrated by the conformal coverage of the nanotubes. In fact, if the CVD process was carried out at higher temperatures in a diffusion controlled regime, the openings of the nanotubes must have been immediately filled without any deposition on the inside and outside of the nanotubes. It is also known that the growth rate in the kinetically controlled surface reaction regime decreases with decreasing the deposition temperature [134, 135]. This is shown in the Arrhenius plot of the logarithm of growth rate vs. inverse deposition temperature in Figure 7.3. The growth rate is determined based on the overall change in thickness of the coating from inside and outside and is measured on the SEM image taken from the top surface of the nanotubes (Figure 7.2 (a)). The Arrhenius plot in Figure 7.3 indicates that the kinetically controlled deposition mechanism is operating within the range of deposition temperature.
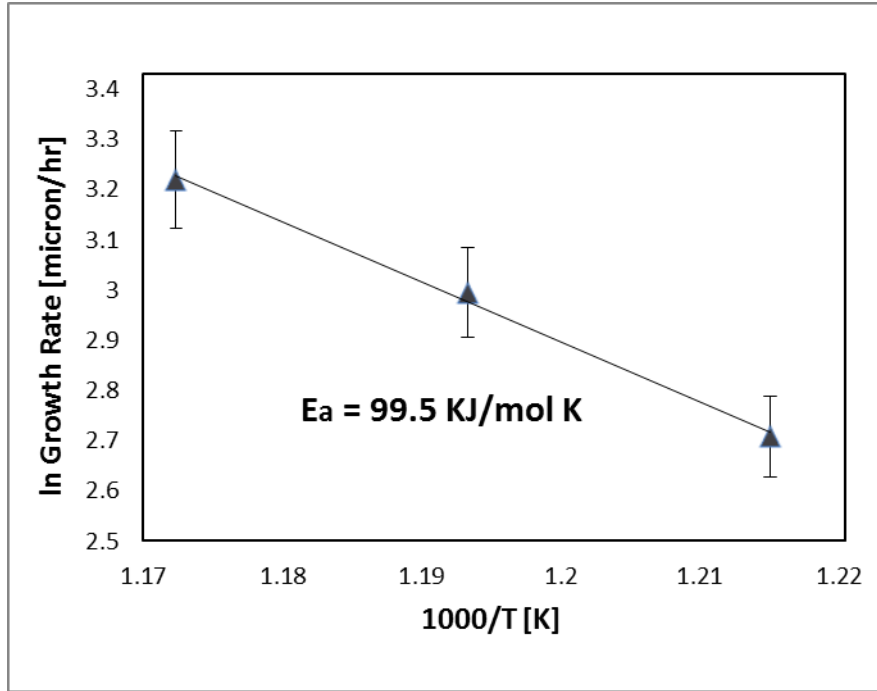
**Figure 7.3** Arrhenius plot of growth rate vs. temperature for precursor concentration of Y/Zr = 0.15 with observed activation energy of 99.5 ± 15 KJ mol$^{-1}$ K$^{-1}$.

The activation energy was determined from an Arrhenius plot of growth rate vs. inverse deposition temperature as in Eq. 7.1

$$GR(T_s) = A\exp(\frac{-E_a}{RT_s}) \qquad\qquad (7.1)$$

where GR is the film growth rate, $A$ is a constant, $R$ is the universal gas constant, $T_s$ is the substrate temperature, and $E_a$ is the activation energy. As seen in Figure 7.3, the activation energy calculated for the β-diketonate precursor used at the deposition reaction temperatures of 550 °C-580 °C was 99.5 ± 15 KJ mol$^{-1}$ K$^{-1}$. Krumdieck, et al. have reported the activation energy of 45 KJ mol$^{-1}$ K$^{-1}$ for YSZ films deposited using Zr(OC$_5$H$_{11}$)$_4$ precursor [135].

Furthermore, in a certain temperature range, where the evaporation characteristics of the precursor solution results in a satisfactory deposition, increasing metal–organic precursor concentration will result in higher growth rates. This effect is shown in FESEM images of Figure 7.4 in which partially coated to fully filled nanotubes of ~ 1 µm long were achieved by increasing the growth rate via increasing the solution concentration at 580 °C.
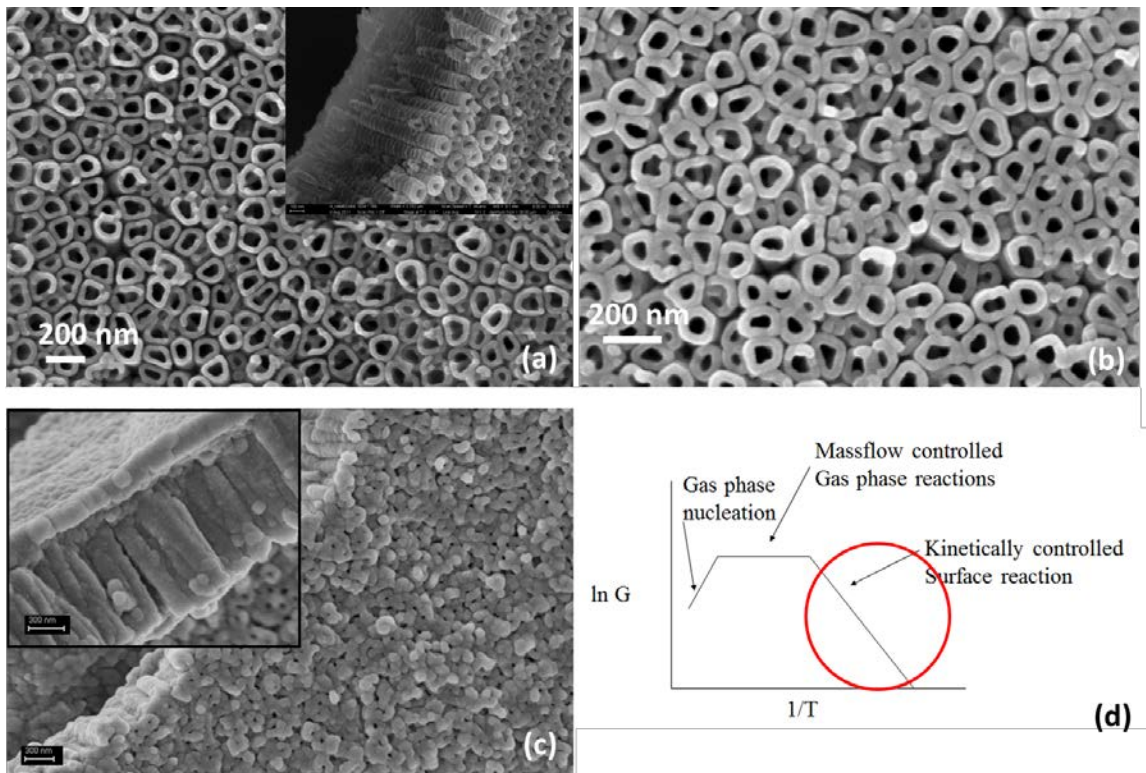


**Figure 7.4** Variation of coating thickness with precursor concentration (a) 20 min, (b) 30 min, (c) 60 min at deposition temperature of 580 °C.

Figure 7.5 shows the TEM image of a pair of YSZ coated Sr-doped TiO$_2$ nanotubes with the individual and combined EDS elemental color mapping obtained in scanning TEM mode wherein elements are distinguished by color: Ti (yellow), O (dark blue) and Zr (red). Note that the Zr map represents the YSZ coating and its fairly uniform spatial distribution along the nanotubes. As can be seen, YSZ layer has an approximate thickness of 10 nm and its distribution is mostly observed on the surface of the nanotubes.
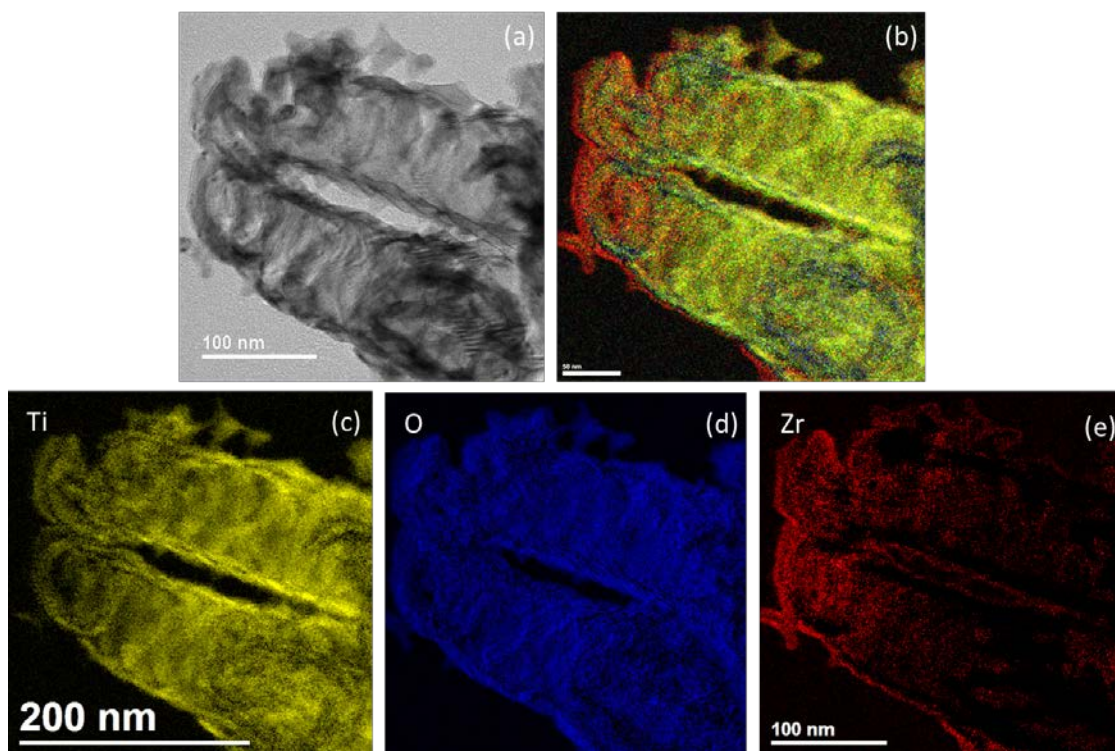


**Figure 7.5** (a) TEM image of a pair of YSZ coated Sr-doped TiO$_2$ nanotubes with the individual and combined EDS elemental color mapping: Ti (yellow), O (dark blue) and Zr (red) shown in (b-e).

**7.2.2 Thermal Stability of YSZ/Sr-Doped TiO$_2$ HNSs**

In order to study the thermal stability of the nanotubes, while annealing the coated nanotubes to crystallize the YSZ coatings, high-temperature glazing angle x-ray diffraction (HT-XRD) has been performed. It is known that annealing the TiO$_2$ nanotubes above ~ 650 °C results in conversion of the anatase to the rutile phase as well as partial destruction of the nanotubular structure. The same effect was observed in the structure of Sr-doped TiO$_2$ nanotubes annealed at 700 °C (which results in collapse of the nanotubes due to phase transformation, Figure 7.6 (a)). However, after coating of the nanotubes with YSZ, the structure of the nanotubes as the backbone remained unchanged after annealing at the same temperature, (i.e., 700 °C for 4 h, Figure 7.6 (b)). High temperature XRD (HTXRD) results also confirmed insignificant transformation of anatase to rutile phase in coated nanotubes. This observation reveals that the presence of YSZ coating around the nanotubes acts as a support and results in shifting of the anatase-to-rutile phase transformation temperature up to 700 °C and hence prevents the collapse of the nanotubes at up to this temperature (Figure 7.7 (a)).
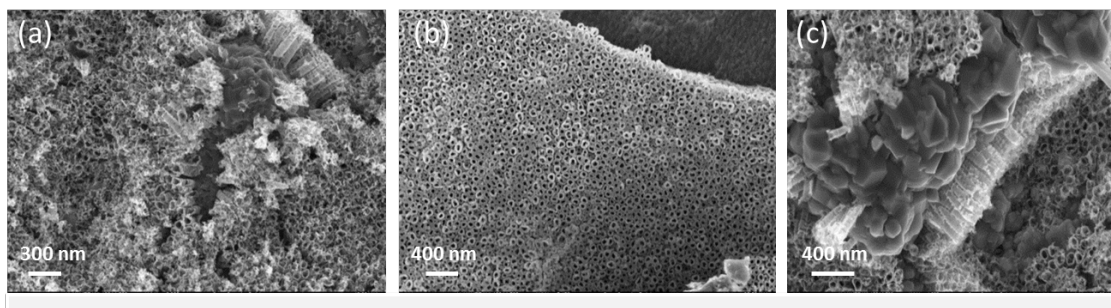
**Figure 7.6** FESEM images of (a) Sr-doped TiO$_2$ nanotubes annealed at 700 °C, (b) coated with YSZ and annealed at 700 °C and (c) coated with YSZ and annealed at 750 °C.

Results from the HTXRD analyses revealed improvement in the crystallinity of YSZ layer to cubic phase confirmed with (111) peak observed after heat treatment of the coated sample at 750 °C for 4 hours (Figure 7.7 (b)). However, characterization of the heat-treated samples showed that the supporting nanotubes are prone to some structural changes after increasing the annealing temperature from 700 °C to 750 °C under oxygen flow due to the phase transformation in the TiO$_2$ sacrificing layer underneath the nanotubes from anatase to rutile. Inspection of the phase-diagram of YSZ as a function of temperature (Figure 7.8) reveals that zirconia with less than 8 mol% Yttria forms the cubic YSZ phase above 1900-2700 °C, at equilibrium. At 750 °C, both cubic and tetragonal phases are retained at equilibrium. It is known that the maximum oxygen ionic conductivity can be obtained a at ~ 8.0 mol% Y$_2$O$_3$ with cubic phase. A lower absolute ionic conductivity is also found for the high density YSZ amorphous solid, relative to crystalline YSZ [136]. Thus, based on the information obtained from the phase-diagram, one can achieve the crystalline cubic phase at temperature range below 700 °C by

139

controlling the precise amount of $Y_2O_3$ dopant in the material. A new Y to Zr ratio (Y/Zr = 0.21) is therefore used in the precursor for deposition of YSZ on STO nanotube arrays in the following section.
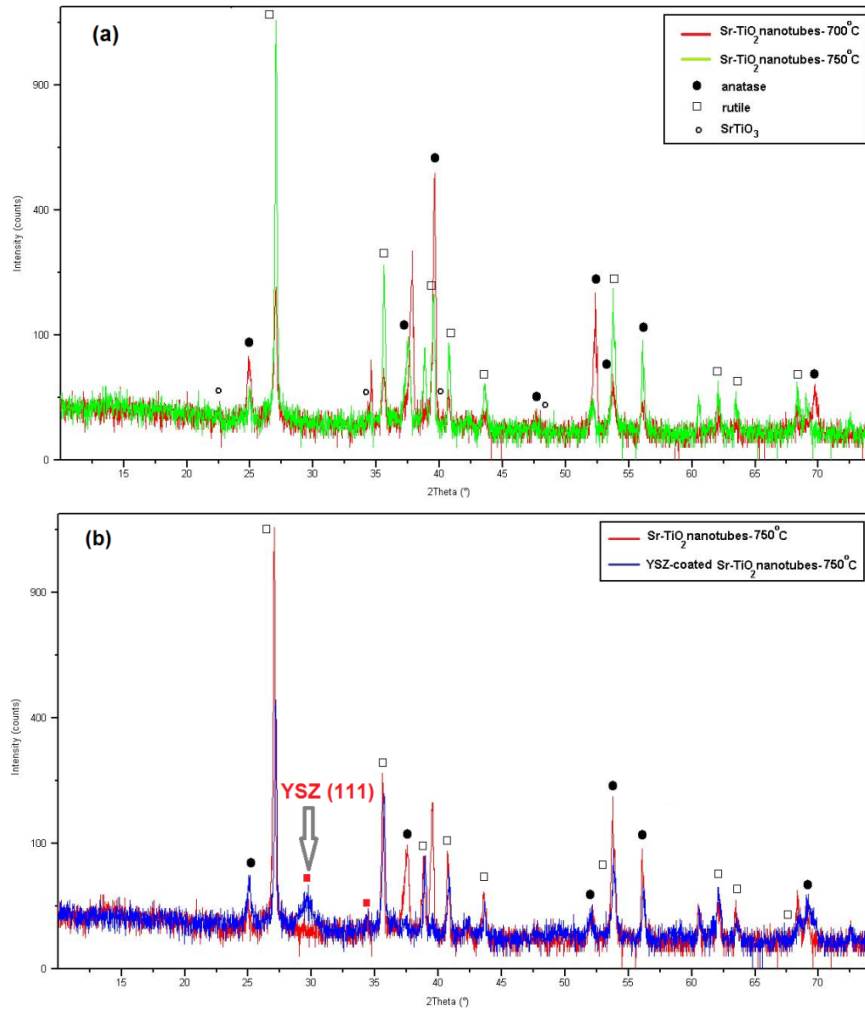


**Figure 7.7** HTXRD of (a) Sr-doped $TiO_2$ nanotubes annealed at 700 °C and 750 °C (b) Sr-doped $TiO_2$ nanotubes and YSZ coated Sr-doped $TiO_2$ nanotubes annealed at 750 °C.
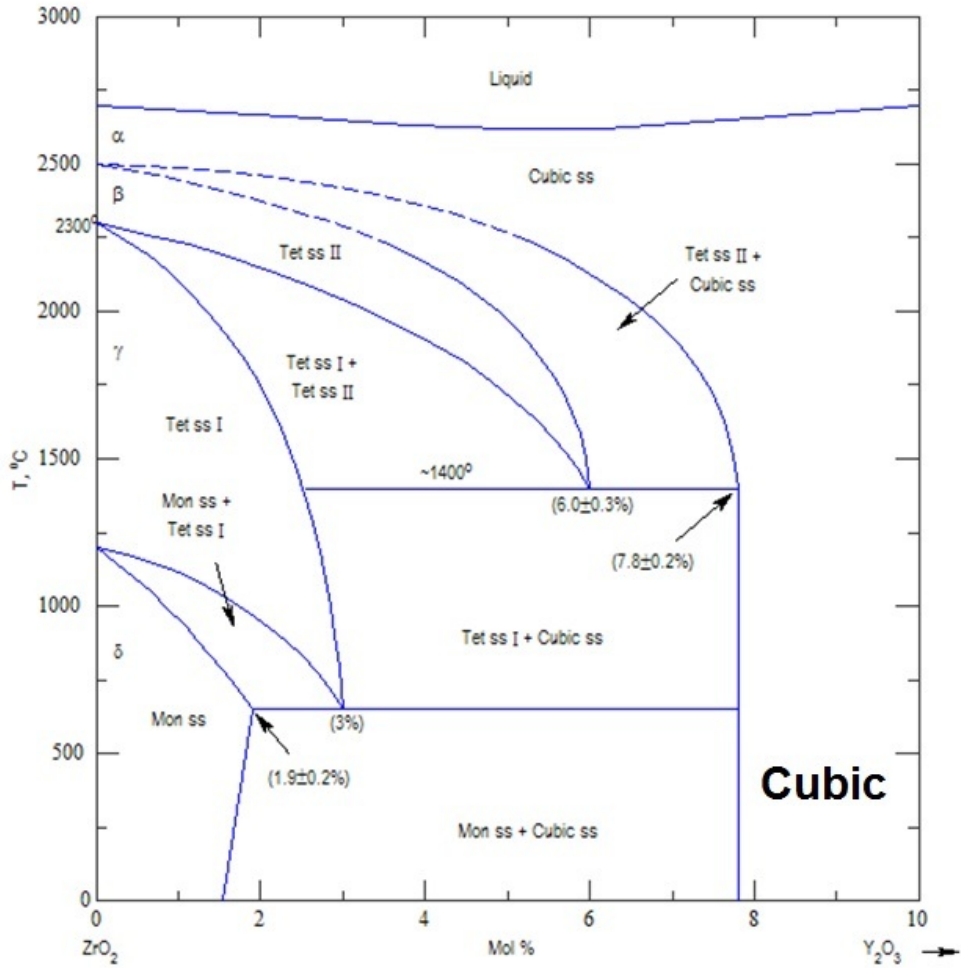
**Figure 7.8** Phase-diagram of YSZ as a function of temperature.

## 7.3. Fabrication of YSZ/STO Hetero-Nanostructures

As mentioned in previous chapters, multilayer systems have shown to enhance ionic conductivity due to spectacular behavior of the interfaces between two different ionic conductors [73]. In these systems, epitaxial thin layers of ionic conductors are grown on top of each other to make at most a few hundreds of nanometers think electrolyte layers. However, such systems are not a practically useful electrolyte system

for μ-SOFCs mainly due to processing factors such as the number of interfaces that is limited by manufacturing constraints in thin-film processing techniques. Thus, a new approach has been sought in this work which utilizes the geometric properties of nanotube arrays in design of new multilayered systems for electrolytes of μ-SOFCs. In this approach (see Figure 7.9), it is suggested that a vertically oriented nanotubes array of an of ionic/insulator can be coated from inside and outside walls with a second ionic oxide film to form a hetero-nanostructure with increased density of interfaces perpendicular to the surface of the electrolyte membrane that can enhance the transport of ionic species along the vertical direction from one side to the other. Such a system can be also considered as a viable architecture for other applications.
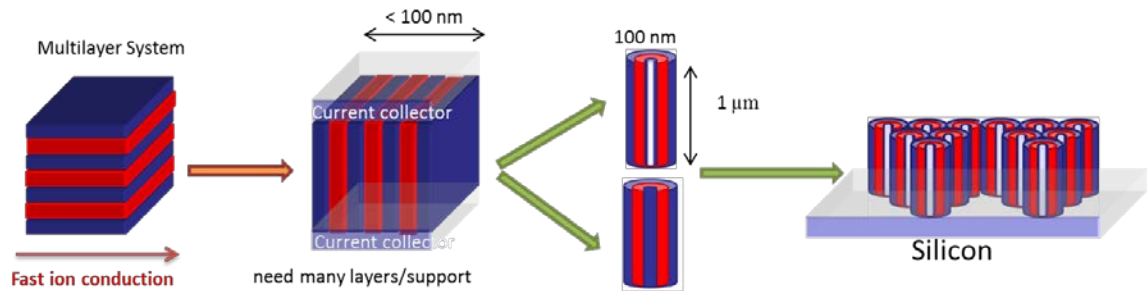


**Figure 7.9** Schematic of the designed hetero-nanostructure composed of an ionic conductor oxide coated on inside and outside walls of vertically oriented nanotube arrays of another ionic conductor.

To form the HNSs, the 5.5 μm STO NTAs with highest crystallinity fabricated on silicon substrate (as explained in chapter 6) were used as the backbone structure. Then, YSZ was deposited on the nanotubes using CVD method at 580 °C for 30 min with more

details explained in section 7.1. Figure 7.10 shows the top and cross section FESEM images of the YSZ coated STO nanotubes. The coating thickness can be tuned by the time of deposition. Therefore, the HNSs can be made in partially or fully coated membranes.
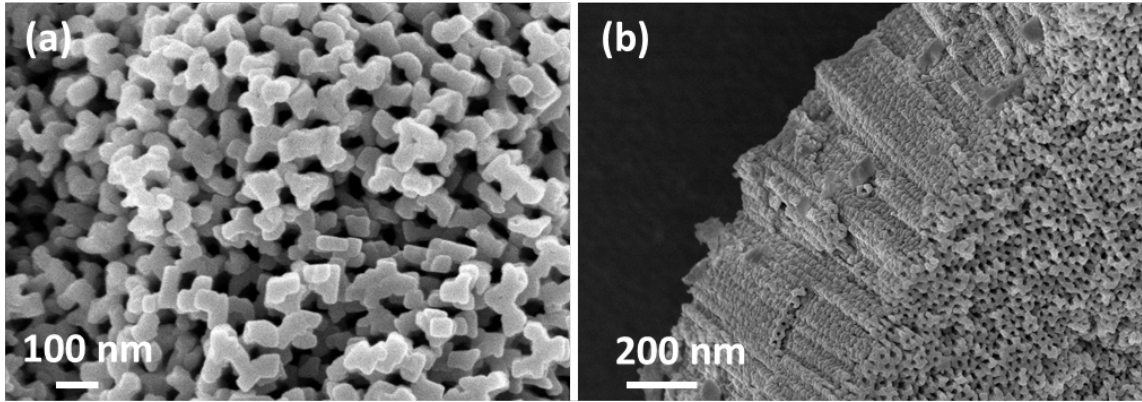


**Figure 7.10** Top and cross section FESEM images of the YSZ coated STO nanotubes prepared at 580 °C for 30 min.

From the SEM images, the average thickness of the walls was estimated ~ 50 nm. The cube-on cube morphology of the STO remained the same. However, the sharp edge of the cubes seems to be rounded. A HRTEM image from the surface of the YSZ coated STO NTAs is shown in Figure 7.11. The chemical composition of the composite is determined through EDS analysis in the TEM system which is shown in Figure 7.12. All elements present in the backbone material and the coating (such as Ti, Sr, Zr and Y) were detected by EDS. The ratio of Sr/Ti and Y/Zr were 0.8 and 0.21 which is close to the stoichiometric composition. As evident from the SAED pattern and HRTEM investigations, the STO backbone is composed of large square grains formed from

arrangement of oriented (110) planes. The smaller grains are also observed forming from arrangement of other planes such as (100) planes as evidenced from diffraction spots. Also, the arrangement of small grains of cubic YSZ at the outer layers with the highly crystalline large grains of cubic STO is clearly observed. There is no evidence of amorphous structure in the SAED pattern.  Thus, it was concluded that the as-deposited YSZ grows crystalline on the STO similar to PLD grown YSZ films on STO substrates. The crystallinity of the YSZ film is also confirmed by XRD analysis as shown in Figure 7.13.
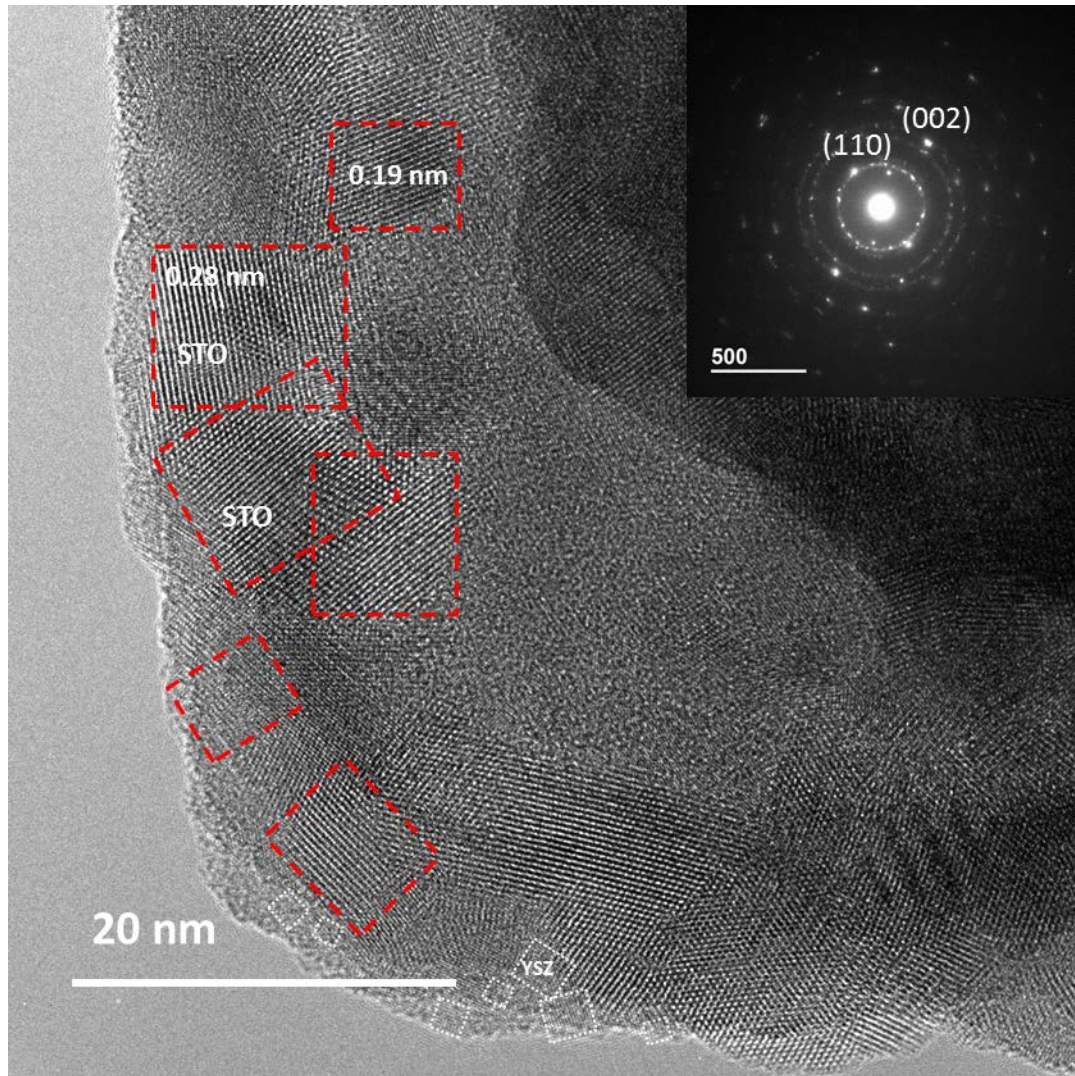
**Figure 7.11** HRTEM image and the SAED pattern in the inset from the top section of the YSZ coated STO NTAs showing arrangement of small grains of cubic YSZ at the outer layers on top of highly crystalline large grains of cubic STO.

| Elem | Weight % | Atomic % |
|------|----------|----------|
| O K  | 09.30    | 30.10    |
| ZrL  | 06.70    | 03.80    |
| TiK  | 33.60    | 36.40    |
| SrK  | 49.00    | 29.00    |
| Y K  | 01.40    | 00.80    |
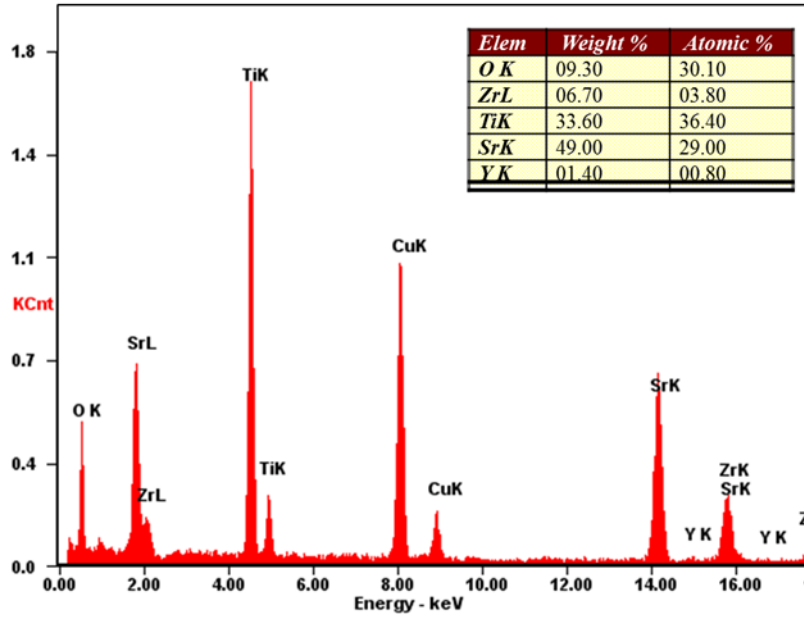
**Figure 7.12** EDS spectra taken from cross section of the YSZ/STO NTAs with the chemical composition shown in inset.
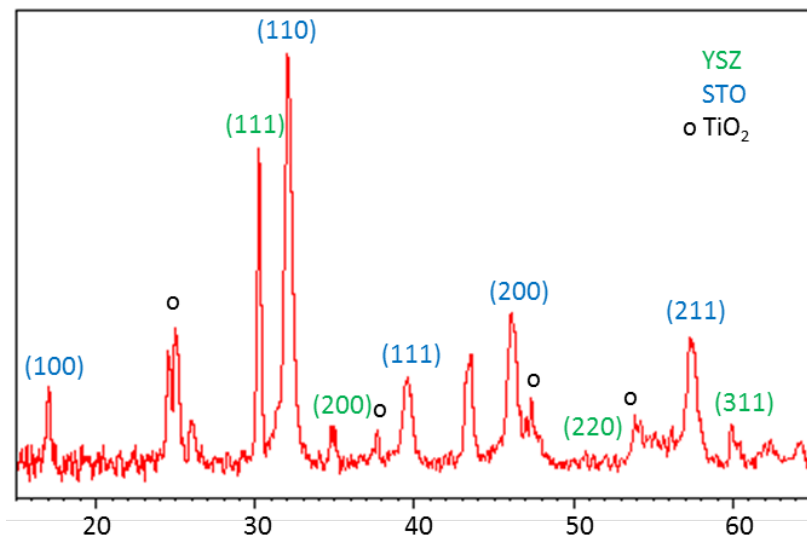


**Figure 7.13** XRD pattern of the STO and YSZ/STO NTAs.

146

Figure 7.14 shows the TEM image of a typical YSZ coated STO nanotube and the distribution of elements in the composite from EDS measurement. Inspecting the colored map, a sharp interface between the Zr coating (representing YSZ) and the STO backbone can be clearly observed. Moreover, conformal coating of the nanotube around its wall can be observed. From this observation, it appears that the coating has mostly covered the outer surface of the nanotubes rather than its inside. This can be related to the accessibility of the outer surface to the precursor gas in the CVD process. Furthermore, it can be seen that Ti is predominantly localized at the center part of the nanotube and its concentration decreases toward the outer wall of nanotube; whereas the Sr shows more homogeneous distribution over the entire structure. This is very well in accordance with the mechanism of phase transformation of $TiO_2$ to $SrTiO_3$ in which the diffusion of Sr ions into $TiO_2$ structure takes place mostly from the outer wall of the nanotube as explained earlier.
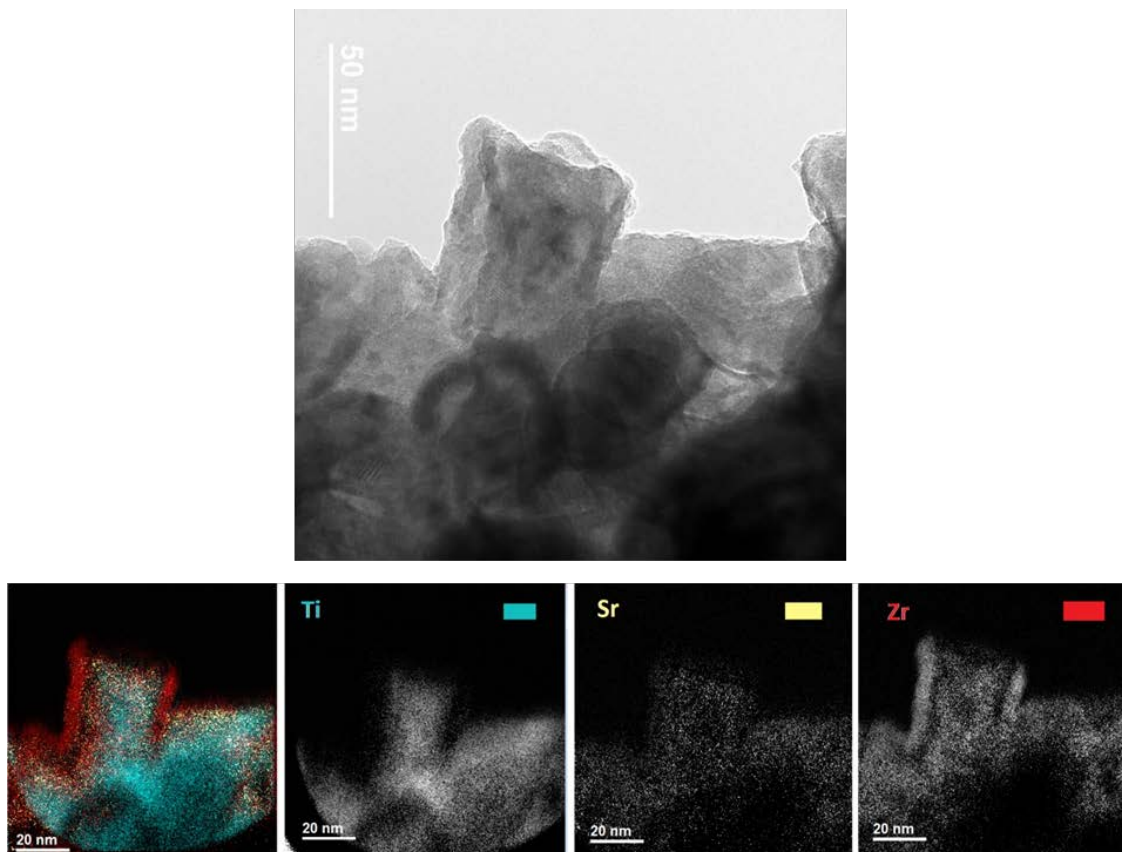
**Figure 7.14** TEM image of a YSZ coated STO nanotube with combined and individual EDS elemental color mapping for Ti (sky blue), Sr (light yellow) and Zr (red).

## 7.5. Conclusion

In this chapter, the coating process of the Sr-doped $TiO_2$ nanotubes and $SrTiO_3$ nanotubes is investigated. The fabrication, characterization and thermal stability of the composite YSZ/Sr-doped $TiO_2$ nanotubes are analyzed using different characterization techniques. The growth mechanism of the YSZ on Sr-doped $TiO_2$ nanotubes in the CVD process showed that in the deposition temperature range of 550 °C-580 °C the film growth mechanism follows the kinetically controlled regime, where the growth rate of the coating increases with increasing the deposition temperature. Post-annealing process of

the YSZ/coated Sr-doped TiO$_2$ nanotubes was shown to result in crystallinity of the film above 750 °C. It was also observed that the YSZ coating acts as a thermal barrier coating for Sr-doped TiO$_2$ nanotubes, thereby, improving the thermal stability of the Sr-doped TiO$_2$ nanotubes up to 700 °C. It was also found that by modification of the composition of the YSZ film to the higher Y doping level, cubic YSZ can be achieved at lower temperatures.

In the second part, YSZ/STO heteronanostructures were fabricated and characterized. It was found that the YSZ coating grows crystalline on the highly crystalline STO nanotube backbone. Consequently, this eliminates the need for post annealing step for crystallization of the coating and results in less complexities in the processing of the HNS on silicon and thermal stability issues that arise from phase transformation in the nanotubes as discussed earlier.

# CHAPTER 8

# CONCLUSION AND FUTURE WORK

## 8.1 Conclusion

This work has provided further knowledge about fundamental understanding of the growth, doping and coating mechanisms of the $TiO_2$ nanotubes structures on different substrates for energy conversion micro-devices. To this end, electrochemical growth mechanism of the $TiO_2$ nanotube arrays as well as the issues involved with their self-organization on silicon substrate via anodization has been highlighted. In addition, the growth of thin-film $TiO_2$ nanotube arrays on 3D isolated islands through the use of the FIB technique as a simple, high resolution and mask-less method for high aspect ratio etching for creation of isolated islands is demonstrated for the first time which shows great promise toward the use of the proposed approach for the development of other metal-oxide nanostructured devices and their integration with micro and nano-electromechanical systems.

The insight gained from the investigation of the doping effect on the structure of $TiO_2$ nanotubes has led to better understanding of the doping mechanism in terms of the role of dopant on the bulk and surface properties of the $TiO_2$ nanotubes with the following key outcomes:

- Up to the solubility limit of $Sr(OH)_2$, variation of the pH of the electrolyte and the doping content significantly influenced the length and quality of the doped nanotubes while the surface morphology remained intact.

Two major contributions were distinguished from the overall mechanism of Sr-doping into $TiO_2$ structure:

- Sr contribution to the bulk properties: at different dopant concentrations, the Sr-doping resulted in expansion of the tetragonal lattice of the $TiO_2$ anatase from XRD data. Additionally, the insertion of the dopant was found to change the oxidation states of Ti along the length of the nanotubes. No evidence of phase segregation was found along the tube axis.

- Sr contribution to the surface properties:

  - The NEXAFS surface analysis of the doped nanotubes confirmed no phase change (from anatase to rutile) due to insertion of the dopant. It also revealed that $Sr^{2+}$ doping only alters the Ti and O ions interaction in the $TiO_2$ lattice by modifying the surroundings of the Ti atoms on the surface and has no evident effect on their individual charge states as observed from the XPS study results. In addition, from NEXAFS experiments at different incident beam angles, a relation was obtained between the preferential crystal orientation in the highest doped nanotubes sample obtained from texture analysis of the bulk and the orientation of the octahedral units in the tetragonal lattice of anatase on the surface.

  - The combination of atomic-resolution Z-contrast imaging and EELS SI mapping also revealed possible phase segregation of SrO on the surface of the nanotubes at highest doping level. This is a key achievement toward understanding of the doping mechanism for similar materials in $TiO_2$

151

nanotube structure. Formation of heterointerfaces between the SrO and TiO$_2$ phases observed in the HRTEM analysis of Sr$^{2+}$-doped TiO$_2$ nanotubes can be also considered as a key factor in evaluation of the functionality of this material system for photocatalytic applications.

These results strongly suggest that the distribution of Sr dopant in TiO$_2$ nanotubes is sensitive to the dopant concentration as well as the growth conditions.

It was also revealed that Sr doping of TiO$_2$ nanotubes can red shift the absorption edge of the material to as long as 402 nm. The incorporation of the Sr in the TiO$_2$ lattice as well as the formation of Sr- rich TiO$_2$ clusters on the surface are suggested being the main factors contributing for the observed decrease in the bandgap and the enhancement in the photocatalytic activity.

The exploration of insertion of Sr atom into the TiO$_2$ nanotube structure is further investigated by processing of SrTiO$_3$ nanotube arrays (STO NTAs) using hydrothermal heat treatment with the following results:

- The as-synthesized STO NTAs were highly crystalline. Besides, the growth rate and morphology of STO NTAs were found to be dependent on the surface morphology of the stating TiO$_2$ nanotubes due to the nucleation starts from the exterior of the nanotube walls where surface morphology and crystal orientation of the planes play an important role in shaping the final morphology.

- The size of crystallites was found to change from ~20 nm at the early stages of the growth (nucleation) to as large as 100 nm cubes after completion of the crystallization and growth. This the critical point at which the cube size becomes

comparable to the size of the pores and as a result the nanotubular structure starts to alter into a porous structure.

In the last part, coating process of the doped $TiO_2$ nanotubes and $SrTiO_3$ nanotubes has been investigated. The fabrication, characterization and thermal stability of the composite YSZ/Sr-doped $TiO_2$ nanotubes were analyzed using different characterization techniques. The growth mechanism of the YSZ on Sr-doped $TiO_2$ nanotubes in the CVD process showed that in the deposition temperature range of 550°C - 580 °C the film growth rate follows the kinetically controlled regime, where the growth rate of the coating increases with increasing the deposition temperature. Post-annealing process of the YSZ/coated Sr-doped $TiO_2$ nanotubes was shown to result in crystallinity of the film above 750 °C. It was found that YSZ coating can improve the thermal stability of the Sr-doped $TiO_2$ nanotubes by shifting the anatase-to-rutile phase transformation temperature to 700 °C. It was also found that by modification of the composition of the YSZ film (> 8 % $Y_2O_3$ doping), cubic YSZ can be achieved at lower temperatures.

In the second part, YSZ/STO heteronanostructures were fabricated and characterized. It was found that the YSZ coating grows crystalline on the highly crystalline STO nanotube backbone. Consequently, this eliminates the need for post annealing step for crystallization of the coating and results in less complexities in the processing of the HNS on silicon and thermal stability issues that arise from phase transformation in the nanotubes as discussed earlier. The results from this part of the dissertation have paved the path for development and implementation of the coaxial nanotubular arrays as a new heterostructure composite architecture in many fields of application. In particular, such proposed platform can contribute in less-

expensive/practically productive construction of micro-SOFCs as well as other micro and nano-scale ionic devices.

## 8.2 Future Work

### 8.2.1 First Principle Study of the Structural stability and electronic Structure of Sr-Doped TiO$_2$

As mentioned in chapter 5, doping of TiO$_2$ nanotubes will result in modification of the electronic structure and thus the bandgap of the material. The results of this work were essentially obtained on a foundation of a comprehensive experimental investigation of the dopant atom and where it is mainly incorporated in the lattice structure of the anatase. However, in order to further strengthen the hypothesis, one needs to investigate theoretically the plausible sites of Sr atoms doped into anatase in more detail. As a preliminary work, it was proposed that the Sr (due to its large ionic radius) tends to go into interstitial sites rather than substitutional for the Ti or O atoms in the lattice structure. Moreover, the calculated lattice parameters of the supercells in the presence of Sr dopant were shown to be supporting the XRD data. However, more extensive theoretical analysis is required to obtain the favored structure in the presence of dopant and also gain more information about the density of states as well as the bandgap of the material.

### 8.2.2 Incident Photon to Charge Carrier Efficiency (IPCE) Measurements

The photoelectrochemical response of these Sr-doped TiO$_2$ electrodes needs to be evaluated in response to monochromatic light irradiation in terms of incident photon to charge carrier efficiency (IPCE). For this purpose, IPCE measurements need to be performed in order to find the band gap energy of the material as well as to proof the

charge separation in this structure. The results from these measurements will extend the fundamental evaluation of the efficiency of the material in terms of photon to charge carrier conversion.

### 8.2.3 Optimization of the YSZ/STO NTAs for Micro-SOFC Applications

The developed STO NTAs can be considered as a great candidate for being used as porous electrode of SOFCs mainly due to their potential applications as a sulfur tolerant anode material. Thus, the work should be expanded to take the advantage of such a porous nanostructure of STO NTAs with such well-defined defined non-tortuous paths for diffusion of hydrogen gas and charge species by doping this system with other transition metals, such as La and Y to enhance the electronic conductivity of the system. In another effort, the STO NTAs can be coated with nanoparticles of an ionic conductive material to for a 2D nanocomposite with a large area of heteronanostructures. Optimization of the fabricated YSZ/STO NTAs in this work would be essential for the use of this system as electrolyte of micro-SOFCs. Also, further attempts need to be made for development of a measurement setup designed for accurate evaluation of the electrical properties of such systems.

# APPENDIX A

# ENHANCED PHOTOELECTROCHEMICAL WATER OXIDATION CHARACTERISTICS OF SR-DOPED TIO$_2$ NANOTUBES

Photoelectrochemical measurements has been performed on Sr-doped TiO$_2$ nanotubes with different dopant level fabricated in this work for the purpose of using these nanostructures for water splitting applications. I was shown that Sr doping also improves the photoconversion efficiency of the nanotubes. The obtained photoconversion efficiency of Sr-doped nanotubes was shown to be about 0.69% which is by far among the highest reported values in the literature for TiO$_2$-based photoelectrochemical cells.

Figure A.1 shows the steady-state photocurrent density ($i_{ph}$) versus applied potential obtained for the Sr-doped TiO$_2$ nanotube samples fabricated in pH = 3 at various dopant concentration in 1.0 M KOH solution under AM1.5G (100 mW/cm$^2$) illumination. We chose the samples fabricated in solutions of pH = 3 because they showed higher dopant concentrations compared to those fabricated in solutions of pH = 2. It is observed that, in general, photocurrent increases with increasing the Sr-doping concentration. Note that the dark current in all cases is approximately 5 µA. The highest photocurrent ($\sim$ 1 mA/cm$^2$) obtained for the sample fabricated in electrolyte containing 0.06 M Sr(OH)$_2$ in the electrolyte with pH 3. This sample also shows the highest negative shift in the onset potential (-0.803 V). In fact, the trend observed in increasing the photocurrent with Sr dopant concentration is analogous to that of the absorption edge discussed earlier.

The corresponding light energy to chemical energy conversion (photoconversion) efficiency η was calculated using Eq. 1 [137]:

$\eta(\%) = [(total power output-electrical power input)/light power input] \times 100$

$$= j_p[(1.23 - |E_{measured} - E_{ocp}|)/I_0] \times 100 \qquad (1)$$

where $j_p$ is the photocurrent density (mWcm$^{-2}$), $E_{measured}$ is the electrode potential (versus Ag/AgCl) of the working electrode at which the photocurrent was measured under illumination. $E_{ocp}$ is the open circuit potential and $I_0$ is the intensity of the incident light (mWcm$^{-2}$). Figure A.2 shows the corresponding (three electrode) photo-conversion efficiency ($\eta$) the highest photo-conversion efficiency of 0.69% was recorded for sample with the highest concentration of Sr dopant, i.e 0.06 M in electrolyte with pH = 3. The enhancement in $\eta$ among all doped samples can be related to the difference in tube length. Longer NTs have larger surface areas enabling more light harvesting and larger active sites accessible to reactants in the aqueous environment. These factors lead to a higher efficiency which is strongly in agreement with the results of Sulaeman and co-workers where $i_{ph}$ activity under visible light irradiation is enhanced by designing strontium titanate with high Sr/Ti atomic ratio [138]. According to Liu and co-workers, the highest peak energy conversion efficiencies reported to date have been 0.60% or less over the whole solar spectrum [139]; thus, the obtained photoconversion efficiency of 0.69% for Sr-doped TiO$_2$ nanotubes in this work shows promising improvement towards a higher photoconversion efficiency.
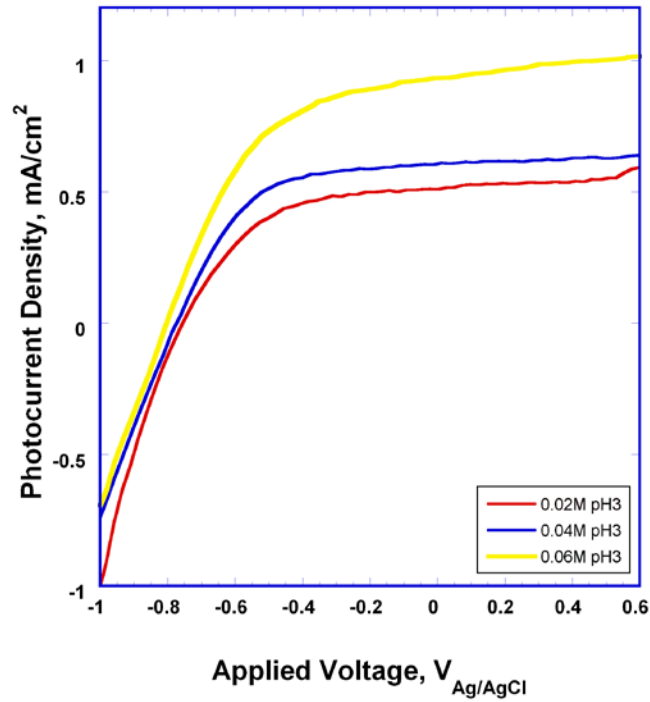
**Figure A.1** Variation of photocurrent obtained from the PEC cell measurement for S-doped $TiO_2$ nanotube electrodes at different Sr dopant concentration and @ pH = 3.
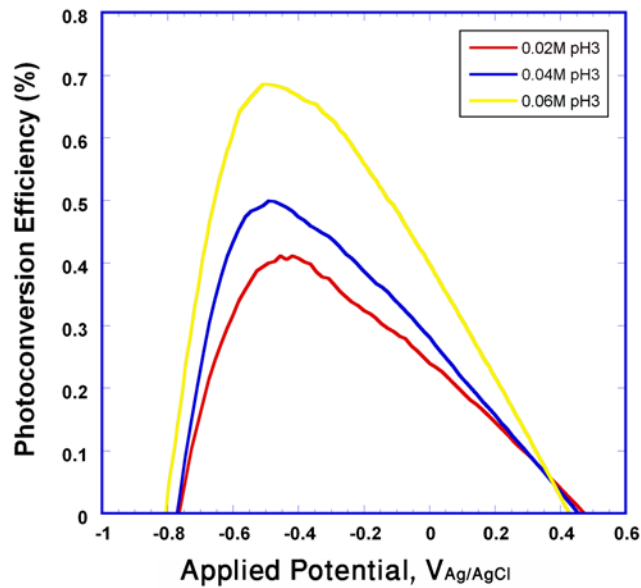


**Figure A.2** Photoconversion efficiency versus voltage characteristics for Sr-doped $TiO_2$ nanotube electrodes at different Sr dopant concentration and @ pH = 3.

# APPENDIX B

# XPS DATA ANALYSIS

The following plots show the details of XPS profile peak fitting for the undoped and Sr-doped TiO2 nanotube samples before and after heat treatment. The O 1s and the Ti with Ti 2p1/2 and Ti 2p1/2 photoemissions with the corresponding binding energies, area, full width at half maximum (FWHM) and the ratios are shown for each single peak next to the spectrum.
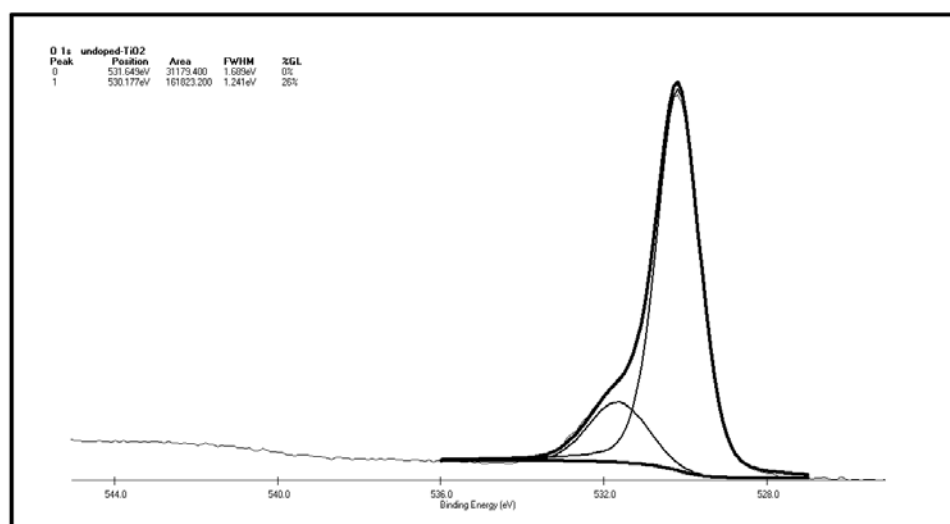


**Figure B.1** Peak fitting on XPS spectra for as-anodized (amorphous) TiO$_2$ nanotube sample showing O 1$s$.
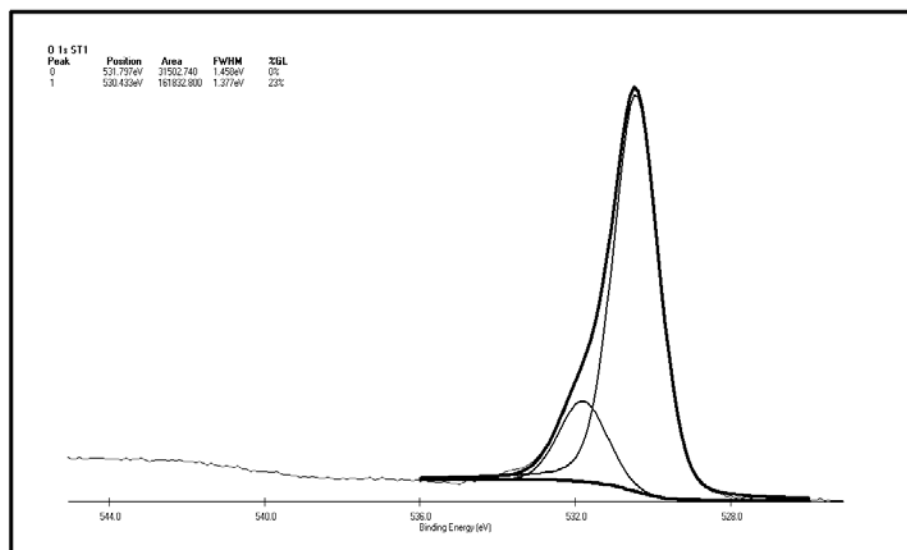
**Figure B.2** Peak fitting on XPS spectra for as-anodized (amorphous) ST1 sample showing O 1*s*.
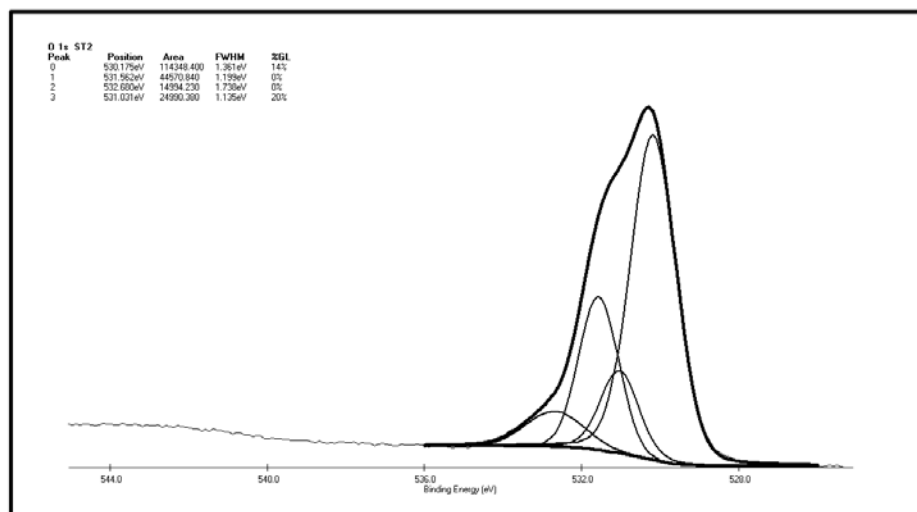


**Figure B.3** Peak fitting on XPS spectra for as-anodized (amorphous) ST2 sample showing O 1*s*.
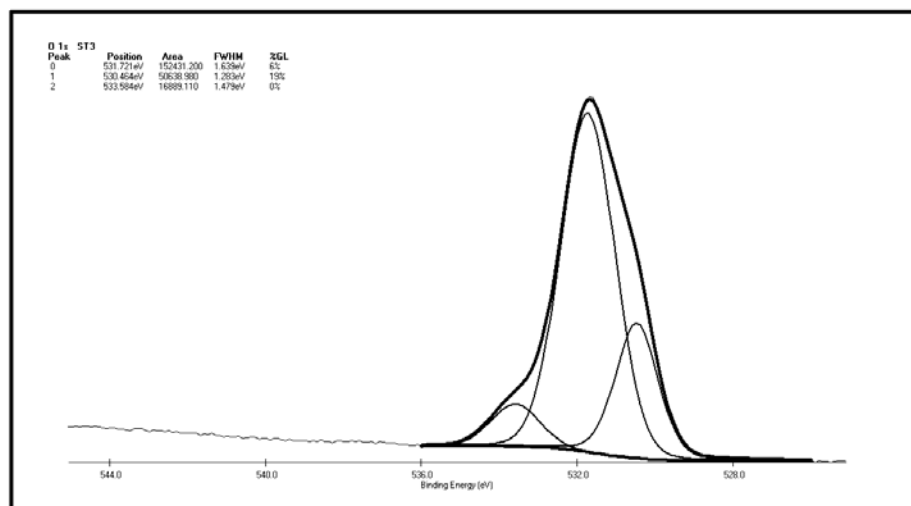
**Figure B.4** Peak fitting on XPS spectra for as-anodized (amorphous) ST3 sample showing O 1*s*.
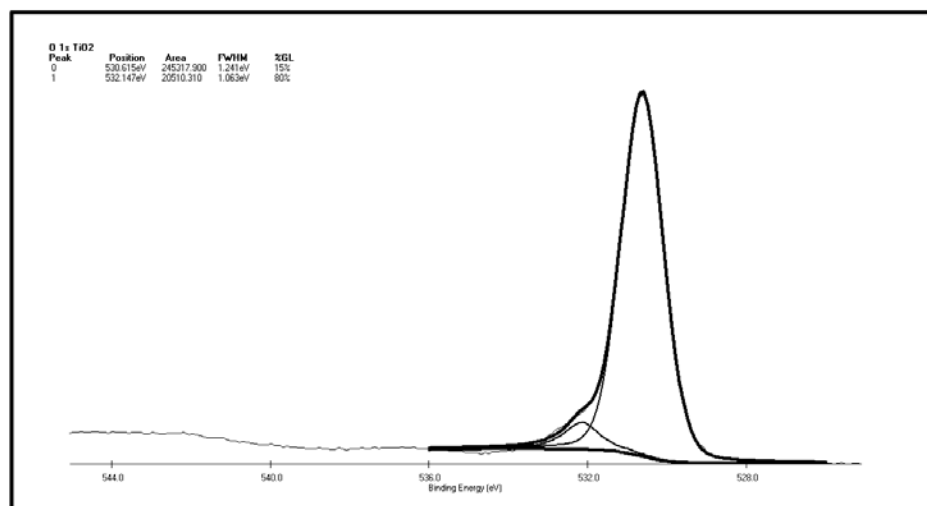


**Figure B.5** Peak fitting on XPS spectra for annealed (crystalline) $TiO_2$ nanotube sample showing O 1*s*.
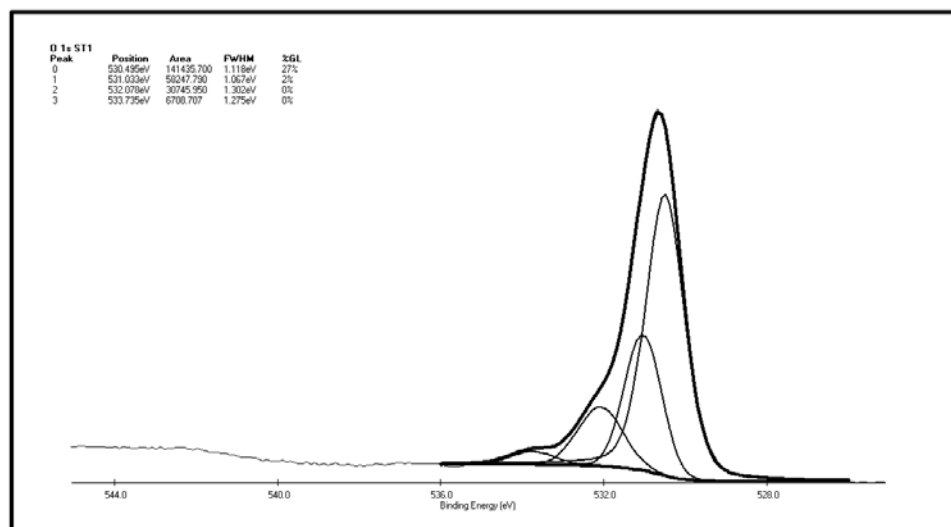
**Figure B.6** Peak fitting on XPS spectra for annealed (crystalline) ST1 sample showing O

1*s*.
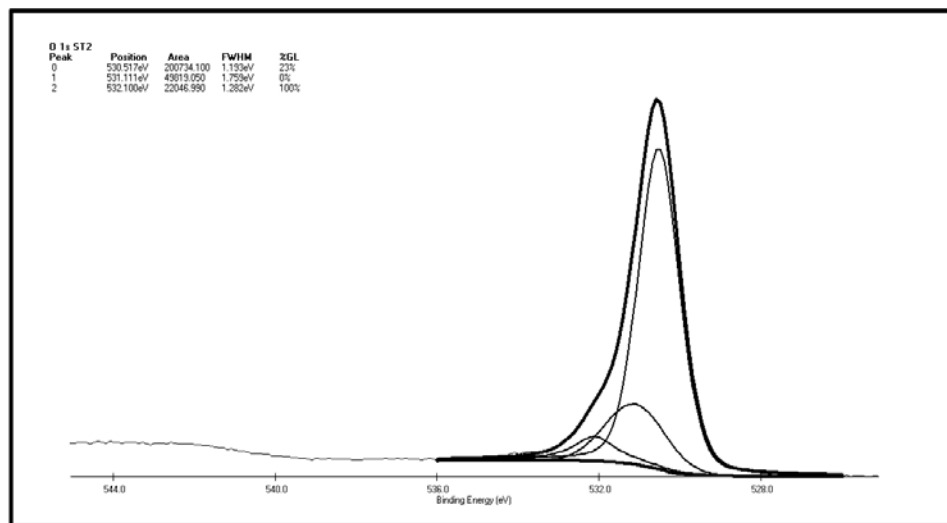


**Figure B.7** Peak fitting on XPS spectra for annealed (crystalline) ST2 sample showing O

1*s*.
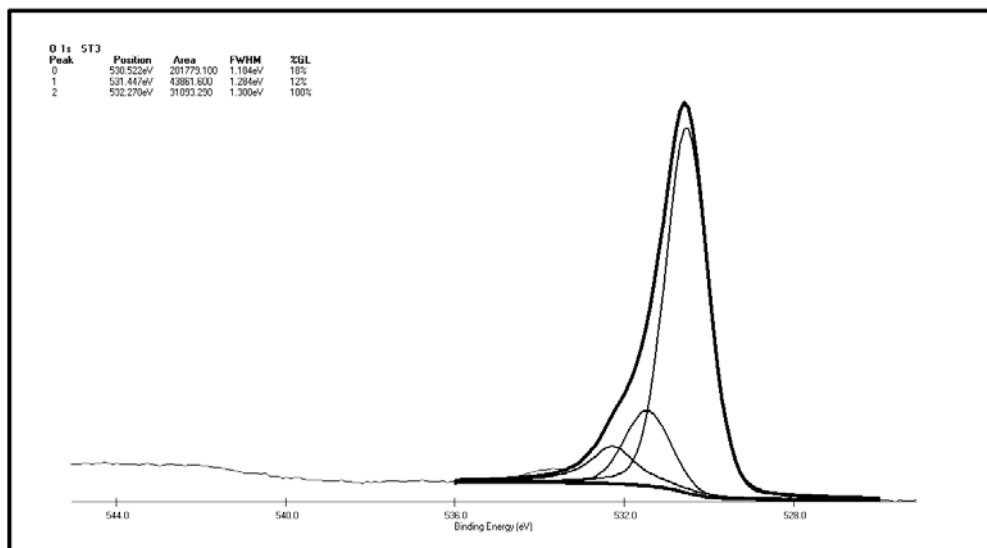
**Figure B.8** Peak fitting on XPS spectra for annealed (crystalline) ST3 sample showing O

1*s.*
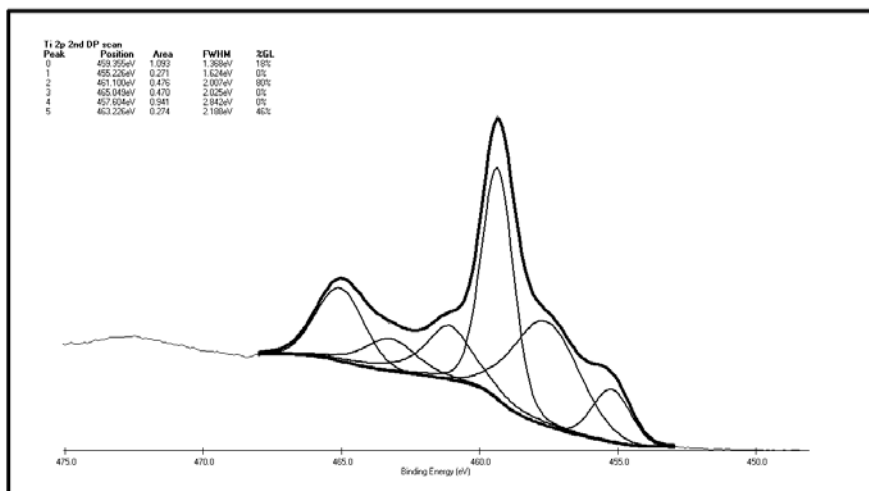


**Figure B.9** Peak fitting on XPS spectra for a typical annealed (crystalline) $Sr^{2+}$-doped

$TiO_2$ nanotubes (sample ST2) showing Ti 2*p* as a result of depth profiling.
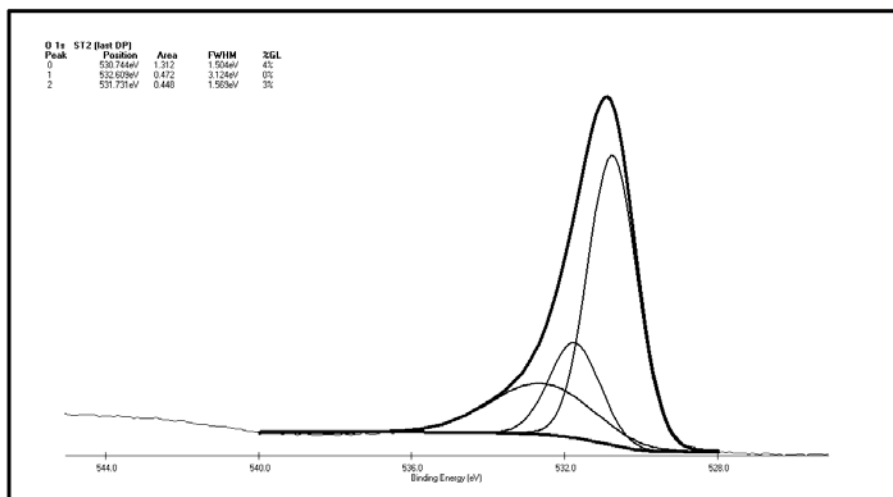
**Figure B.10** Peak fitting on XPS spectra for a typical annealed (crystalline) $Sr^{2+}$-doped

$TiO_2$ nanotubes (sample ST2) showing O 1*s* as a result of depth profiling.

# APPENDIX C

# EELS SPECTRA ANALYSIS

The low energy Sr $M_{4,5}$ -edges from EELS spectra has been used instead of taking high energy Sr $L_{2,3}$-edges at 1940 eV to identify the Sr in the nanoclusters. The reason for this is that the intensity of EELS signal drops substantially at high energy region. Therefore, to get sufficient signal at higher energy region, longer exposure may be needed. The lower energy Sr M-edge requires much shorter exposure time to get sufficient signal without damaging the sample.

In the various series (K, L, M, N, O) the edges show different profiles. They can be saw-tooth, delayed, white lines or mixture. It is known that $M_{4,5}$ -edges ($3d$ excitation) are typically rounded with delayed maxima. While, low energy M-edges such as the Sr $M_{4,5}$ -edges have large cross-sections for energy loss events, the delayed nature of the M edge results in poor signal-to-background ratios [140]. This is a result of the effective centrifugal barrier when the final states show a quantum number > 1. In the case of Mg, Al, Si, the $L_{2,3}$ -edge appears about 20 ev beyond the start of the ionization edge. Some elements' edges such as M-edges tend to appear as delayed signals even further away from the start of the ionization edge [141]. Two standard SrO spectra have been taken from Gatan's EELS atlas as the reference [142]. The first one shows the Sr $M_{4,5}$ -edge with a two humps around 160 eV and 190 eV and the second one after background subtraction [143] (Figure C.1). Here, the method of G.A. Botton [124] for extracting Sr M-edge map for standard $SrTiO_3$ has been used to extract the Sr M-edge map for doped

sample (Figure C.2). The obtained peak matches well with the Sr position edge and has become more pronounced after removing plural scattering.
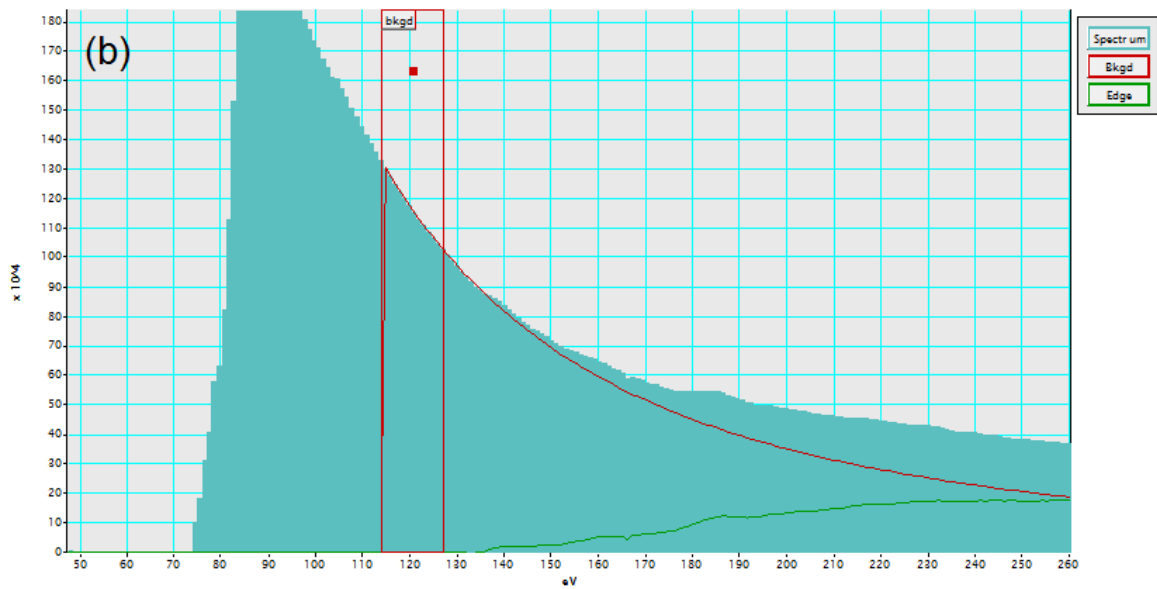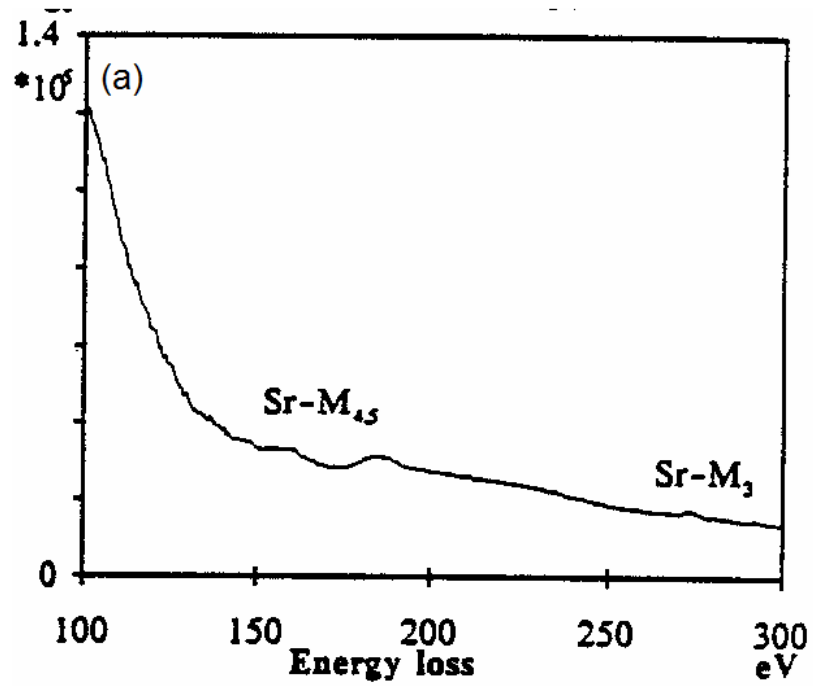
**Figure C.1** EELS spectra of Sr M-edges in (a) and (b) Sr M-edge with background subtraction [142, 143]. Reprinted with permission from EELS Atlas.
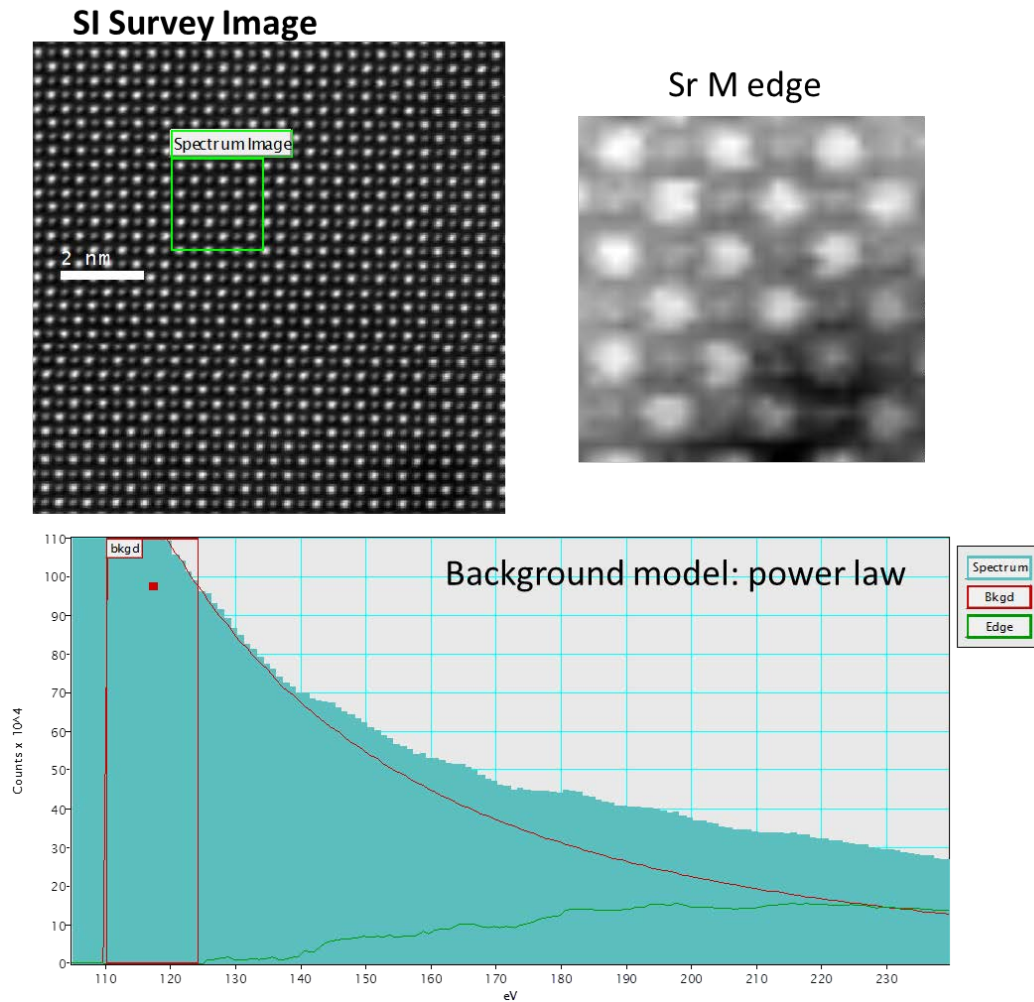


**Figure C.2** EELS spectrum of Sr M-edges [143]. Reprinted with permission from JEOL News.

Figures C.3 and C.4 show Z-contrast STEM images from the surface of a single $Sr^{2+}$-doped $TiO_2$ nanotube and the corresponding Sr M-edge EELS spectrum taken from

the selected region on the image and extracted by power-low background subtraction. The line map of Sr M-edge and the EELS-SI color map of Sr M-edge are also shown.
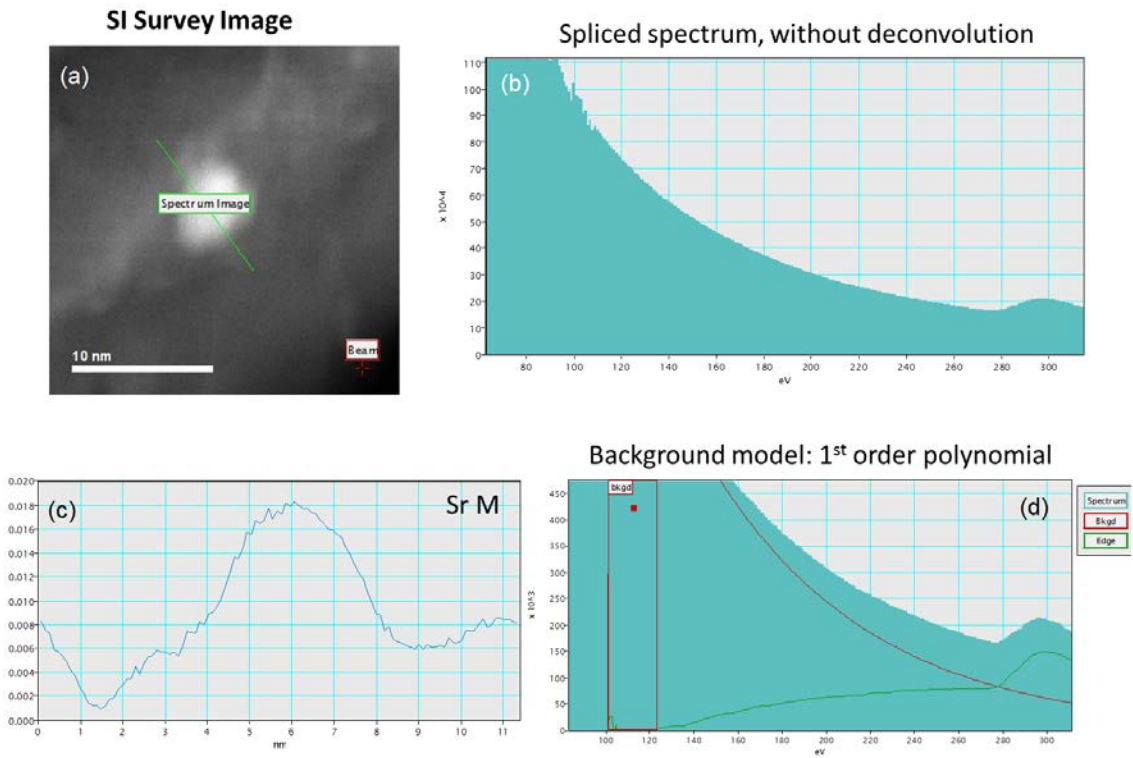


**Figure C.3** (a) Top view Z-contrast STEM image from the surface of $Sr^{2+}$-doped $TiO_2$ nanotube (sample ST3) and the corresponding Sr M-edge EELS spectrum taken from the line scan on the nanoparticle (c) line map of Sr M-edge and (d) Sr M-edge spectrum after background subtraction.
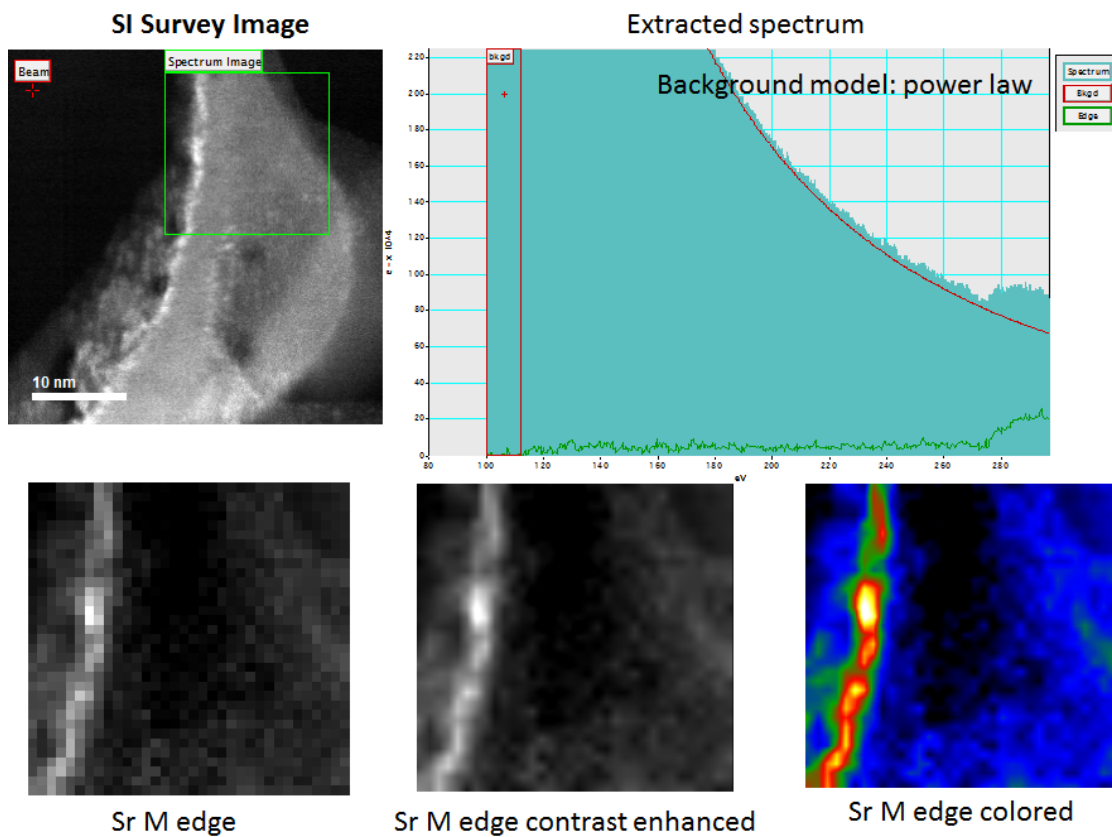
**Figure C.4** Top view Z-contrast STEM image from the surface of a single $Sr^{2+}$-doped $TiO_2$ nanotube and the corresponding Sr M-edge EELS spectrum taken from the selected region on the ring after background subtraction. The corresponding EELS-SI map of Sr M-edge is shown in color.

# REFERENCES

1.  Allam, N. K., An investigation into the doping and crystallinity of anodically fabricated $TiO_2$ nanotube arrays: Towards an efficient material for solar energy applications, in Department of Materials Science and Engineering2009, The Pennsylvania State University.

2.  Grimes, C. A.; O. K. Varghese and S. Ranjan, Light, Water, Hydrogen: The solar production of hydrogen by water photoelectrolysis. *Springer, Norwell, MA.*, **2007**,

3.  Khaselev, O. and J. A. Turner, A Monolithic Photovoltaic-Photoelectrochemical Device for Hydrogen Production via Water Splitting. *Science*, **1998**, *280*, 425-427.

4.  Hartmann, P.; D.-K. Lee; B. M. Smarsly and J. Janek, Mesoporous $TiO_2$: Comparison of Classical Sol-Gel and Nanoparticle Based Photoelectrodes for the Water Splitting Reaction. *ACS Nano*, **2010**, *4*, 3147-3154.

5.  Mor, G. K.; O. K. Varghese; M. Paulose; K. Shankar and C. A. Grimes, A review on highly ordered, vertically oriented $TiO_2$ nanotube arrays: Fabrication, material properties, and solar energy applications. *Solar Energy Materials and Solar Cells*, **2006**, *90*, 2011-2075.

6.  Stambouli, A. B. and E. Traversa, Solid oxide fuel cells (SOFCs): a review of an environmentally clean and efficient source of energy. *Renewable and Sustainable Energy Reviews*, **2002**, *6*, 433-455.

7.  Traversa, E., Toward the Miniaturization of Solid Oxide Fuel Cells. *The Electrochemical Society Interface* **2009**.

8.  Ruiz-Morales, J. C.; D. Marrero-Lopez; M. Galvez-Sanchez; J. Canales-Vazquez; C. Savaniu and S. N. Savvin, Engineering of materials for solid oxide fuel cells and other energy and environmental applications. *Energy & Environmental Science*, **2010**, *3*, 1670-1681.

9.  Gong, W.; S. Gopalan and U. B. Pal, Materials System for Intermediate-Temperature (600-800[degree]C) SOFCs Based on Doped Lanthanum-Gallate Electrolyte. *Journal of The Electrochemical Society*, **2005**, *152*, A1890-A1895.

10. Holme, T. P.; C. Lee and F. B. Prinz, Atomic layer deposition of LSM cathodes for solid oxide fuel cells. *Solid State Ionics*, **2008**, *179*, 1540-1544.

11. Liu, Y.; C. Compson and M. Liu, Nanostructured and functionally graded cathodes for intermediate temperature solid oxide fuel cells. *Journal of Power Sources*, **2004**, *138*, 194-198.

12. Shim, J. H.; C.-C. Chao; H. Huang and F. B. Prinz, Atomic Layer Deposition of Yttria-Stabilized Zirconia for Solid Oxide Fuel Cells. *Chemistry of Materials*, **2007**, *19*, 3850-3854.

13. Chao, C.-C.; C.-M. Hsu; Y. Cui and F. B. Prinz, Improved Solid Oxide Fuel Cell Performance with Nanostructured Electrolytes. *ACS Nano*, **2011**, *5*, 5692-5696.

14. Tsuchiya, M.; B.-K. Lai and S. Ramanathan, Scalable nanostructured membranes for solid-oxide fuel cells. *Nat Nano*, **2011**, *6*, 282-286.

15. Kuan-Lun, C.; S. Gold; V. Subramanian; L. Chang; M. A. Shannon and R. I. Masel, A nanoporous silicon membrane electrode assembly for on-chip micro fuel cell applications. *Microelectromechanical Systems, Journal of*, **2006**, *15*, 671-677.

16. Iijima, S., Helical microtubules of graphitic carbon. *Nature*, **1992**, *354*, 56-58.

17. Zhu, X.; Z. Liu and N. Ming, Perovskite oxide nanotubes: synthesis, structural characterization, properties and applications. *Journal of Materials Chemistry*, **2010**, *20*, 4015-4030.

18. Patzke, G. R.; F. Krumeich and R. Nesper, Oxidic Nanotubes and Nanorods–Anisotropic Modules for a Future Nanotechnology. *Angew. Chem. Int. Ed.*, **2002**, *41*, 2446-2461.

19. Bavykin, D. V. and F. C. Walsh, *Titanate and Titania Nanotubes: Synthesis, Properties and Applications*. 2009: RSC Nanoscience & Nanotechnology.

20. Zhao, J.; X. Wang; R. Xu; F. Meng; L. Guo and Y. Li, Fabrication of high aspect ratio zirconia nanotube arrays by anodization of zirconium foils. *Materials Letters* **2008**, *62* 4428–4430.

21. Yasir, M., Synthesis and Structural Characterization of Metal-Doped Titanate Nanotubes Using TEM, XRD and XAS, in Department of Synchrotron Instrumentation2011, Lund University Sweden.

22. Macak, J. M.; H. Tsuchiya; A. Ghicov; K. Yasuda; R. Hahn; S. Bauer and P. Schmuki, $TiO_2$ nanotubes: Self-organized electrochemical formation, properties and applications. *Current Opinion in Solid State and Materials Science*, **2007**, *11*, 3-18.

23. Currao, A., Photoelectrochemical Water Splitting *Chimia*, **2007**) *61*, 815–819.

24. Allam, N. K. and M. A. El-Sayed, Photoelectrochemical Water Oxidation Characteristics of Anodically Fabricated $TiO_2$ Nanotube Arrays: Structural and Optical Properties. *The Journal of Physical Chemistry C*, **2010**, *114*, 12024-12029.

25. Deng, L.; S. Wang; D. Liu; B. Zhu; W. Huang; S. Wu and S. Zhang, Synthesis, Characterization of Fe-doped TiO&lt;sub&gt;2&lt;/sub&gt; Nanotubes with High Photocatalytic Activity. *Catalysis Letters*, **2009**, *129*, 513-518.

26. Kapoor, P. N.; S. Uma; S. Rodriguez and K. J. Klabunde, Aerogel processing of $MTi_2O_5$ (M = Mg, Mn, Fe, Co, Zn, Sn) compositions using single source precursors: synthesis, characterization and photocatalytic behavior. *Journal of Molecular Catalysis A*, **2005**, *229*, 145–150.

27. Lu, N.; X. Quan; J. Li; S. Chen; H. Yu and G. Chen, Fabrication of Boron-Doped $TiO_2$ Nanotube Array Electrode and Investigation of Its Photoelectrochemical Capability. *The Journal of Physical Chemistry C*, **2007**, *111*, 11836-11842.

28. Park, J. H.; S. Kim and A. J. Bard, Novel Carbon-Doped $TiO_2$ Nanotube Arrays with High Aspect Ratios for Efficient Solar Water Splitting. *Nano Lett.*, **2006**, *6*, 25-28.

29. Tokudome, H. and M. Miyauchi, N-doped $TiO_2$ Nanotube with Visible Light Activity. *Chemistry Letters*, **2004**, *33*, 1108-1109.

30. Zhang, J.; C. Tang and J. H. Bang, $CdS/TiO_2$–$SrTiO_3$ heterostructure nanotube arrays for improved solar energy conversion efficiency. *Electrochemistry Communications* **2010**, *12*, 1124–1128.

31. Kumar, A.; P. G. Santangelo and N. S. Lewis, Electrolysis of Water at $SrTiO_3$, Photoelectrodes: Distlngulshlng between the Statistical and Stochastic Formalisms for Electron-Transfer Processes In Fuel-Formlng Photoelectrochemical Systems. *The Journal of Physical Chemistry*, **1992**, *96*, 834-842.

32. Liu, Y.; L. Xie; Y. Li; R. Yang; J. Qu; Y. Li and X. Li, Synthesis and high photocatalytic hydrogen production of $SrTiO_3$ nanoparticles from water splitting under UV irradiation. *Journal of Power Sources*, **2008**, *183*, 701-707.

33. Ueda, M. and S. Otsuka-Yao-Matsuo, Preparation of tabular $TiO_2$-$SrTiO_{3-\delta}$ composite for photocatalytic electrode. *Science and Technology of Advanced Materials*, **2003**, *5*, 187-193.

34. Zhang, J.; J. H. Bang; C. Tang and P. V. Kamat, Tailored $TiO_2$-$SrTiO_3$ Heterostructure Nanotube Arrays for Improved Photoelectrochemical Performance. *ACS Nano*, **2010**, *4*, 387-395.

35. Zhang, J.; C. Tang and J. H. Bang, $CdS/TiO_2$-$SrTiO_3$ heterostructure nanotube arrays for improved solar energy conversion efficiency. *Electrochemistry Communications*, **2010**, *12*, 1124-1128.

36. Zhang, X.; K. Huo; L. Hu; Z. Wu and P. K. Chuw, Synthesis and Photocatalytic Activity of Highly Ordered $TiO_2$ and $SrTiO_3/TiO_2$ Nanotube Arrays on Ti Substrates. *J. Am. Ceram. Soc.*, **2010**, *93*, 2771–2778.

37. Jitputti, J.; P. Charoensirithavorn and S. Yoshikawa, Hydrothermal Production of $SrTiO_3$ Nanotube Arrays. *Chemistry Letters* **2007**, *36*, 1508-1509.

38. Blennow, P.; K. K. Hansen; L. Reine Wallenberg and M. Mogensen, Effects of Sr/Ti-ratio in $SrTiO_3$-based SOFC anodes investigated by the use of cone-shaped electrodes. *Electrochimica Acta*, **2006**, *52*, 1651-1661.

39. Savaniu, C. D. and J. T. S. Irvine, La-doped $SrTiO_3$ as anode material for IT-SOFC. *Solid State Ionics*, **2011**, *192*, 491-493.

40. Kurokawa, H.; L. Yang; C. P. Jacobson; L. C. De Jonghe and S. J. Visco, Y-doped $SrTiO_3$ based sulfur tolerant anode for solid oxide fuel cells. *Journal of Power Sources*, **2007**, *164*, 510-518.

41. HARA, T.; T. ISHIGURO; N. WAKIYA and K. SHINOZAKI, Oxygen Sensing Properties of $SrTiO_3$ Thin Films. *Japanese Journal of Applied Physics*, **2008**, *47*, 7486–7489.

42. Hara, T. and T. Ishiguro, $SrTiO_3$-Based Microfabricated Oxygen Sensors. *Japanese Journal of Applied Physics* **2009**, *48*, 09KA17.

43. Voigts, F.; T. Damjanoví´c; G. u. Borchardt; C. Argirusis and WolfgangMaus-Friedrichs, Synthesis and Characterization of Strontium Titanate Nanoparticles as Potential High Temperature Oxygen Sensor Material. *Journal of Nanomaterials*, **2006**, *2006*, 1-6.

44. LEE, D. K.; I.-S. CHO; D. K. YIM; J.-H. NOH; K. S. HONG and D.-W. KIM, Synthesis and photoactivity of hetero-nanostructured $SrTiO_3$. *Journal of the Ceramic Society of Japan* **2010**, *118*, 876-880.

45. Chen, Y.-Y.; B.-Y. Yu; J.-H. Wang; R. E. Cochran and J.-J. Shyue, Template-Based Fabrication of $SrTiO_3$ and $BaTiO_3$ Nanotubes. *Inorganic Chemistry*, **2009**, *48*, 681–686.

46. Zhang, N.; J. Li; Z. He and K. Sun, Preparation and characterization of nano-tube and nano-rod structured $La0.8Sr_{0.2}MnO_{3-\delta}/Zr_{0.9}2Y_{0.08}O_2$ composite cathodes for solid oxide fuel cells. *Electrochemistry Communications*, **2011**, *13*, 570-573.

47. Zhang, J.; J. H. Bang; C. Tang and P. V. Kamat, Tailored $TiO_2$−$SrTiO_3$ Heterostructure Nanotube Arrays for Improved Photoelectrochemical Performance. *ACS Nano*, **2009**, *4*, 387-395.

48.    Xin, Y.; J. Jiang; K. Huo; T. Hu and P. K. Chu, Bioactive SrTiO$_3$ Nanotube Arrays: Strontium Delivery Platform on Ti-Based Osteoporotic Bone Implants. *ACS Nano*, **2009**, *3*, 3228-3234.

49.    Zhang, X.; K. Huo; L. Hu; Z. Wu and P. K. Chu, Synthesis and Photocatalytic Activity of Highly Ordered TiO$_2$ and SrTiO$_3$/TiO$_2$ Nanotube Arrays on Ti Substrates. *Journal of the American Ceramic Society*, **2010**, *93*, 2771-2778.

50.    Wong, S. and Y. Mao, Hydrothermal Synthesis of Perovskite Nanotubes, U.S. Patent, Editor 2006, The Research Foundation of State University of New York: United States.

51.    Alexandrov, V., Ab initio study of point defects in the bulk and on surfaces of an SrTiO$_3$ crystal, 2009, Max-Planck-Institut für Festkörperforschung, Stuttgart, Universität Stuttgart.

52.    Lu, H. F.; F. Li; G. Liu; Z.-G. Chen; D.-W. Wang; H.-T. Fang; G. Q. Lu; Z. H. Jiang and H.-M. Cheng, Amorphous TiO 2 nanotube arrays for low-temperature oxygen sensors. *Nanotechnology*, **2008**, *19*, 405504.

53.    Shankar, K.; J. I. Basham; N. K. Allam; O. K. Varghese; G. K. Mor; X. Feng; M. Paulose; J. A. Seabold; K.-S. Choi and C. A. Grimes, Recent Advances in the Use of TiO$_2$ Nanotube and Nanowire Arrays for Oxidative Photoelectrochemistry. *The Journal of Physical Chemistry C*, **2009**, *113*, 6327-6359.

54.    Su, X.; Q. Wu; X. Zhan; J. Wu; S. Wei and Z. Guo, Advanced titania nanostructures and composites for lithium ion battery. *J Mater Sci*, **2012**, *47*, 2519-2534.

55.    Rettew, R. E.; N. K. Allam and F. M. Alamgir, Interface Architecture Determined Electrocatalytic Activity of Pt on Vertically Oriented TiO$_2$ Nanotubes. *ACS Applied Materials & Interfaces*, **2011**, *3*, 147-151.

56.    Ortiz, G. F.; I. Hanzu; P. Knauth; P. Lavela; J. L. Tirado and T. Djenizian, TiO$_2$ nanotubes manufactured by anodization of Ti thin films for on-chip Li-ion 2D microbatteries. *Electrochimica Acta*, **2009**, *54*, 4262-4268.

57.    Varghese, O. K.; M. Paulose and C. A. Grimes, Long vertically aligned titania nanotubes on transparent conducting oxide for highly efficient solar cells. *Nat Nano*, **2009**, *4*, 592-597.

58.    Macak, J. M.; H. Tsuchiya; S. Berger; S. Bauer; S. Fujimoto and P. Schmuki, On wafer TiO$_2$ nanotube-layer formation by anodization of Ti-films on Si. *Chemical Physics Letters*, **2006**, *428*, 421-425.

59.    Roy, P.; S. Berger and P. Schmuki, TiO$_2$ Nanotubes: Synthesis and Applications. *Angewandte Chemie International Edition*, **2011**, *50*, 2904-2939.

60.    Hamedani, H. A.; N. K. Allam; H. Garmestani and M. A. El-Sayed, Electrochemical Fabrication of Strontium-Doped TiO$_2$ Nanotube Array Electrodes and Investigation of Their Photoelectrochemical Properties. *The Journal of Physical Chemistry C*, **2011**, *115*, 13480-13486.

61.    Allam, N. K.; F. Alamgir and M. A. El-Sayed, Enhanced Photoassisted Water Electrolysis Using Vertically Oriented Anodically Fabricated Ti−Nb−Zr−O Mixed Oxide Nanotube Arrays. *ACS Nano*, **2010**, *4*, 5819-5826.

62.    Tuller, H. L., Ionic Conduction and Applications, in Springer Handbook of Electronic and Photonic Materials2007, Springer-Verlag US.

63. Zha, S.; Y. Zhang and M. Liu, Functionally graded cathodes fabricated by sol-gel/slurry coating for honeycomb SOFCs. *Solid State Ionics*, **2005**, *176*, 25-31.

64. Vohs, J. M. and R. J. Gorte, High-Performance SOFC Cathodes Prepared by Infiltration. *Advanced Materials*, **2009**, *21*, 943-956.

65. Rivera-Calzada, A.; M. R. Diaz-Guillen; O. J. Dura; G. Sanchez-Santolino; T. J. Pennycook; R. Schmidt; F. Y. Bruno; J. Garcia-Barriocanal; Z. Sefrioui; N. M. Nemes; M. Garcia-Hernandez; M. Varela; C. Leon; S. T. Pantelides; S. J. Pennycook and J. Santamaria, Tailoring Interface Structure in Highly Strained YSZ/STO Heterostructures. *Advanced Materials*, **2011**, *23*, 5268-5274.

66. Jiang, Z.; C. Xia and F. Chen, Nano-structured composite cathodes for intermediate-temperature solid oxide fuel cells via an infiltration/impregnation technique. *Electrochimica Acta*, **2010**, *55*, 3595-3605.

67. Vohs, J. M. and R. J. Gorte, High-performance SOFC cathodes prepared by infiltration. *Advanced Materials*, **2009**, *21*, 943-956.

68. Bidrawn, F.; G. Kim; N. Aramrueang; J. M. Vohs and R. J. Gorte, Dopants to enhance SOFC cathodes based on Sr-doped $LaFeO_3$ and $LaMnO_3$. *Journal of Power Sources*, **2010**, *195*, 720-728.

69. Jiang, Z.; Z. Lei; B. Ding; C. Xia; F. Zhao and F. Chen, Electrochemical characteristics of solid oxide fuel cell cathodes prepared by infiltrating $(La,Sr)MnO_3$ nanoparticles into yttria-stabilized bismuth oxide backbones. *International Journal of Hydrogen Energy*, **2010**, *35*, 8322-8330.

70. Leng, Y. J.; S. H. Chan; K. A. Khor and S. P. Jiang, Performance evaluation of anode-supported solid oxide fuel cells with thin film YSZ electrolyte. *International Journal of Hydrogen Energy*, **2004**, *29*, 1025-1033.

71. Sata, N.; K. Eberman; K. Eberl and J. Maier, Mesoscopic fast ion conduction in nanometre-scale planar heterostructures. *Nature*, **2000**, *408*, 946-949.

72. Azad, S.; O. A. Marina; C. M. Wang; L. Saraf; V. Shutthanandan; D. E. McCready; A. El-Azab; J. E. Jaffe; M. H. Engelhard; C. H. F. Peden and S. Thevuthasan, Nanoscale effects on ion conductance of layer-by-layer structures of gadolinia-doped ceria and zirconia. *Applied Physics Letters*, **2005**, *86*, 131906.

73. Garcia-Barriocanal, J.; A. Rivera-Calzada; M. Varela; Z. Sefrioui; E. Iborra; C. Leon; S. J. Pennycook and J. Santamaria, Colossal Ionic Conductivity at Interfaces of Epitaxial $ZrO_2$:$Y2O_3$/$SrTiO_3$ Heterostructures. *Science*, **2008**, *321*,

74. Pennycook, T. J.; M. J. Beck; K. Varga; M. Varela; S. J. Pennycook and S. T. Pantelides, Origin of Colossal Ionic Conductivity in Oxide Multilayers: Interface Induced Sublattice Disorder. *Physical Review Letters*, **2010**, *104*, 115901.

75. Zhang, C.; J. Grandner; R. Liu; S. B. Lee and B. W. Eichhorn, Heterogeneous films of ordered $CeO_2$/Ni concentric nanostructures for fuel cell applicationsw. *Phys. Chem. Chem. Phys*, **2010**, *12*, 4295–4300

76. Bellino, M. n. G.; J. n. G. Sacanell; D. G. Lamas; A. G. Leyva and N. E. Walsoe de Reca, High-Performance Solid-Oxide Fuel Cell Cathodes Based on Cobaltite Nanotubes. *Journal of the American Chemical Society*, **2007**, *129*, 3066-3067.

77. Bellino, M. G.; J. G. Sacanell; D. G. Lamas; A. G. Leyva and D. R. N. E. Walsoe, High-performance solid-oxide fuel cell cathodes based on cobaltite nanotubes. *Journal of the American Chemical Society*, **2007**, *129*, 3066-3067.

78.     Zhang, D.; C. Pan; L. Shi; L. Huang; J. Fang and H. Fu, A highly reactive catalyst for CO oxidation: $CeO_2$ nanotubes synthesized using carbon nanotubes as removable templates. *Microporous and Mesoporous Materials*, **2009**, *117*, 193-200.

79.     Pinedo, R.; I. Ruiz de Larramendi; D. Jimenez de Aberasturi; I. Gil de Muro; J. I. Ruiz de Larramendi; M. I. Arriortua and T. Rojo, Synthesis of highly ordered three-dimensional nanostructures and the influence of the temperature on their application as solid oxide fuel cells cathodes. *Journal of Power Sources*, **2011**, *196*, 4174-4180.

80.     Hibino, T.; A. Hashimoto; T. Inoue; J.-i. Tokuno; S.-i. Yoshida and M. Sano, Single-Chamber Solid Oxide Fuel Cells at Intermediate Temperatures with Various Hydrocarbon-Air Mixtures. *Journal of The Electrochemical Society*, **2000**, *147*, 2888-2892.

81.     Sacanell, J.; A. G. Leyva; M. G. Bellino and D. G. Lamas, Nanotubes of rare earth cobalt oxides for cathodes of intermediate-temperature solid oxide fuel cells. *Journal of Power Sources*, **2010**, *195*, 1786-1792.

82.     Chappanda, K. N.; Y. R. Smith; M. Misra and S. K. Mohanty, Site-specific and patterned growth of TiO 2 nanotube arrays from e-beam evaporated thin titanium film on Si wafer. *Nanotechnology*, **2012**, *23*, 385601.

83.     Masuda, Y.; S. Ieda and K. Koumoto, Site-Selective Deposition of Anatase $TiO_2$ in an Aqueous Solution Using a Seed Layer. *Langmuir*, **2003**, *19*, 4415-4419.

84.     Lai, Y.; J. Huang; J. Gong; Y. Huang; C. Wang; Z. Chen and C. Lin, Superhydrophilic-Superhydrophobic Template: A Simple Approach to Micro- and Nanostructure Patterning of $TiO_2$ Films. *J. Electrochem. Soc.* , **2009**, *156*, D480-D484.

85.     Pittrof, A.; S. Bauer and P. Schmuki, Micropatterned $TiO_2$ nanotube surfaces for site-selective nucleation of hydroxyapatite from simulated body fluid. *Acta Biomaterialia*, **2011**, *7*, 424-431.

86.     Arshak, K.; M. Mihov; A. Arshak; D. McDonagh and D. Sutton. Focused ion beam lithography-overview and new approaches. in *Microelectronics, 2004. 24th International Conference on*. 2004.

87.     Lai, Y.; L. Lin; F. Pan; J. Huang; R. Song; Y. Huang; C. Lin; H. Fuchs and L. Chi, Bioinspired Patterning with Extreme Wettability Contrast on $TiO_2$ Nanotube Array Surface: A Versatile Platform for Biomedical Applications. *Small*, **2013**, 1-9.

88.     Yongqi Fu, N. K. A. B., Focused ion beam direct fabrication of microoptical elements: features compared with laser beam and electron beam direct writing, in Innovation in Manufacturing Systems and Technology (IMST)2004.

89.     Chen, B.; K. Lu and J. A. Geldmeier, Highly ordered titania nanotube arrays with square, triangular, and sunflower structures. *Chemical Communications*, **2011**, *47*, 10085-10087.

90.     Chen, B. and K. Lu, Selective Focused-ion-beam Sculpting of $TiO_2$ Nanotubes and Mechanism Understanding. *Physical Chemistry Chemical Physics*, **2012**, 1854-1862.

91.     Chen, B.; K. Lu and Z. Tian, Effects of titania nanotube distance and arrangement during focused ion beam guided anodization. *Journal of Materials Chemistry*, **2011**, *21*, 8835-8840.

92.     Berger, S.; R. Hahn; P. Roy and P. Schmuki, Self-organized $TiO_2$ nanotubes: Factors affecting their morphology and properties. *physica status solidi (b)*, **2010**, *247*, 2424-2435.

93.     Ghicov, A. and P. Schmuki, Self-ordering electrochemistry: a review on growth and functionality of $TiO_2$ nanotubes and other self-aligned $MO_x$ structures. *Chemical Communications*, **2009**, *0*, 2791-2808.

94.     Yasuda, K.; A. Ghicov; T. Nohiraa; N. Kani; R. Hagiwara and P. Schmuki, Preparation of Organized Ti Nanorods by Successive Electrochemical Processes in Aqueous Solution and Molten Salt. *Electrochem. Solid-State Lett.*, **2008**, *11*, C51-C54.

95.     Bauer, S.; S. Kleber and P. Schmuki, $TiO_2$ nanotubes: Tailoring the geometry in $H_3PO_4$/HF electrolytes. *Electrochemistry Communications*, **2006**, *8*, 1321-1325.

96.     Roy, P.; S. Berger and P. Schmuki, $TiO_2$ Nanotubes: Synthesis and Applications. *Angew. Chem. Int. Ed.*, **2011**, *50*, 2904–2939.

97.     Masahashi, N.; S. Semboshi; N. Ohtsu and M. Oku, Microstructure and superhydrophilicity of anodic $TiO_2$ films on pure titanium. *Thin Solid Films*, **2008**, *516*, 7488–7496.

98.     Kim, G.-S.; S. G. Ansari; H.-K. Seo; Y.-S. Kim and H.-S. Shin, Effect of annealing temperature on structural and bonded states of titanate nanotube films. *J. Appl. Phys.*, **2007**, *101*, 024314- 024320.

99.     Lee, C. C.; G. Proust; G. Alici; G. M. Spinks and J. M. Cairney, Three-dimensional nanofabrication of polystyrene by focused ion beam. *Journal of Microscopy*, **2012**, *248*, 129-139.

100.    Tipler, P. A. and G. Mosca, *Physics for Scientists and Engineers: Electricity and Magnetism, Light, Modern Physics*. 5th ed. Vol. 2. 2003: Susan Finnermore Brennan.

101.    Kumar, S. G. and L. G. Devi, Review on Modified $TiO_2$ Photocatalysis under UV/Visible Light: Selected Results and Related Mechanisms on Interfacial Charge Carrier Transfer Dynamics. *The Journal of Physical Chemistry A*, **2011**, *115*, 13211-13241.

102.    Chiodo, L.; J. M. Garc´ıa-Lastra; D. J. Mowbray; A. Iacomino and A. Rubio, Tailoring electronic and optical properties of $TiO_2$: nanostructuring, doping and molecular-oxide interactions, 2010.

103.    Zounani, A.; D. Zambon and J. C. Cousseins, Optical properties of $Eu^{3+}$ activated $Sr_{10}F_2(PO_4)_6$ elaborated by coprecipitation. *Journal of Alloys and Compounds*, **1992**), *188*, 82-86.

104.    Ernst, E., Hydrothermal Conversion of Diatom Frustules Into Barium Titanate Based Replicas, 2007, Georgia Institute of Technology.

105.    Hengerer, R.; B. Bolliger; M. Erbudak and M. Grätzel, Structure and stability of the anatase $TiO_2$ (101) and (001) surfaces. *Surface Science*, **2000**, *460*, 162-169.

106.    Campos, M. F. d.; J. C. Damasceno; R. Machado and C. A. Achete, Ucertainty Estimation of Lattice Parameters Measured by X-Ray Diffraction in XVIII IMEKO WORLD CONGRESS Metrology for a Sustainable Development

2006: Rio de Janeiro, Brazil.

107. Wang, Q., Grain Boundary Segregation and Blocking Effect in Doped Titanium Oxide at High Temperature Equilibrium, in Materials Science and Engineering2008, The Pennsylvania State University.

108. Atanacio, A. J.; T. Bak and J. Nowotny, Effect of Indium Segregation on the Surface versus Bulk Chemistry for Indium-Doped $TiO_2$. *ACS Applied Materials & Interfaces*, **2012**, *4*, 6626-6634.

109. Ikeda, J. A. S. and Y.-M. Chiang, Space Charge Segregation at Grain Boundaries in Titanium Dioxide: I, Relationship between Lattice Defect Chemistry and Space Charge Potential. *Journal of the American Ceramic Society*, **1993**, *76*, 2437-2446.

110. Ikeda, J. A. S.; Y.-M. Chiang; A. J. Garratt-Reed and J. B. V. Sande, Space Charge Segregation at Grain Boundaries in Titanium Dioxide: II, Model Experiments. *Journal of the American Ceramic Society*, **1993**, *76*, 2447-2459.

111. LING, H. C. and M. F. YAN, Second phase development in Sr-doped $TiO_2$. *JOURNAL OF MATERIALS SCIENCE*, **1983**, *18*, 2688-2696.

112. Mete, E.; D. Uner; O. Gülseren and Ş. Ellialtıoğlu, Pt-incorporated anatase $TiO\_\{2\}(001)$ surface for solar cell applications: First-principles density functional theory calculations. *Physical Review B*, **2009**, *79*, 125418.

113. Steveson, M.; T. Bredowy and A. R. Gerson, MSINDO quantum chemical modelling study of the structure of aluminium-doped anatase and rutile titanium dioxide. *Journal of Molecular Modeling*, **2012**, *18*, 358-365.

114. SHANNON, R. D. and C. T. PREWITT, Effective ionic radii in oxides and fluorides. *Acta Crystallog.*, **1969**, *B25*, 925-946.

115. Gallay, R.; J. J. van der Klink and J. Moser, EPR study of vanadium (4+) in the anatase and rutile phases of $TiO_2$. *Physical Review B*, **1986**, *34*, 3060-3068.

116. Gesenhues, U. and T. Rentschler, Crystal Growth and Defect Structure of $Al^{3+}$-Doped Rutile. *Journal of Solid State Chemistry*, **1999**, *143*, 210–218.

117. Kröger, F. and H. Vink, Relations between the concentrations of imperfections in crystalline solids. *Solid state physics*, **1956**, *3*, 307-435.

118. Chen, T.-j. and P. Shen, Defect Clustering and Ordering in Zn-Doped $TiO_2$ upon Solution Annealing. *J. Phys. Chem. C*, **113**, *2009*, 328–332.

119. Baer, D. R.; M. H. Engelhard; A. S. Lea; P. Nachimuthu; T. C. Droubay; B. L. J. Kim; C. Mathews; R. L. Opila; L. V. Saraf; W. F. Stickle; R. M. Wallace and B. S. Wright, Comparison of the sputter rates of oxide films relative to the sputter rate of $SiO_2$. *J. Vac. Sci. Technol. A*, **2010**, *28*, 1060.

120. Stohr, J., *NEXAFS Spectroscopy*. 1992: Springer.

121. Guttmann, P.; C. Bittencourt; X. Ke; G. V. Tendeloo; D. A. P. Umek4; C. P. Ewels; S. Rehbein; S. Heim and G. Schneider1. TXM-NEXAFS of $TiO_2$-Based Nanostructures

Location: . in *THE 10TH INTERNATIONAL CONFERENCE ON X-RAY MICROSCOPY* 2010. Chicago, Illinois, (USA)

122. Bittencourt, C.; A. Felten; X. Gillon; J. J. Pireaux; E. Najafi; A. P. Hitchcock; X. Ke; G. Tendeloo; C. P. Ewels; P. Umek and D. Arcon, STXM-NEXAFS of individual titanate-based nanoribbon, in EMC 2008 14th European Microscopy Congress 1–5 September 2008, Aachen, Germany, M. Luysberg, K. Tillmann, and T. Weirich, Editors. 2008, Springer Berlin Heidelberg. p. 693-694.

123. Zhou, J. G.; H. T. Fang; J. M. Maley; M. W. Murphy; J. Y. P. Ko; J. N. Cutler; R. Sammynaiken; T. K. Sham; M. Liu and F. Li, Electronic structure of $TiO_2$ nanotube arrays from X-ray absorption near edge structure studies. *J. Mater. Chem.*, **2009**, *19*, 6804–6809.

124. Botton, G. A.; S. Lazar and C. Dwyer, *Ultramicroscopy*, **2010**, *110*, 926-934.

125. Chen, J.-G.; C.-Y. Chen; C.-G. Wu; C.-Y. Lin; Y.-H. Lai; C.-C. Wang; H.-W. Chen; R. Vittal and K.-C. Ho, An efficient flexible dye -sensitized solar cell with a photoanode consisting of $TiO_2$ nanoparticle -filled and SrO-coated $TiO_2$ nanotube arrays†. *J. Mater. Chem.*, **2010**, *20*, 7201-7207.

126. Miao, L.; S. Tanemura; H. Watanabe; Y. Mori; K. Kaneko and S. Toh, The improvement of optical reactivity for $TiO_2$ thin films by N2–H2 plasma surface-treatment. *Journal of Crystal Growth*, **2004**, *260*, 118-124.

127. Yang, J.; Baoyou Geng; Y. Ye and X. Yu, Stick-like titania precursor route to $MTiO_3$ (M = Sr, Ba, and Ca) polyhedra. *CrystEngComm*, **2012**, *14*, 2959.

128. Scherrer, P., Bestimmung der Grösse und der inneren Struktur von Kolloidteilchen mittels Röntgenstrahlen. *Nachr. Ges. Wiss. Göttingen*, **1918**, *26*, 98-100.

129. Šetinc, T.; M. Spreitzer; D. Vengust; I. Jerman and D. Suvorov, Inherent defects in sol-precipitation/hydrothermally derived $SrTiO_3$ nanopowders. *Ceramics International*.

130. Moon, J.; J. A. Kerchner; H. Krarup and J. H. Adair, Hydrothermal synthesis of ferroelectric perovskites from chemically modified titanium isopropoxide and acetate salts. *J. Mater. Res.*, **1999**, *14*,

131. Cheng, H. and A. Selloni, Hydroxide Ions at the Water/Anatase $TiO_2(101)$ Interface: Structure and Electronic States from First Principles Molecular Dynamics. *Langmuir*, **2010**, *26*, 11518-11525.

132. Zˇagar, K.; A. Recˇnik; P. M. Ajayan and M. Cˇeh, Oriented cube-on-cube nanocrystal assembly of $SrTiO_3$ tubules. *Nanotechnology*, **2010**, *21*, 375605-337612.

133. Krumdiecka, S. P.; O. Sbaizeroa; A. Bullerta and R. Raj, YSZ layers by pulsed-MOCVD on solid oxide fuel cell electrodes. *Surface and Coatings Technology* **2003**, *167*, 226–233.

134. Choy, K. L., Chemical vapour deposition of coatings. *Progress in Materials Science*, **2003**, *48*, 57–170.

135. Krumdieck, S. P.; O. Sbaizero; A. Bullert and R. Raj, YSZ layers by pulsed-MOCVD on solid oxide fuel cell electrodes. *Surface and Coatings Technology*, **2003**, *167*, 226-233.

136. Lau, K. C. and B. I. Dunlap, Molecular dynamics simulation of yttria-stabilized zirconia (YSZ) crystalline and amorphous solids. *J. Phys.: Condens. Matter* **2011** *23*, 16.

137. Allam, N. K.; F. Alamgir and M. A. El-Sayed, Enhanced Photoassisted Water Electrolysis Using Vertically Oriented Anodically Fabricated Ti-Nb-Zr-OMixed Oxide Nanotube Arrays. *ACS Nano*, **2010**, *4*, 5819-5826.

138. Sulaeman, U.; S. Yin and T. Sato, Solvothermal synthesis of designed nonstoichiometric strontium titanate for efficient visible-light photocatalysis. *APPLIED PHYSICS LETTERS*, **2010**, *97*, 103102.

139. Liu, M.; N. d. L. Snapp and H. Park, Water photolysis with a cross-linked titanium dioxide nanowire anode  Tools and Resources. *Chem. Sci.*, **2010**, *2*, 80-87.

140. Longo, P., Atomic Level EELS Mapping Using High Energy Edges in DualEELS Mode. *Analytical TEM Application Note*.

141. Egerton, R. F., Electron energy-loss spectroscopy in the TEM. *Rep. Prog. Phys.*, **2009**, *72*, 25.

142. Ahn, C. C. and O. L. Krivanek, EELS Atlas, A.H.a.G. Inc., Editor.

143. Watanabe, M.; M. Kanno and E. Okunishi, Atomic-Resolution Elemental Mapping by EELS and XEDS in Aberration Corrected STEM. *JEOL News*, **2010**, *45*.